Dissertation

submitted to the
Combined Faculty of Natural Sciences and Mathematics
of the Ruperto Carola University Heidelberg, Germany
for the degree of
Doctor of Natural Sciences

Presented by

Theresa Schlamp, M.Sc.
born in Berlin, Germany

Oral examination: 30th October 2020

Investigating the impact of cell wall dynamics on secondary growth regulation

Referees:

Prof. Dr. Thomas Greb

Prof. Dr. Karin Schumacher

Acknowlegments

I want to thank the people who enabled me to work, discover and question. I can not express the the deep gratefullness that I feel when I think back.

First of all I want to thank Prof. Thomas Greb, who made it possible for me to enter into the field of developmental biology. Thank you so much for giving me the freedom and the guidance that I needed, thanks for supporting me without restricting me. The supportive and very open atmosphere in the Greb lab was extremly important for me. I want to say “thank you” especially to Virginie who was always willing to help and fascilitates the dive into a biological laboratory. She helped me to understand basic concepts and to develop my own strategies, I think without her it would have been a much harder time. Thanks to Vadir, who was my bench neighbor and always ready for a philosophical challenge and a broad view on thematic relationships. Thanks also to Dongbo, Sophie and Jiyan, who helped me with their huge knowledge and skills, and filled my toolbox. For the input and discussions about science and beyond, for social interaction and fun I like to thank Nina, Denis and Pascal. Thank you Ilona, for helping, for chatting and for taking care. Thanks to Dmitry for his time and knowledge that he shared with me so freely and his practical input in the Brillouin system.

Vielen Dank an meine Familie, an meine kleine und an meine große. Dafür ein Ausgleich zu sein und dafür, dass ihr immer hinter mir steht, auch wenn es schwieriger wird. Ihr habt mir die Balance gegeben, die während der Zeit der Doktorarbeit nötig war.

Zusammenfassung

Die Morphologie von Pflanzen kann sich aufgrund von post-embryonaler Entwicklung, sehr gut anpassen. In Pflanzen werden Stammzellpopulationen das ganze Leben über bewahrt und ermöglichen lebenslange Entwicklung. Längenwachstum, wird durch meristematische Aktivität an Spross- und Wurzelspitze ermöglicht, während das Dickenwachstum durch die Aktivität des seitlichen Meristems, auch vaskuläres Kambium genannt, ermöglicht wird. Dieses kann Gewebe nach zwei Seiten ausbilden. Anfänglich ist das vaskuläre Kambium ausschließlich in den vaskulären Bündeln aktiv. Zu einem späteren Punkt in der Entwicklung breitet sich das vaskuläre Kambium in die Region zwischen den vaskulären Bündeln – der sogenannten intervaskulären Region – aus und beginnt sich zu teilen, was eine post-embryonale Etablierung des vaskulären Kambiums bedeutet. Seine Bildung basiert potenziell auf der Dedifferenzierung von bereits differenzierten Zellen. Wie genau dieser Prozess beginnt und welche Mechanismen wichtig sind, ist jedoch nur schlecht verstanden.
Ich habe die Bildung von vaskulärem Kambium, als ein beeindruckendes Beispiel von Modellierung von Gewebespezifität, untersucht. Um die Bildung von vaskulärem Kambium genauer zu untersuchen, habe ich ein induzierbares System genutzt, welches mir ermöglicht hat, Auxinbiosyntheses zelltypspezifisch anzuregen. Bemerkenswerterweise hat die Anregung von Auxinbiosynthese in voll differenzierten Zellen der Stärkescheide ein Wechsel der Gewebespezifität und die Bildung des intervaskulären Kambiums ausgelöst. Während der detaillierten Analyse der Bildung des intervaskulären Kambiums wurde es deutlich, dass Auxin-induzierte Veränderungen der Expression bestimmter Gene von besonderer Wichtigkeit sind. Außerdem habe ich die Rolle der Zellwand während der Bildung von vaskulärem Kambium untersucht, da Pflanzenzellen durch Zellwände – eine steife extrazelluläre Matrix – immobilisiert werden. Die dadurch fixierte Position der Zelle, kann wichtige Information für deren Festlegung der Gewebespezifität beinhalten. Interessanterweise findet eine umfangreiche Zellwandmodellierung während der Bildung des vaskulären Kambiums statt, wie ich es anhand der Quantifizierung von verändertem Extensin Vorkommen und dem veränderten Zustand der Pektine nachweisen konnte. Eine genomweite Veränderung des Transkriptionsprofils während der von Auxin angeregten Bildung von vaskulärem Kambium unterstützt dieses Ergebnis, da unter den differentiell exprimierten Genen überproportional viele Gene, die mit Zellwandmodellierung in Zusammenhang gebracht werden können, waren.
Zum Schluss habe ich die Wichtigkeit von Zellwandmodellierung während der Bildung

von vaskulärem Kambium zeigen können, indem ich die Auxin induzierte Bildung von vaskulärem Kambium durch Verhinderung von Zellwandmodellierung blockiert habe.

Es kann angenommen werden, dass sich durch eine Veränderung in der Zusammensetzung der Zellwand auch deren Elastizität verändert, was eventuell für Dickenwachstum von Wichtigkeit sein könnte. Um die Veränderungen der Elastizität der Zellwand zu messen, habe ich eine Brillouin Mikroskop in unserem Labor etabliert und untersucht, wie Zellwandeigenschaften von der Orientierung und der Lokalisierung der Zellwand abhängen. Ich habe damit gezeigt, dass Brillouin Mikroskopie eine passende Methode ist, um die mechanischen Eigenschaften von Zellwänden zu untersuchen.

Abstract

The morphology of plants can be highly adaptive due to the plasticity governed by postembryonic development. In plants, stem cell populations, called meristems are maintained through the entire life and enable lifelong development. Longitudinal growth is realized by the meristematic activity in the apices of the shoot and root, while lateral growth is enabled by the activity of the vascular cambium that is able to produce specialized tissues in a bifacial manner. Initially, the fascicular cambium is active solely in vascular bundles. At a later stage of development, the fascicular cambium extends and cells in the region between vascular bundles – the so-called interfascicular region – start to divide, cumulating in the post-embryonic establishment of the vascular cambium. Its formation is potentially based on de-differentiation of differentiated cells. However, how exactly this process is initiated is still poorly understood.

Here, I used the process of vascular cambium formation, as a unique model to study cell fate change. To control the formation of vascular cambium, I used a genetic tool that allowed me to induce auxin biosynthesis in a cell type-specific manner. Strikingly, induction of auxin biosynthesis in fully differentiated starch sheath cells provoked a cell fate change and initiated the formation of interfascicular cambium. Based on detailed analysis of interfascicular cambium formation, nuclear auxin signaling is shown to be critical for this process. Furthermore, I investigated the role of cell wall during vascular cambium formation, as plant cells are immobilized by cell walls – a rigid type of extracellular matrix. The thereby fixed position of the cell can contain important information for cell fate determination. Interestingly, extensive cell wall remodeling takes place during cambium formation, as revealed by immunohistochemical quantification of extensin abundance and pectin modifications. Genome-wide transcriptional profiling upon auxin-induced interfascicular cambium formation further supports this result, as genes related to cell wall remodeling were disproportionately represented among differentially expressed genes. Finally, I demonstrated the importance of cell wall remodeling during interfascicular cambium formation by blocking auxin induced interfascicular cambium formation via inhibiting cell wall remodeling.

The reported change in cell wall composition during vascular cambium formation may cause a change in the elasticity of the cell wall, which might in turn be a prerequisite for lateral growth. To quantitatively measure the elasticity of cell walls, I established Brillouin microscopy in our lab and investigated cell wall properties depending on their orientation and localization. I was able to show that Brillouin microscopy is a suitable method to further investigate cell wall mechanics and its impact in the field of plant science.

List of abbreviations

Listed in alphabetical order are abbreviations for genes, organisms, and scientific terms recurring in this dissertation. Gene names are written in capitals and italics.

AFM	Atomic force microscopy
AHA2	*H(+)-ATPASE 2*
ANY1	*ANISOTROPY1*
APC	Angled physical contact
AR	Anti refective
ARF	Auxin response factor
ARF19	*AUXIN RESPONSE FACTOR 19*
ARF5	*AUXIN RESPONSE FACTOR 5*
ARF7	*AUXIN RESPONSE FACTOR 7*
BDL	*BODENLOS*
BSA	Bovine Serum Albumin
CESA	*CELLULOSE SYNTHASE*
CESA1	*CELLULOSE SYNTHASE1*
CESA2	*CELLULOSE SYNTHASE2*
CESA3	*CELLULOSE SYNTHASE3*
CESA5	*CELLULOSE SYNTHASE5*
CMF	Cellulose micro fibrils
Col	Columbia
DAG	Days after germination
DAT	Days after treatment
dCT	Delta cycle threshold
DPSS	Diode pumped solid state
DR23	Direct red 23
EDTA	Ethylenediaminetetraacetic acid
eGFP	Enhanced Green fluorescent protein
ER	Endoplasmic reticulum
EXP20	*EXPANSIN20*
EXT1	*EXTENSIN1*

FWHM	Full width at half maximum
GFP	Green fluorescent protein
GO	Gene ontology
GUS	β-glucuronidase
HG	Homo galacturonan
HyD	hybrid detectors
IAA12	*INDOLE-3-ACETIC ACID INDUCIBLE 12*
IC	Interfascicular cambium
KOR1	*KORRIGAN1*
LD	Long day
MP	*Monopteros (ARF5)*
mRFP	Monomeric Red Fluorescent Protein
mRNA	Messenger Ribonucleic acid
NA	Numeric appertur
ND	neutral-density
NPA	1-N-Naphthylphthalamic acid
PCR	Polymerase chain reaction
PIN3	*PIN-FORMED 3*
PME3	*PECTIN METHYLESTERASE 3*
PME61	*PECTIN METHYLESTERASE 61*
PMEI3	*PECTIN METHYLESTERASE INHIBITOR 3*
PMEI5	*PECTIN METHYLESTERASE INHIBITOR 5*
PMT	Photomultiplier tubes
PXY	*PHLOEM INTERCALATED WITH XYLEM*
RAM	Root apical meristem
RG I	Rhamnogalacturonan I
RG II	Rhamnogalacturonan II
RLP44	*RECEPTOR LIKE PROTEIN 44*
SAM	Shoot apical meristem
SAUR19	*SMALL AUXIN UP RNA 19*
SAUR44	*SMALL AUXIN UP RNA 44*
SCR	*SCARECROW*
SD	Short day
SMXL5	*SUPPRESSOR OF MAX2 1-LIKE5*
TIR1	TRANSPORT INHIBITOR RESPONSE 1

VIPA	Virtual image phase array
WOX4	*WUSCHEL RELATED HOMEOBOX 4*
WOX5	*WUSCHEL RELATED HOMEOBOX 5*
WUS	*WUSCHEL*
YFP	Yellow fluorescent protein

Table of content

1. Introduction

Plants live a sessile lifestyle; they cannot escape unideal environmental conditions or attacks by herbivores. The postembryonic mode of development enables plants to react to their environment and solve problems on site without the necessity to move. This lifelong development is made possible through a permanently active group of pluripotent stem cells and also explains the huge plasticity in growth and form of plants that is very reliant on environmental circumstances (Greb and Lohmann, 2016). The fate of the cells that are permanently produced by those stem cells is determined by positional cues depending on requirements derived by developmental stage and environmental input (Chan et al., 2017). Unlike in animals, the extracellular matrix of plants forms a rigid cell wall that fixes the position of cells relative to each other. The interplay between the cell innate turgor pressure and the variable cell wall lead to the inherent biomechanical forces found in plant cells and tissues. Those underlying forces play an important role in development and growth of plants (Hamant and Traas, 2010).

With respect to mechanical properties of participating cells, radial plant growth, during which the plant body expands laterally, is a remarkable process. Radial growth is based on the activity of a stem cell niche, called the cambium, which is deeply embedded into specialized tissues (Sehr et al., 2010). Although being essential in ecological and economic terms, a detailed understanding of plant cell wall remodeling in the cambium zone and its impact in cambial activity remains unknown.

1.1. Secondary growth

Arabidopsis thaliana is a model plant, that enable to us cell fate regulation in very good spatio-temporal resolution. The fixed position of each cell makes it possible to follow cell linages easily, determine changes of cell identity within those and investigate underlying regulatory mechanisms.

Plant growth can be divided into two different phases. During primary growth plants grow vertically and develop primary tissues, like the epidermis or vasculature. Primary growth is driven by the activity of apical meristems. Those primary meristems harbour pluripotent stem cells and are located at the shoot tip and the root tip and are called shoot apical meristem (SAM) and root apical meristem (RAM), respectively (Basile et al., 2017). The SAM

is responsible for the formation of all organs above the ground whereas the RAM is responsible for the formation of all organs below the ground. In contrast to primary growth, where organs are formed along a vertical growth axis, secondary growth is responsible for lateral expansion of this axis (Tonn and Greb, 2017). Secondary growth is governed by pluripotent cells that reside in the bifacial stem cell niche named vascular cambium, that produce xylem towards the inside and phloem towards the outside (Barra-Jiménez and Ragni, 2017; Nieminen et al., 2015). During the phase of primary growth, the vascular cambium is restricted to the vascular bundles (Figure 1 B). Only later during the phase of secondary growth, a closed cylinder of stem cells is established giving rise to differentiated tissues by periclinal cell divisions at the base of the stem to provide stability (Agusti and Greb, 2013; Altamura et al., 2001) (Figure 1 C). The establishment of the interfascicular cambium, established de novo between vascular bundles, is a developmental process that progressively takes place from the lower to the upper stem (Sehr et al., 2010; Suer et al., 2011). The exact mechanism underlying the formation of interfascicular cambium is still not completely understood. However, in previous work it has been shown that parenchymal cells could serve as an origin for interfascicular cambial cells (Altamura et al., 2001; Mazur and Kurczynska, 2012) and another study supported starch sheath cells as progenitors for *de novo* formed interfascicular cambium (Sanchez, 2013). The starch sheath is the innermost cortical cylindrical cell layer and cells contain the amyloplasts. Some important factors of the molecular regulation of cambium are known, like transcription factors from the WUSCHEL-RELATED HOMEOBOX (WOX) family and a receptor kinase *PHLOEM INTERCALATED WITH XYLEM* (Brackmann et al., 2018; Suer et al., 2011). Two genes that are expressed in the cambium domain and are important for its regulation are *WOX4* and *PXY* which are common cambium markers. It is known, that the homeobox transcription factor WOX4 is important to maintain stem cell activity and that it is important for vascular cell division and acts downstream of PXY. PXY itself regulates vascular cell division, vascular organization and xylem differentiation and is needed for auxin-dependent stimulation of cambial activity via WOX4 mRNA level (Etchells et al., 2013; Fisher and Turner, 2007; Suer et al., 2011). Auxin had been shown to trigger interfascicular cambium initiation and is important to control cambium activity (Agusti et al., 2011a; Brackmann et al., 2018; Suer et al., 2011). Other hormones like cytokinin, strigolactone and

brassinosteroids were found to be important for secondary growth too (Agusti et al., 2011a; Caño-Delgado et al., 2004; Han et al., 2018; Nemhauser et al., 2006). The mechanism of interfascicular cambium initiation, the importance of auxin signaling and cell wall remodeling are still not completely understood and are part of this study.

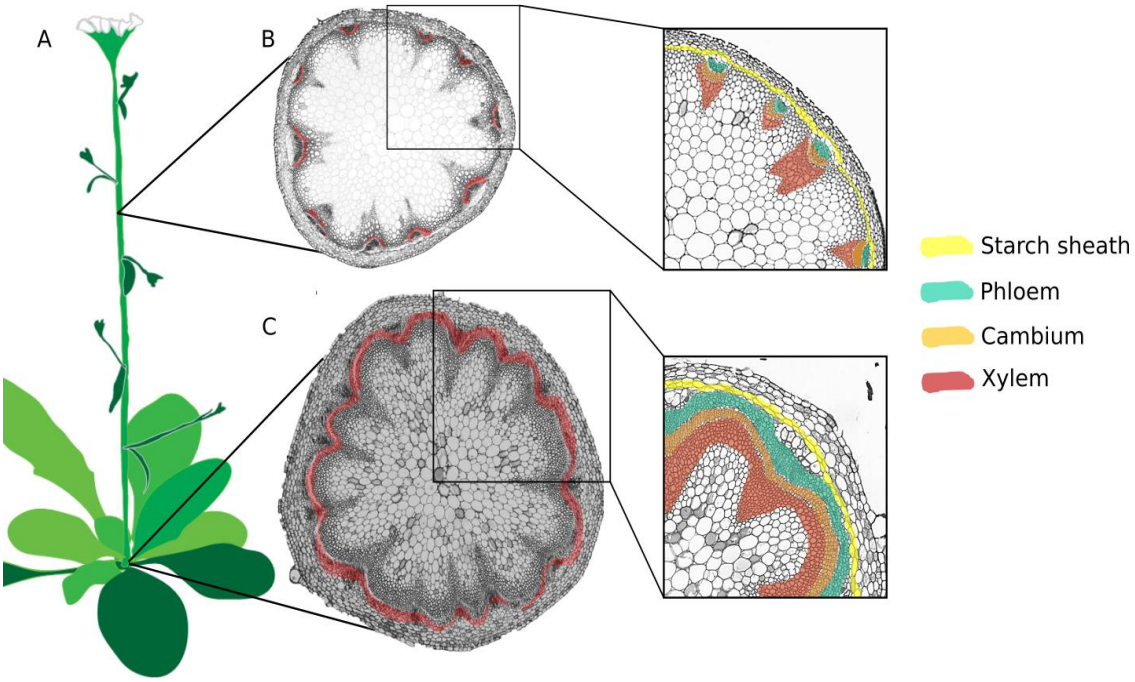

Figure 1 ***The interfascicular cambium is a stem cell niche that is established de-novo.*** *Arabidosis thaliana (A, drawing adapted from Pablo Sanchez thesis) with primary growth conformation in the upper stem (B) and secondary growth conformation at the base (C), image details at the left side with starch sheath, phloem, cambium and xylem tissue color-coded as indicated in the ledgend.*

1.2. The plant hormone auxin and its signaling

The *de novo* formation of the interfascicular cambium is known to be tightly regulated by plant hormones, especially auxin (Agusti et al., 2011a, 2011b; Sehr et al., 2010; Suer et al., 2011; Uggla et al., 1996) which mainly originates from the shoot apical meristem and from young leaves and is transported towards sink tissues at the base of the stem (Friml, 2003; Ljung et al., 2001; Muday, 2001). Auxin is a small, multifunctional molecule that is involved in numerous aspects of plant development like organogenesis (Heisler et al., 2010; Sassi et al., 2014; De Smet et al., 2010), gravitropism (Marchant et al., 1999; Rashotte et al., 2000) and growth through cell wall expansion (Esmon et al., 2006; Rayle and Cleland, 1992). Interestingly, it

can have different effects in different parts of the plant. In the SAM, low levels of auxin signaling need to be maintained to inhibit differentiation of the pluripotent stem cells in the WUSCHEL (WUS) domain. Thereby, WUS represses auxin signaling output in the meristem center where differentiation needs to be repressed (Ma et al., 2019) while at the periphery, where organ formation takes place, auxin signaling is increased. This contrasts with auxin function in the root where an auxin maximum is maintained in the quiescent centre in order to prevent differentiation and gradually decreases in the more differentiated parts of the root (Petersson et al., 2009). How auxin affects the balance between differentiation and stemness in the cambium is still not understood. From studies in aspen and pine trees its known, that there is an auxin maximum in the cambium region (Kramer et al., 2008; Uggla et al., 1998). Also studies from *Arabidopsis thaliana* show a maximum of auxin signaling in the cambium (Smetana et al., 2019; Suer et al., 2011), suggesting a situation comparable to the root, where high levels of auxin are needed to maintain stem cells. At the same time, an auxin gradient is necessary to realize the transition between cambium stem cells and developing vasculature, similar to the situation in the SAM (Smetana et al., 2019). Even though the impact of auxin signaling in stem cell regulation is similar to certain aspects in one or the other stem cell niche it does not completely mirror one situation exactly. Analogous to the situation in the SAM and RAM the transcription factor WOX4, which maintains stem cell fate like WUS and WOX5 in the SAM (Mayer et al., 1998) and the RAM (Stahl et al., 2009), respectively, responds to alterations in auxin levels (Suer et al., 2011). Main parts of the transcriptional regulation that is caused by auxin is realized via a short intracellular signal transduction pathway that is shown in Figure 2. Auxin mediates binding between the Aux/IAA transcriptional repressor family and F-box proteins of the TRANSPORT INHIBITOR RESPONSE1/AUXIN SIGNALING F-BOX (TIR1/AFB) family (Tan et al., 2007). The TIR1/AFB proteins are part of to a SCF-type ubiquitin protein ligase complex, which is responsible for the ubiquitination of Aux/IAA proteins which makes their degradation possible (Gray et al., 2001; Zhou and Howley, 1998). If they are not hindered by Aux/IAA proteins, members of the AUXIN RESPONSE FACTOR (ARF) family can bind to specific regions at so called AUXIN RESPONSIVE ELEMENTS (ARE) in the promotor region of certain auxin inducible genes and activate their transcription (Lavy et al., 2016; Wang et al., 2013).

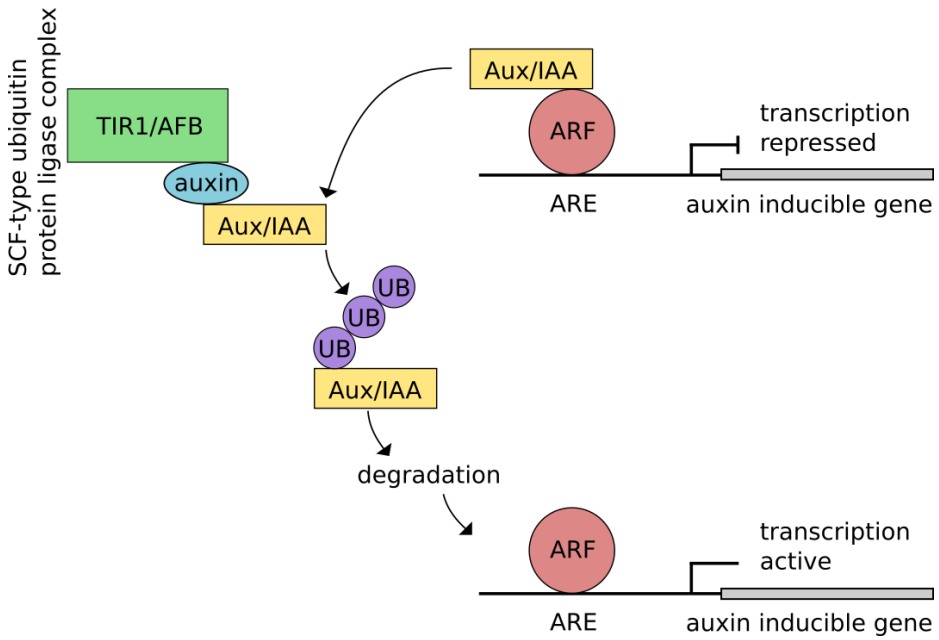

Figure 2 ***Main auxin signaling pathway of auxin dependent transcription****, members of the Aux/IAA transcriptional repressor family dimerize with transcription factors of the AUXIN RESPONSE FACTOR (ARF) family and prevent the activation of AUXIN RESPONSIVE ELEMENTS (ARE) in promoter regions of auxin inducible genes and therefor transcription of auxin inducible genes is repressed. Auxin connect F-box proteins of the TRANSPORT INHIBITOR RESPONSE1/AUXIN SIGNALING F-BOX (TIR1/AFB) family and members of the Aux/IAA transcriptional repressor family brings them to the SCF-type ubiquitin protein ligase complex. Subsequently Aux/IAAs go through ubiquitination and degradation and ARFs can bind to AREs to allow transcription of auxin inducible genes. Illustration adapted from (Leyser, 2018).*

1.3. The plant cell wall – a rigid and flexible network with impact

The plant cell wall is a heterogeneous and dynamic structure and represents an extracellular matrix outside of the plasma membrane. Plant cell walls are very ambivalent in their provided properties, on the one hand providing a rigid structure that supports and protects the plant against biological, chemical or biophysical impact and define the growth vector for cells by restricting turgor driven growth to the desired directions only. On the other hand, it has to be flexible to allow turgor-driven cell growth which can only take place if the cell wall is flexible enough to allow extension (Burton et al., 2010; Proseus and Boyer, 2005; Wolf et al., 2012a). There are two kinds of cell walls. The first is the primary cell wall which consists mainly of glucan-based CMFs in a matrix of pectins, hemicellulose, structural proteins and proteoglycans, and which is highly hydrated (Burton et al., 2010; Carpita and Gibeaut, 1993; Cosgrove, 2005; Wolf et al., 2012a). The primary cell wall can be found in young and growing cells and only when cells stop growing and become more specialized, a secondary cell wall is established.

This secondary cell wall is mainly composed of cellulose, hemicellulose and lignin and found in vessels or fiber tissues (Takenaka et al., 2018a). As the cell wall is such a heterogeneous structure, its main components that were important during the present study, will be introduced individually here.

1.3.1. Cell wall components

Cellulose

Cellulose is composed of (1,4)-β-D-glucan chains, that are organized in parallel arrays and are tightly connected to each other by hydrogen bonds in cylindrical fibers (cellulose microfibrils – CMF). Those CMFs give the plant strength to resist tensile forces and bear additional load. They also conduct the direction of cell expansion, which is in most cases (with the exception of the epidermis) perpendicular to the net orientation of CMF (Baskin, 2005; Marga et al., 2005) and cause directional or anisotropic growth. Cellulose is synthesized in the cellulose synthase (CESA) complex composed of at least three types of glycosyl transferases arranged into a hexameric rosette. The complex contains also other components such as KORRIGAN1 (KOR1), which is part of the cellulose synthesis complex but its full function is not completely understood (Mutwil et al., 2008; Somerville, 2006; Vain et al., 2014). The cellulose synthase complex is guided by cortical microtubules located intracellularly close to the plasmamembrane and microtubules and CMFs can be found to be co-aligned often (Gutierrez et al., 2009; Paredez et al., 2006). In consequence, mutants that are affected in cellulose synthesis and/or orientation show a disturbed orientation of expansion (Chen et al., 2010; Fujita et al., 2013).

Hemicellulose

The most abundant hemicellulose in *Arabidopsis thaliana* is Xyloglucan, which consist of (1,4)-β-D-glucan chains with sidechains of galactose, fucose and/or xylose residues. The postulated role of Xyloglucan is to be a crosslinker or spacer of CMF and thereby influences stability of the microtubule cytoskeleton (Eckardt, 2008; Scheller and Ulvskov, 2010; Xiao et al., 2016). Opposite of xyloglucans that can be found in primary cell walls, other hemicelluloses like xylans, heteroxylans and (1,3;1,4)-

β-D-glucans can be found in secondary cell walls (Carpita and Gibeaut, 1993).

Pectin

Pectin is an important cell wall polysaccharide that impacts cell wall porosity and hydration. It consists of four main components: homogalacturonan (HG), rhamnogalacturonan I (RG I), rhamnogalacturonan II (RG II) and xylogalcturonan (XG) (Willats et al., 2001; Wolf et al., 2009). HG is the main polysaccharide in primary cell walls and is highly methyl-esterified when built in. Those methyl groups can be cleaved by PECTIN METHYL ESTERASEs (PMEs) which can dramatically change physical properties like cell wall elasticity. Negatively charged pectate can bind calcium ions in so called „egg-box" structures which strengthens the cell wall. Pectate can also be degraded by polygalacturonases or pectin/pectate lyases which would soften the cell wall (Vincken et al., 2003; Wolf et al., 2009). Overexpression of PMEs or their inhibitors, the PECTIN METHYL ESTERASE INHIBITORs (PMEIs), lead to drastic change in cell wall elasticity and respective plants are impaired in their growth and/or organogenesis (Paynel et al., 2014; Peaucelle et al., 2008, 2011).

RG I is a very complex polysaccharide, that consists of alternating galacturonic acid and rhamnose with galactose, arabinose or arabinogalactan sidechains which regulate elasticity and extensibility of the cell wall (Takenaka et al., 2018b). RG II can be found in the primary cell wall and consists out of 12 different glycosyl residues which are linked by more than 20 different glycosylic linkages and is thereby very complex. Its ability to form dimers via covalently cross linking via borat diesters is required for the three dimensional structure of the pectic network (O'Neill et al., 2004). Xylogalcturonan is a HG subunit that is substituted with an additional xylose (chain) and can be found in reproductive tissues mostly but also stem and leaves (Zandleven et al., 2007).

Expansin

Expansins are proteins that were found to be important for the mechanical properties of the cell wall and for growth and morphogenesis

of the whole plant body. In studies from the last decades it was suggested, that expansins play an important role in softening of the cell wall through disruption of hydrogen bonds between CMF and hemicellulose (preferentially xyloglucan) (Li et al., 2003; McQueen-Mason et al., 1992). Their non-enzyme activity is highly pH-dependent and could, thus, provide a link between the auxin induced cell wall acidification (see below) and the cell wall extension that is needed prior to turgor driven cell growth (Cosgrove, 2005; Esmon et al., 2006; Majda and Robert, 2018).

Extensin

Extensins are structural glycoproteins that provide a scaffold for the growing primary cell wall (Cannon et al., 2008; Lamport et al., 2011). They have the ability to self-assemble due to their amphiphilic character. Furthermore they can insolubilize via extensin crosslinking, catalyzed by specific extensin peroxidases (Jacobowitz et al., 2019; Schnabelrauch et al., 1996), or via acid base interaction in extensin – pectate (Cannon et al., 2008; Smith et al., 1984). Extensin mutants are impaired in growth and morphogenesis (Baumberger et al., 2001; Draeger et al., 2015).

1.3.2. Auxin and its impact on cell wall

Auxin is known to induce transcriptional changes in the expression of many genes such as members of *SAUR*s (*Small Auxin up RNA*s) or Aux/IAAs (Quint and Gray, 2006) families. In addition, it can also affect the transcription of cell wall-related genes during processes like growth, morphogenesis and organ formation (Aryal et al., 2020; Braybrook and Peaucelle, 2013; Sassi et al., 2014). Cell wall expansion can be stimulated by auxin through modulation of expression of cell wall-related genes (Braybrook and Peaucelle, 2013; Nemhauser et al., 2006; Reinhardt et al., 1998). Furthermore, auxin can cause acidification of the apoplast (Haruta et al., 2015; Takahashi et al., 2012). The most supported pathway by which auxin induces cell wall acidification is probably through induction of *SAUR19*, which causes inactivation of a PP2C-family phosphatase. In consequence the auto-inhibitory domain of the H^+-ATPase is phosphorylated and the proton pump is activated

(Fendrych et al., 2016; Spartz et al., 2014). This acidification of the apoplast influences the activity of cell wall remodeling proteins like expansins (which have a pH optimum < 5.5 (Cosgrove, 2000; Wang et al., 2008), pectin methylesterases (*PME*s) (Denès et al., 2000) and others. Simultaneously the resulting proton gradient causes hyperpolarization of the plasmamembrane which is followed by opening of the voltage sensitive K^+ channels and an increasing turgor pressure through osmosis (Fendrych et al., 2016). The weakened cell wall and the increase in turgor pressure let the cell expand.

1.3.3. Mechanical properties of cell wall

Plant cells are surrounded by an extracellular matrix, the cell wall, which dominates the mechanical behavior of the whole cell. The various components of the cell wall can influence cell wall mechanics on very different ways. Pectin as one of the most abundant cell wall component is highly methylated when secreted into the cell wall, which is generally associated with a rather soft cell wall. Once the cell wall ages, pectin gets de-methyl esterified which influences mechanical properties in both directions, cell walls can get stiffer (because of the formation of Ca^{2+} dependent “egg-box” structures) or softer, like in the SAM (Braybrook and Peaucelle, 2013; Peaucelle et al., 2011). But also the ratio of side chains of the RG I (arabinan and galactan) can affect mechanical properties of the cell wall (McCartney et al., 2000). The mechanical anisotropy of cell walls is mainly realized by the orientation of the load-bearing CMFs, if the orientation of those is changed it can have a drastic effect on mechanical properties (Baskin, 2005; Marga et al., 2005). CMFs are in most cases oriented perpendicular to the growth direction. This provides stability on horizontal direction and enable cell wall extensibility along the longitudinal axis at the same time (Adamowski et al., 2019; Anderson et al., 2010). Furthermore, there are cell wall remodeling proteins like expansins and pectin methylesterases which impact the interaction of cell wall epitopes and thereby also alter the mechanical properties of cell wall.

1.4. Mechanics in biology

In 1917 biological patterns have been already described as "diagrams of underlying forces" by D'Arcy Thomson in his book "On Growth and Form" (Thomson, 1917). After firstly focusing on molecular cues of development, the contribution of mechanics to developmental processes got again in the center of attention. From mammalian cells cultured on hydrogels with different mechanical properties it is known that the Young's modulus of the provided matrix affects cell spreading, morphology and function (Pek et al., 2010; Žigon-Branc et al., 2019). For mammalian stem cells plated on hydrogels it has been shown, that their cell fate strongly depends on mechanical properties of the hydrogel (Engler et al., 2006; Pek et al., 2010). Also, for the development of whole organisms, mechanical impact is more and more taken into account as an important factor. To just pick two examples: realization of the layer organization in zebra fish through intercellular surface tension (interaction of adhesion force and intracellular tension). Secondly, the dorsal closure during embryogenesis of drosophila as a result of interaction between tension in two different tissues (Kiehart et al., 2000; Schötz et al., 2008)(amnioserosa and lateral epidermis) (Kiehart et al., 2000; Schötz et al., 2008).

1.4.1. Elasticity modulus

The elasticity modulus describes the resistance of an object being deformed elastically (non-permanently) when stress is applied on it. In other words, it is the ratio of stress and strain, stress as an applied force and strain as the parameter for the degree of deformation. The higher the force that is needed to gain a certain deformation the higher is the elasticity modulus. As most biological samples are neither structurally homogeneous nor isotropic, the directionality of applied force and resulting deformation is important in most cases. Hence, it has to be differentiated between the bulk modulus, the shear modulus, the Young's modulus and the longitudinal modulus (Figure 3). The bulk modulus (Figure3, A) is the volume change due to a change in pressure. The shear modulus (Figure 3, B) quantifies the deformation of an object as a consequence of force that being applied parallel to the surface of the object. The Young's modulus (Figure 3, C) quantifies the reaction of an object to uniaxial applied stress by parallel and perpendicular

deformation to the applied force. In contrast, the longitudinal modulus (Figure 3, D) measures the ratio between unidirectional stress and strain along the very same direction (87). However, the object's perpendicular deformation (with respect to the applied force) is restricted.

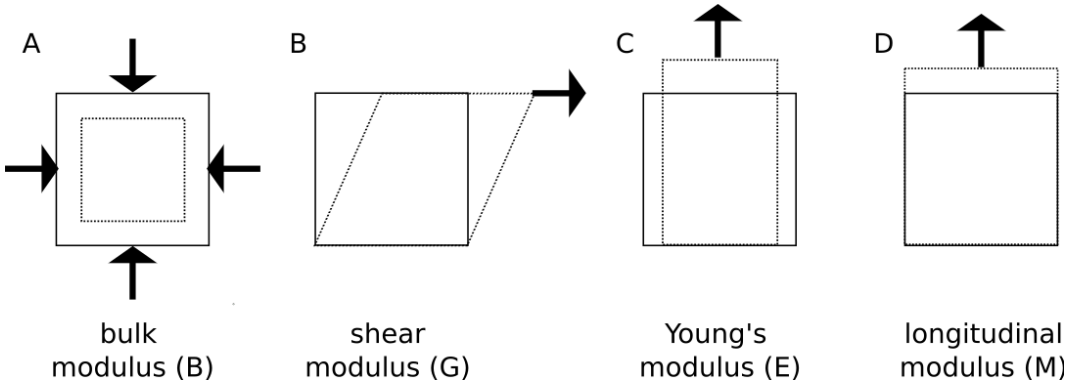

Figure 3 ***Schematic representation of the relationship between applied force, stress and deformation, strain****. Bulk modulus (A), shear modulus (B), Young's modulus (C) and longitudinal modulus (D) (Illustration adapted from M.Nicolic et al. (2018)).*

1.4.2. Determining mechanical properties of biological samples

To study mechanical properties of cells and/or extracellular matrixes a couple of methods are available such as atomic force microscopy (AFM), micropipette aspiration, traction force microscopy, etc. AFM uses a cantilever, which applies a precise force on a sample and measures its deformation. The ratio between the applied force (stress) and the deformation is used to calculate the Young's modulus at a spatial resolution in the nm range and a length scale range between 0.1 nm – 100 µm. Due to instrumental restrictions the temporal resolution is quite poor and tissues can only be probed at the surface (Müller and Dufrêne, 2011). Micropipette aspiration uses predefined negative pressure (aspiration) on the sample and take its resistance to deform to calculate its elastic properties at single cell resolution (Daza et al., 2019; Lee and Liu, 2014). With this method only one single cell can be analyzed at a time, so that the throughput is low. Mostly cells are immobilized and this can impact the mechanical response (Daza et al., 2019; Lee and Liu, 2014). A contact-free method to determine the elastic modulus in biological samples is micro-rheology. For this method, fluorescent traceable probes are injected in the biological sample and their motion is tracked. Assuming Brownian motion of the fluorescent dyes, this strategy allows the determination of the local elasticity modulus (Weihs et

al., 2006). Brillouin microscopy is a non-tactile (not restricted to the surface like AFM), label-free (samples does not need to be labeled like micro-rheology) method that can determine the elastic modulus of biological samples, either single cells (like micro-pipette aspiration that is restricted to single cells), tissues or whole organisms (Antonacci et al., 2020).

1.5. Brillouin Microscopy

Brillouin microscopy is a microscopic technique that enables scientists to create maps of elastic modulus of biological tissues at subcellular and reasonable temporal resolution. The underlying physical phenomenon of this imaging technique is Brillouin scattering and changes in instrumentation over the last two decades made it applicable to the field of life sciences (Antonacci et al., 2020).

1.5.1. Brillouin scattering

When light hits matter three processes can occur: light can be reflected, absorbed or scattered. Scattering of light can be ether elastic (Rayleigh, Mie) without the loss or gain of energy or inelastic (Brillouin, Raman) where the frequency and the direction of the beam is altered. The underling mechanism of Brillouin scattering was predicted by Leon Brillouin (1922) and Leonid Mandelstam (1926) and describes the inelastic scattering of light from thermally generated density waves. This interaction causes a loss and gain of energy (Stokes and Ani-Stokes shift) equal to the energy of the thermally generated density waves. Analyzing the spectral shift of the scattered light allows therefore conclusions on thermal density fluctuations of the material and related physical properties (Antonacci et al., 2020). When the scattering process occurs, we can define the wavevector k_i of the incident light with a frequency ω. After inelastic interaction with the material the scattered light propagates along the wavevector (k_s) with a frequency (ω + Ω), the sum of the frequency of the incident light and the thermal density wave Ω, respectively (Figure 4).

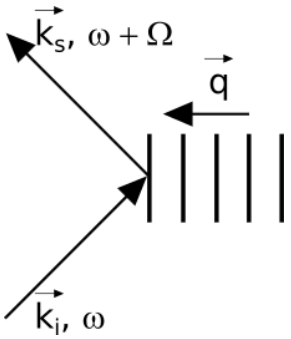

Figure 4 ***Scheme of the scattering process on thermal density waves****, incident light with a certain frequency (ω) follows the wavevector k_i and scattered at thermal density waves with the wavevector (q). After scattered from the material the scattered light follows the wavevector k_s with the frequency ω + Ω.*

The thermal density waves travel inside of materials with the speed of sound (ν), which is dependent on material properties like the longitudinal elastic modulus (M) and the density (ρ).

$$v = \sqrt{\frac{M}{\rho}} \qquad \textit{Equation 1}$$

Moreover, the frequency of the thermal density wave (Ω) is related to the wavevector ($\vec{q}$) by linear dispersion ratio.

$$\Omega = \sqrt{\frac{M}{\rho}} \cdot q \qquad \textit{Equation 2}$$

The intensity of the wavevector ($\vec{q}$) can be written as

$$q = \frac{4 \cdot \pi \cdot \eta}{\lambda} \cdot \sin\frac{\theta}{2} \qquad \textit{Equation 3}$$

and depends on the refractive index of the material (η) and the wavelength of the incident light (λ) and the scattering angle (θ). This is only true, because the shift of frequency is very small and the length of the wavevector of the scattered and the incident light are nearly the same. And so the frequency of the thermal density wave (Ω) can be written as

$$\Omega = \sqrt{\frac{M}{\rho}} \cdot \frac{4 \cdot \pi \cdot \eta}{\lambda} \cdot \sin\frac{\theta}{2} \qquad \textit{Equation 4}$$

From investigations about the refractive index and the mass density in biological tissues it is known that the relation of $\frac{\rho}{\eta^2}$ varies at most a few percent (Scarcelli et al., 2015) and can be assumed as constant. If the set-up to measure Brillouin shifts only evaluates light that is scattered back in an angle of 180° and the wavelength of the incident light stays constant it can be estimated that the frequency of the thermal density wave (Ω), which is equal of the frequency shift of the scattered light, is proportional to the longitudinal elastic modulus.

$$\Omega \propto \sqrt{M} \qquad \textit{Equation 5}$$

A typical Brillouin spectrum would look as follow (Figure 5).

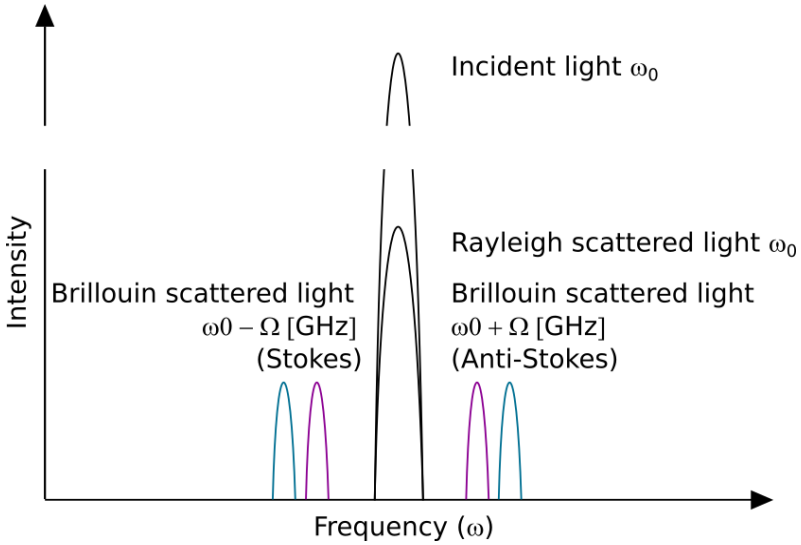

Figure 5 ***Schematic representation of a Brillouin spectrum together with the incident light and the elastic scattered light****, two Brillouin peaks can be observed, one shifted to a higher frequency (Anti-Stokes shift) and one shifted to a lower frequency (Stokes shift). As* $\boldsymbol{\Omega \propto \sqrt{M}}$*, "stiffer" material gives bigger shifts (turquoise) than "softer" material (purple).*

1.5.2. Brillouin spectrometer instrumentation

The Brillouin shift of biological materials is very small and a typical shift of around 8 GHz (λ = 532 nm) corresponds with a shift of the wavelength of 0.008 nm. Small shifts like this cannot be resolved with gratings or filters used in commercial fluorescence or Raman spectrometers. To obtain high spectral resolution sufficient to resolve small shifts like they are typical in Brillouin spectroscopy, Fabry-Perot-interferometer are used. Two highly reflective surfaces are placed parallel to each other and light gets partially transmitted and reflected at both surfaces (Figure 6, A). The phase delay of the beam created by a double reflection in the interferometer, creates a

transmission pattern which can be described by the Airy function. Unfortunately, the throughput efficiency is so bad (< 1%) that the acquisition time of one spectrum can range from minutes to hours (Ko and Kojima, 2009). This was the reason, why Brillouin spectroscopy was for a long time limited to application in material science. This was until 2008 when a spectrometer with a special kind of Fabry-perot etalon was introduced by G. Scarcelli and S.H.Yun, the virtual image phase array (VIPA) (Scarcelli and Yun, 2007). It consists of a glass cube with one surface that is highly reflective and one surface that is totally reflective and of an anti-reflective (AR)-coated entrance window (Figure 6, B). It allows fast acquisition of the spectrum because of a better throughput efficiency, that is sufficient to use Brillouin spectroscopy on biological samples (acquisition time around 0.1s/ spectrum) (Scarcelli and Yun, 2011).

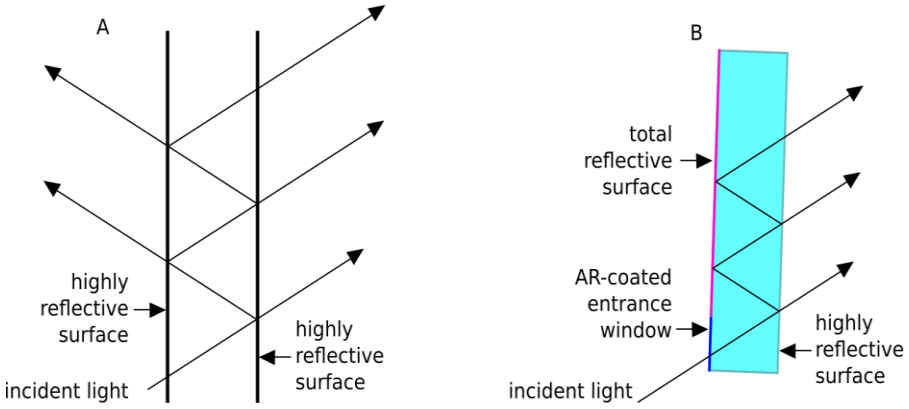

Figure 6 ***Schema of the internal reflection and transmission in a classical Fabry-Perot Interferometer*** *with two highly reflective surfaces (A) and a Virtual Image Phase Array with one total reflective surface (red) and an AR-coated entrance window (blue) (B).*

As most biological samples are turbid, light is scattered in an elastic fashion predominantly and thus is much stronger than inelastic scattering. Therefore, the signal from elastic scattering would overwhelm the weak Brillouin signal. To resolve the Brillouin signal, a high extinction coefficient (ratio of the minimal and maximal intensity of the transmitted light) of the spectrometer is required which can be realized by a cross-axis configuration of two VIPAs (Scarcelli and Yun, 2011). In a single VIPA configuration the Brillouin spectrum is dispersed along one axis along with the elastically scattered light (Figure 7A). In a two stage VIPA configuration the second VIPA is oriented 90° with respect to the first one. Here, the second dispersion axis is perpendicular to the first one and the resulting dispersion takes place along a diagonal line which separates the Brillouin signal from

the dispersion cross talk and the Rayleigh signal even further (Figure 7B). The remaining signal of elastically scattered light can be physically cut out by masks placed after each VIPA (Scarcelli and Yun, 2011).

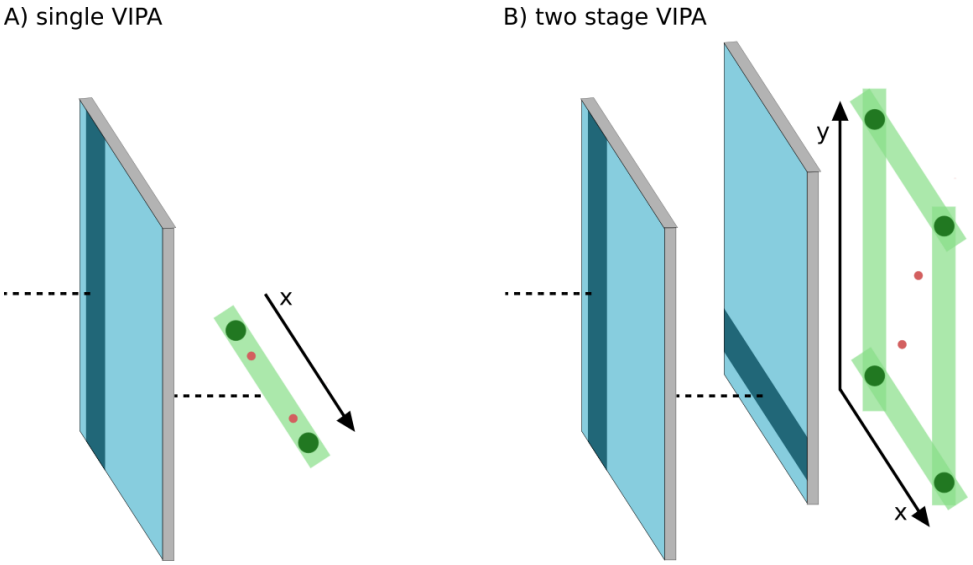

Figure 7 ***Dispersion pattern*** *in a single stage VIPA (A) with the dispersion axis (x), the Rayleigh signal (dark green), the Brillouin signal (red) and the dispersed cross talk signal (light green) and the dispersion pattern in a two stage VIPA (B) with two dispersion axis (x, y), the Rayleigh signal (dark green), the Brillouin signal (red) and the dispersed cross talk signal (light green)(adapted from (Scarcelli and Yun, 2011).*

Additional improvement of the spectral contrast, can be achieved by an extra VIPA. However, this would also reduce the throughput efficiency und with that the Brillouin signal intensity, which would eventually will lead to longer acquisition times. Alternatively, the usage of molecular absorption filters that can absorb the Rayleigh signal if the wavelength of the scattered light matches the atomic energy transition for $\lambda = 532$ nm (e.g. iodine absorption cell) could increase the spectral contrast further (Meng et al., 2014). Another method that can be used to block elastically scattered light is the introduction of a Lyot-stop, which is a 4-f element with a spatial filter (Edrei et al., 2017a). The underlying principle is that lenses function as Fourier-elements that transform frequencies in the k-space to the real space. Diffracted light which is high frequency light can be filtered out by physical blocking. In contrast, low frequency components (Brillouin signal) are passing through the filter and can be captured by the detector.

1.5.3. Brillouin Microscope

Microscopy is a very important technique in the field of life sciences and makes it possible to picture objects with an immense magnification with the help of a microscope. Various types of microscopes have been developed with very different underlying principles to visualize objects, depending on the requirements (high contrast, high resolution, imaging depth), for example light microscopy, electron microscopy and scanning probe microscopy. Light microscopy uses visible light that is either transmitted or reflected by the sample or interacted in a way with the sample (fluorescence, absorption, scattering). Light coming from the sample passes multiple lenses to allow a magnified view of the sample. Using a confocal light microscope has the advantage to gain higher resolution with a big penetration depth than a conventional bright field microscope, where the entire sample is illuminated. The principle of confocality is blocking off light that does not come from the focal plan of the tube lens of the objective. The blocking is realized by placing a pinhole at the focal point of the objective in front of the camera or the spectrometer, so that only light from the focal plane of the objective will pass through. The pinhole makes it necessary to acquire the image based on a probe scanning procedure. This can be realized by directing the light over the sample or by moving the sample with a scanning stage.

A Brillouin confocal microscope consists basically of three parts, the illumination part, the microscope body and the Brillouin spectrometer with the camera (Figure 27/ 26)

Illumination part

The light hitting the sample need to be very well defined. The beam should have a Gaussian shape like emitted by a single longitudinal mode laser, or after cleaning by guidance through a single mode fiber. Because the beam needs to slightly overfill the back-aperture of the objective, the beam usually needs to be expanded after cleaning.

Microscope

The incident light travels through an objective which can have a major impact on image quality. The most important feature of the used objective that should be considered, is the numerical aperture (NA). In Brillouin microscopy it has been found that a higher NA leads to an increased signal intensity but also to a loss of spectral resolution due to spectral broadening. The spectral broadening is caused by the wider range of scattering angle in which photons are collected. The low NA objectives have the advantage that they only collect photons of a small range of scattering angle, so that spectral broadening is avoided. In turn, because of the small amount of photons that are collected the signal intensity is lower. In most of the Brillouin microscopes light from the sample is collected within the 180° of backscattering because the Brillouin shift is maximized in this configuration and the effect of the NA of the objective is not as big as in other configurations using smaller collection angles (Antonacci et al., 2013). The signal is then conducted to the spectrometer freely or via a fiber. The usage of a single mode fiber has two advantages, the set-up is more robust against misalignments and the single mode fiber serves as a pinhole ensuring confocality.

Spectrometer part

The spectrometer can consist out of various parts which are partially described in 1.5.2. Important are the components that are necessary for the resolution of the Brillouin shift that is only around 0.01 nm. The resolution of small wavelength shifts like this can be realized by Fabry-Perot interferometer or VIPAs (Figure 6). The spectral contrast enhancement is especially important in biological samples and can be realized using an absorption cell or a Lyot-stop filter, explained in 1.5.2.

1.6. Aims and objectives

Thickening of plant shoots and roots is designated as secondary growth. During secondary growth it is important that meristematic activity is established in a cylindrical domain at the periphery of shoots and roots, such that tissues can be produced in a bidirectional manner. Cells with meristematic activity between vascular bundles in the shoot are called interfascicular cambium (IC). How these cambium cells are formed and what pathways are involved in this process was unclear. Results from a clonal analysis combined with 1-N-Naphthylphthalamic acid (NPA) treatments and the following auxin agglomeration suggest that starch sheath cells can de-differentiate and give rise to the IC [23]. Furthermore, the impact of the plant hormone auxin – an essential stimulator of cambium activity – was studied with high spatio-temporal resolution using an *in vitro* culture system [31]. RNA sequencing of certain tissues in the sample revealed genes having a key role in the regulation of the cell wall elasticity. Those genes were identified to change their activity early during induced IC formation.

Our knowledge about the impact of cell wall composition and properties during developmental processes like the IC formation is still very limited. My aim was to use the IC formation (de-differentiation of starch sheath cells) as a model to study the change in the cell wall during this process and the influence IC formation by cell wall modification. Another aim was to set up a Brillouin microscope to be able to quantify the elasticity modulus of cell walls during IC formation and other contexts. Having the hypothesis that cell wall remodeling is important during IC formation and can influence this developmental process, I formulated three objectives:

How is the biochemical and mechanical state of the cell wall modified during interfascicular cambium formation?

To investigate the dynamic modifications of cell wall properties during the IC formation I performed immunohistochemistry. I was able to visualize and quantity the dynamics of changes in cell wall composition with antibodies that are specific for extensins and certain methylation state of pectin. I used Brillouin microscopy to study cell wall mechanics in different organs (roots and shoot apical meristem) to establish the technique.

Can cell fate alteration be triggered or blocked by modification of the cell wall composition?

To elucidate the impact of the cell wall composition, I generated ethanol inducible lines to affect the methylation of the pectin, pectin methylesterase (PME3) and pectin methylesterase inhibitor (PMEI3, PMEI5) and express them under the starch sheath specific promoter pSCR, alone and simultaneously with iaaM.

Does IC formation exclusively depend on nuclear auxin signaling?

To address the question whether nuclear auxin signaling is the predominant route by which auxin induces IC formation, I blocked nuclear auxin signaling by expression of the mutated AUX/IAA protein *bodenlos* (*bdl*) which does not respond to auxin and can repress the transcriptional influence of auxin. In a second approach, I addressed the question whether the auxin-dependent activation of the H^+-ATPase in the plasma membrane is a crucial step in cell wall modification during IC formation. I generated transgenic plant lines with an ethanol inducible H^+-ATPase (AHA2) that is constitutive active in the starch sheath after its induction. I made use of a ratiometric, pH sensitive, apoplastic marker to measure the pH of the cell wall after induction of the transgenic constructs.

2. Material and Methods

2.1. Model organisms and bacterial strains

2.1.1. Arabidopsis thaliana

In this study the ecotype Columbia (Col) of the model organism *Arabidopsis thaliana* was used. All used plant lines are listed in Table 1, marker lines were crossed if needed. Table 1: *Arabidopsis thaliana* lines used in this study. All plant lines are described in the plants database of the Greb lab (COS, Heidelberg, Germany).

Line	Origin	Reference
pSCR:AlcR, pAlcA:iaaM, pAlcA:GUS	Klaus Brackmann	unpublished
pSCR:AlcR, pAlcA:iaaM, pAlcA:GUS, pAlcA:pmei3	this dissertation	unpublished
pSCR:AlcR, pAlcA:GUS, pAlcA:pmei3	this dissertation	unpublished
pSCR:AlcR, pAlcA:iaaM, pAlcA:GUS, pAlcA:pmei5	this dissertation	unpublished
pSCR:AlcR, pAlcA:GUS, pAlcA:pmei5	this dissertation	unpublished
pSCR:AlcR, pAlcA:iaaM, pAlcA:GUS, pAlcA:pme3	this dissertation	unpublished
pSCR:AlcR, pAlcA:GUS, pAlcA:pme3	this dissertation	unpublished
pSCR:AlcR, pAlcA:iaaM, pAlcA:GUS, pAlcA:bdl	this dissertation	unpublished
pSCR:AlcR, pAlcA:GUS, pAlcA:bdl	this dissertation	unpublished
pSCR:AlcR, pAlcA:iaaM, pAlcA:GUS, pAlcA:AHAd94	this dissertation	unpublished
pSCR:AlcR, pAlcA:GUS, pAlcA:AHAd94	this dissertation	unpublished
pUB10::SYP122- pHusion	Karin Schumacher	Kesten et al. (2019)

pWOX4:YFP	Stefanie Suer	(Suer et al., 2011)
pPXY:YFP	Javier Agusti	(Agusti et al., 2011a)
pSCR:YFP	Pablo Sanchez	(Sanchez, 2013)
pDR5rev:GFP	Jiří Friml	(Benková et al., 2003)

Table 1 A. thaliana lines used in this study

2.1.2. Escherichia coli

The *Escherichia coli* (*E. coli*) genotype DH5α (Hanahan, 1983) was used for molecular cloning and plasmid amplification. For Amplification E. coli were grown in liquid LB medium while shaking (180 rpm) at 37 °C overnight (Innova44, New Brunswick Scientific Co., USA) until the culture had an optical density OD600 > 1. For selection *E. coli* was plated on LB plates containing the according antibiotics and grown in an incubator (UN110, Memmert, Buechenbach, Germany).

2.1.3. Agrobacterium tumefaciens

The Agrobacterium tumefaciens (*Agrobacteria*) genotypes C58C1: RifR with pSoup plasmid (TetR) or ASE: KanR, CamR with pSoup+ plasmid (TetR) were used (Ashby 1988, Fraley 1985, Hellens 2000). Growing conditions were typically liquid YEB medium at 28 °C overnight while shaking (180 rpm until OD > 1) (Innova 44, New Brunswick Scientific, USA).

2.2. Plasmids

2.2.1. Vectors used in this study

Name	Description	Resistance for bacteria	Origin	Reference
pGGA008	AlcA in module A	ampicilin	J. Lohmann	(Lampropoulos et al., 2013)
pVL50	dummy in module B	ampicilin	T. Greb	(Schürholz et al., 2018)
pSW190	pmei5 in module C	ampicilin	S. Wolf	(Wolf et al., 2012b)
pSW417	pmei3 in module C	ampicilin	S. Wolf	(Schürholz, 2019)
pSW354	pme3 in module C	ampicilin	S. Wolf	(Schürholz, 2019)
pTC13	BDL in module C	ampicilin	this dissertation	unpublished
pA700	HAH1 (d94)	ampicilin	Claudia Oecking	(Pacheco-Villalobos et al., 2016)
pTC12	HAH1(d94) in module C	ampicilin	this dissertation	unpublished
pVL51	dummy in module D	ampicilin	T. Greb	(Schürholz et al., 2018)
pGGE028	term35S in module E	ampicilin	J. Lohmann	(Lampropoulos et al., 2013)
pVL53	sulfR in module F	ampicilin	T. Greb	(Schürholz et al., 2018)
pVL11	backbone	spectinomycin	T. Greb	(Schürholz et al., 2018)

Table 2 Vectors used in this study

2.2.2. Constructs

Destination vector	Entry vectors (modules)						
	A	B	C	D	E	F	Z
AlcA:pmei5 (pTC9)	*pGGA008*	*pVL50*	*pSW190*	*pVL51*	*pGGE028*	*pVL53*	*pVL11*
AlcA:pmei3 (pTC6)	*pGGA008*	*pVL50*	*pSW417*	*pVL51*	*pGGE028*	*pVL53*	*pVL11*
AlcA:pme3 (pTC12)	*pGGA008*	*pVL50*	*pSW354*	*pVL51*	*pGGE028*	*pVL53*	*pVL11*
AlcA:bdl (pTC5)	*pGGA008*	*pVL50*	*pTC13*	*pVL51*	*pGGE028*	*pVL53*	*pVL11*

AlcA:AHAd94 (pTC9)	*pGGA008*	*pVL50*	*pTC12*	*pVL51*	*pGGE028*	*pVL53*	*pVL11*

Table 3 Self generated constructs used in this study

2.3. Primers

	Used for	Primer name	Primer sequence (5' to 3')
Genotyping	pAlcA:iaaM	AlcAprom-for	GCATCCCCGCATAGCTGAAC
		IAAMrev3	CTTCAAGAACGCACGCCA
	pAlcA:bdl	D-dummy_seq_1	GGgAATgAAGGTAAAGGT
		BDL exo R	CATCTCCAACAAGCATCCAA
	pAlcA:PME3, pAlcA:PMEI3, pAlcA:PMEI5	seq_GG_Z00_rvs	CCTTTTTACGGTTCCTG
		D-dummy_seq_1	GGgAATgAAGGTAAAGGT
	pAlcA:AHAd94	AHA1_forw1	CGGTAAAGCTGCTCACCTTGTGG
		D-dummy_seq_1	GGgAATgAAGGTAAAGGT
RT-PCR	WOX4	WOX4 qPCR F	CCTCCGGCGTCACTTCAG
		WOX4 qPCR R	GGGTTCCACCTTGTCCCTC
	PXY	PXYrev	GAGAGAGGTCGAGGGAAATG
		PXYfor16	ACCACACTTCCTCAAACAAC
	iaaM	IAAM fw1	ACCTGATGCTGAAGGGTTCG
		IAAM rev1	CCAAAGCTTGCCTCCAACAC
	SAUR19	SAUR19 F	ACCGTCATTTCAAGCTCTGC
		SAUR19 R	TTCATTGGAGCCGAGAAGTC
	ACT2	qACT2f	GCCATCCAAGCTGTTCTCTC
		qACT2r	ACCCTCGTAGATTGGCACAG
	UBQ10	UBQ1	gatctttgccggaaaacaattggaggatggt
		UBQ2	cgacttgtcattagaaagaaagagataacagg
Cloning	BDL in module C	bdl_forw_moduleC	AACAGGTCTCAGGCTCAATGCGTGGA ACAGGTCTCACTGACTA AATAGGGTTGTTTC
		bdl_rev_moduleC	AACAGGTCTCACTGACTAAATAGGGTT GTTTC
	AHAd94 in module C	AHA1_forw_moduleC	AACAGGTCTCAGGCTCAATGTCGAGT CTCGAAG
		AHA1_rev_moduleC	AACAGGTCTCACTGACTAAAACAAGTT GAGCC
	35Sterm in module E	35Sterm_for_moduleE	AACAGGTCTCACTGCCATAAATAATGT GTGAG

		35Sterm_rev_moduleE	AACAGGTCTCATAGTAGATCTGGATTTTAGTAC
Sequencing	pAlcA:PME3, pAlcA:PMEI3, pAlcA:PMEI5, pAlcA:bdl	seq_GG_Z00_rvs	CCTTTTTACGGTTCCTG
		seq_GG_N001_fwd	TCTAGTCTTTCAATTGTG
		D-dummy_seq_1	GGgAATgAAGGTAAAGGT
		D-dummy_seq_2	TAACCTTTACCTTcATTcCC
	pAlcA:AHAd94	AHA1_forw1	CGGTAAAGCTGCTCACCTTGTGG
		AHA1_forw2	GCGTGGTCTTAGGTCGTTGGCTG
		seq_GG_N001_fwd	TCTAGTCTTTCAATTGTG
		D-dummy_seq_1	GGgAATgAAGGTAAAGGT
		D-dummy_seq_2	TAACCTTTACCTTcATTcCC
	35Sterm in module E	35Sterm-rev	AAGAACCCTAATTTCCCTTATCGG

Table 4 Primers used in this study

2.4. Chemicals

All chemicals that were used in this study were shared between the research groups of Prof. Dr. Jan Lohmann and Prof. Dr. Thomas Greb (COS Heidelberg, Germany). They are all listed in the common and publicy accessible Dangerous Materials Registry Information System (DaMaRIS) that is provided by the University of Heidelberg, Germany.

2.4.1. Buffers and solutions

Use	Buffer/ solution	Content
Extraction of genomic DNA	Extraction buffer	200 mM Tris (pH 7.5) 250 mM NaCl 0.5 % SDS 25 mM EDTA
	10 x TE buffer	100 mM Tris (pH 8) 10 mM EDTA (pH 8) 0.1 M NaCl 2 % SDS
RNA extraction	Extraction buffer	50 mM Tris/HCl (pH 9) 10 mM EDTA 20 mM β-mercaptoethanol (added freshly)

Gel electrophoresis	1L 50 x TAE buffer	242 g TRIS 100 ml EDTA (0.5 M) 57.1 ml Acetic acid pH 7.6
	DNA ladder (Thermo-Scientific; Waltham, USA)	GeneRuler 1 kb DNA Ladder #SM0311 MassRuler Low Range DNA Ladder #SM0383
Immunohistochemistry	2F4 Buffer	20mM Tris-HCl, 1mM $CaCl_2$ 150 mM NaCl, pH 8.2

Table 5 Buffers and solutions used in this study

2.4.2. Antibiotics

Antibiotics stocks:

- 100 mg/mL ampicillin (Sigma-Aldrich; St. Louis, USA)
- 25 mg/mL chloramphenicol in ethanol (Roth; Karlsruhe, Germany)
- 50 mg/mL kanamycin (Roth; Karlsruhe, Germany)
- 100 mg/mL spectinomycin (Sigma-Aldrich; St. Louis, USA)
- 100 mg/mL sulfadiazine (Sigma-Aldrich; St. Louis, USA)
- 10 mg/mL tetracycline in ethanol (Sigma-Aldrich; St. Louis, USA)
- 100 mg/mL rifampicin (Sigma-Aldrich; St. Louis, USA)
- Hygromycin B (50 mg/mL, Roche; Basel, Switzerland)

2.4.3. Dyes

- Toluidine blue, 50 mg/mL (AppliChem, Darmstadt, Germany)
- DirectRed23, 0.1 % (Sigma Aldrich, St. Louis, USA)
- Propidium iodide, 10 µg/mL (Sigma Aldrich, St. Louis, USA)
- Ethidium bromide solution, 0.025 % (Karl Roth, Karlsruhe, Gemany)

2.4.4. Antibodies for immunohistochemistry

Name	Epitope	Host species	Work concentration	Origin	Reference
2F4	Homogalacturonan	Mouse	1/100	PlantProbes	(Liners et al., 1992)
LM20	Homogalacturonan	Rat	1/100	PlantProbes	(Verhertbruggen et al., 2009)
LM19	Homogalacturonan	Rat	1/100	PlantProbes	(Verhertbruggen et al., 2009)
LM1	Extensin	Rat	1/100	PlantProbes	(Leroux et al., 2007)
Alexa488	Mouse	Goat	1/1000	Thermo Fisher Scientific	(Gonzalez-Perez et al., 2018)
Alexa488	Rat	Goat	1/1000	Thermo Fisher Scientific	(Li et al., 2018)
Alexa647	Rat	Goat	1/1000	Thermo Fisher Scientific	(Sasaki et al., 2019)

Table 6 Antibodies used in this study

2.5. Standard plant work and growth conditions

2.5.1. Seed sterilization and stratification

Seeds were vapor sterilized using 40 mL commercial bleach, adding 4 mL of concentrated hydrochloric acid. Seeds and bleach containing beaker where placed in a desiccator with closed lid for around 5 hours. Sterile seeds were stratified in micro centrifuge tubes in dH_2O at 4 °C in the dark for at least three days.

2.5.2. Plant growth, induction and seed collection

For histological sectioning, stratified seeds were distributed and grown on standard soil (Patzer, Sinntal-Altengronau, Germany) mixed with 1: 4 perlite (Perligran extra, Knauf, Iphofen, Germany) in growth chambers under short day (SD) conditions (12 h light, 12 h dark) at 23 ° C and 65 % humidity for three weeks, then transferred to growth chambers with long day conditions (16 h light, 8 h dark) at 23 ° C and 65 % humidity.

After two to three weeks in LD condition they started bolting and where treated with ethanol or control condition. For ethanol treatment plants where put under a dome with two petri dishes with 15 mL 70 % ethanol two allow evaporation overnight (around 15-17 h). Plants were harvested three, five or ten days after the treatments (DAT). For seed collection plants were placed in a drying chamber (constant light) for two weeks before collection. Selection of transformed plants was performed on ½ MS Plates containing the according antibiotics.

2.6. Tissue staining

2.6.1. Propidium iodine staining

Fresh hand cut sections of stems were incubated for 5 - 7 min with 10 µg/mL PI dissolved in sterile de-ionized water to visualize lignified secondary cell walls by confocal microscopy. PI-stained tissues were excited with the DPSS laser line at 561 nm and detected with the PMT at 590-690 nm.

2.6.2. DirectRed23 staining

Fresh hand cut sections of stems were incubated for 5 - 7 min with 0.1 % direct red 23 dissolved in sterile de-ionized water to visualize cell walls by confocal microscopy. Tissues stained with direct red 23 were excited with the DPSS laser line at 561 nm and detected with the PMT at wavelength 660 nm.

2.6.2. Toluidine blue staining

see histology (2.7.)

2.6.3. GUS staining

To make the β-glucuronidase reporter visible the GUS staining with X-Gluc (5-bromo-4-chloro-3-indolyl glucuronide) (Roth, Karlsruhe, Germany) developed by R.A. Jefferson et al. (1987) was used. Freshly harvested sample material (stem or leave) was dipped in 2 mL tube filled with GUS staining solution with freshly added potassium ferricyanide and potassium ferrocyanide (final concentration 0.5 mol/L) and X-Gluc (final concentration 1mM). Samples were incubated at 37 °C over night

after a possible vacuum infiltration (30 min, approx. 500 mbar). Blue staining was visible after incubation and staining solution was removed and replaced by 30 %, 50 % and 70 % ethanol solution successively for 1 hour each solution. After the last step, the samples were stored in a renewed 70 % ethanol solution until being processed for histology (2.7).

2.7. Histology

After incubation of harvested material (1 cm stem fragments of the second internode) in 70 % ethanol for at least 5 days at 4 °C, samples were processed by the Leica ASP 200S tissue fixation machine. After fixation, samples were transferred to the paraffin embedding centre EG1160 (Leica Microsystems, Mannheim, Germany) and embedded in paraffin. Using the microtome RM2235 (Leica Microsystems, Mannheim, Germany), stem sections with a thickness of 8 µm were cut and collected on a water film on a microscopy slide (Superfrost Microscope Slides (Thermo-Scientific, Waltham, USA). The paraffin sections stretched onto the water film and dried overnight on a heating plate at 42 °C. Dry sections were de-paraffinised and stained with Toluidine blue as described below:

De-paraffinising		**Toluidine blue staining**	
Histo-Clear™	10 min	0.05 % Toluidine blue solution	5 – 8 min
Histo-Clear™	10 min	H_2O (tab water)	rinsing
100 % ethanol	1 min	H_2O (tab water)	1 min
100 % ethanol	1 min	85 % ethanol	0.5 min
95 % ethanol	1 min	95 % ethanol	0.5 min
85 % ethanol	1 min	100 % ethanol	0.5 min
50 % ethanol	1 min	100 % ethanol	0.5 min
30 % ethanol	1 min		
H_2O (tab water)	5 min		

Table 7 De-paraffinising and Toluidine blue staining protocol for histology

After letting the sample air-dry for one to three hours they were embedded in Micromount Mounting Media (Leica Microsystems, Mannheim, Germany) and again air-dried for at least three days. Samples were scanned using the slide scanner Pannoramic SCAN II (3DHistech, Budapest, Hungary) and analyzed by the software

CaseViewer 2.2 (3DHistech, Budapest, Hungary). Data were processed in Microsoft Excel (Microsoft, Redmond, USA) and R (R-studio, Boston, USA).

2.8. Extraction of genomic DNA and genotyping of *Arabidopsis thaliana*

Rosette leaves were harvested in a 1.5 mL tube with two glass beads and placed in N2(l) immediately. Samples were grinded 30 secs at top speed at the using the mixer mill MM 400 (Retsch, Haan, Germany). 300 µL of DNA extraction buffer was added and tubes were inverted several times. Samples were centrifuged for 1 min at maximal speed at room temperature. Supernatant was transferred in new tubes, 150 µL Isopropanol were added and samples was centrifuged again for 5 min at maximal speed at room temperature. A DNA containing pellet was formed and the supernatant was poured. 700 µL of 70 % ethanol was added and the samples were centrifuged again for 1 min. at maximal speed at room temperature. Supernatant was removed and the pellet was allowed to air-dry. To dissolve the DNA 150 µL of de-ionized, autoclaved water was added and samples were incubated at 65 °C for 10 min. Genotyping of Arabidopsis was performed using 1 µl of DNA solution and the Taq DNA Polymerase, recombinant (5 U/µL) kit (Thermo-Scientific; Waltham, USA). Genotyping PCRs and thermocycler settings were set up as recommended by the manufacturer. To design primers for genotyping CLC Main Workbench 7 (CLC Bio Qiagen, Aarhus, Denmark) was used, Genotyping primers can be found in table (2.3).

2.9. Gel electrophoreses

Agarose was melted in TAC-buffer using the microwave and let cool down for approximately 4 min. The agarose concentration depends on the PCR product and has to be adjusted. Ethydiumbromide was added to the agarose (1 drop of 0.025 % solution per 20 mL agarose gel) (Roth, Karlsruhe, Germany) and let solidify in a gel tray with appropriate number of pockets. After loading the PCR products and an appropriate ladder, the electrophoresis was running 30 - 90 min. at 100 V.

2.10. RNA extraction and processing

2.10.1. RNA extraction

To extract RNA, segments of the stem at the second internode were harvested in a 1.5 mL tube and placed in N2(l) immediately. Plastic pestles were used to grind the samples within one min. under constant cooling and adding of 450 µl of RNA extraction buffer. Samples were vortexed, 500 µl of phenol and 500 µl of chloroform were added and the samples were vortexed again. After centrifugation with 13000 rpm for ten min. at 4 °C the aqueous phase was recovered and 500 µl phenol and 500 µl chloroform were added. Samples were vortexed again and centrifuged with 13000 rpm for 10 min at 4 °C. Aqueous phase was recovered and mixed with 500 µl chloroform to remove remaining phenol, vortexed and centrifuged at 13000 rpm for 10 min. at 4 °C. RNA was allowed to precipitate over night after adding 1/10 of the volume of 3 M sodium acetate (pH 3.5) and three times the volume of cold ethanol. Samples were centrifuged at 13000 rpm at 4 °C and the supernatant was poured out. Ice cold ethanol was added (1000 µl) and the samples was centrifuged again for 5 min at 13000 rpm at 4 °C. This washing step was repeated two times. Supernatant was poured out carefully and the pellet was allowed to dry. RNA pellet was resuspended in 30 µl ddH2O (RNAse free). The RNA concentration was measured using a NanoDrop ND-1000 (ThermoSci-entific; Waltham, USA).

2.10.2. cDNA synthesis

To remove residual genomic DNA, the extracted RNA was treated with DNAse I, RNAse free (ThermoScientific, Waltham, USA) and tested for genomic DNA contamination. cDNA synthesis was performed following the instructions of the Thermo Revert Aid Kit (ThermoScientific; Waltham, USA). As negative control the volume of the reaction buffer was exchanged by water. Quality of the cDNA was checked by PCR with primers for the housekeeping gen ACTIN2. In case of a contamination with genomic DNA, DNAse treatment was repeated.

2.10.3. Sequencing

For sequencing, RNA was extracted from the second internode (max. 1 cm) of three stems, pooled together for one biological replicate. Three biological replicates were collected per genotype and treatment. To remove residual genomic DNA, samples were treated with DNAse according to the protocol of DNAse and RNAse free (Thermo Sientific, Waltham, USA) as described above. Library preparation and next generation sequencing was performed at the Deep Sequencing Core Facility provided by the Exzellenzcluster CellNetworks at the University of Heidelberg (http://www.cellnet-works.uni-hd.de/483065/Deep_Sequencing_Core_Facility). Single reads of 50 nucleotides in length were sequenced using Illumina HiSeq 2500 machine. Reads were aligned to the *Arabidopsis* genome (TAIR10) using TopHat2 v2.0.14 (Kim et al. 2013) and the statistical analysis was done by Dr. Dongbo Shi using the DESeq2 package from the R/Bioconductor software (Love et al. 2014). Ethanol treated transgenic lines were compared to ethanol treated wild type (p value < 0.01, Wald test). GO enrichment analysis was carried out using PANTHER (v 14.1) provided by TAIR (https://arabidopsis.org/tools/go_term_enrichment.jsp).

2.11. Generation of new transgenic lines

2.11.1. Molecular cloning (Green gate cloning)

All constructs that were cloned during and for this study were obtained using the method of GreenGate cloning (Lampropoulos et al. 2013). The two entry vectors that were newly generated were obtained in a PCR reaction using correspondingly designed primers to add a GreenGate module specific sequence and an Eco31I enzyme recognition site. Entry module-specific primers were designed in silico using CLC Main Workbench 7 (CLC Bio Qiagen, Aarhus, Denmark). To purify the PCR products agarose gel electrophorese was used, and bands with expected band length were illuminated using an UV Transilluminator (VWR International, Darmstadt, Germany), cut out and purified using the Wizard® SV Gel and PCR Clean-Up System (Promega, Madison, USA) for gel purification.

To ligate purified gene fragments with empty entry vectors both components were first digested with Eco 31I enzyme and purified using the QIAquick OCR Purification Kit (Quiagen, Venlo, Netherlands). DNA insert and vector were then ligated using the T4 DNA ligase (Thermo Scientific, Waltham, USA) in a ratio of five to one. After 20 min at 65 °C (heat inactivation) the plasmids were amplified using chemical competent *E. coli* (DH5α) growing on ampicillin (1:2000) containing LB plates. Vectors were isolated from bacterial colonies with the help of the QIAprep Spin Miniprep Kit (Qiagen, Venlo, Netherlands) and sent for Sanger sequencing (Eurofins, Ebersberg, Germany) after successful digestion with two to three digestion enzymes.

All entry vectors and the empty destination vector were mixed in one reaction including ATP, T4 DNA Ligase and the fast digest Eco31I enzyme to create the final construct. After the ligation and inactivation by heat, competent *E. coli* (DH5α) growing on spectinomycin LB plates were used to amplify the plasmid. To isolate the destination vectors from positive colonies, the QIAprep Spin Miniprep Kit (Qiagen, Venlo, Netherlands) was used. After digestion with two or three digestion enzymes, samples were sent for Sanger sequencing (Eurofins, Ebersberg, Germany).

2.11.2. Transformation of Agrobacterium tumefaciens

To transform Agrobacteria (C58C1), 500 ng of the purified plasmids were incubated with 500 µL Agrobacteria for 5 min on ice, frozen in $N_{2(l)}$ for five minutes and heat shocked for another 5 min at 37 °C while shaking. Agrobacteria were incubated for 2 - 4 hours at 28 °C in 800 µL liquid YEB medium while shaking. 200 mL of the bacterial solution was spread on YEB plates containing rifampicin (1:2000), tetracycline (1:2000) and spectinomycin (1:2000) and grown for 2 – 3 days at 28 °C until colonies appeared. Glycerol stocks were generated by picking individual colonies and growing them in 10 mL liquid YEB, containing the above mentioned mixture of antibiotics, for up to 24 hours until the medium became turbid. 250 µL of Agrobacteria were mixed with 750 µL sterile glycerol (80 – 100 %), immediately frozen and stored at – 80 °C.

2.11.3. Transformation of Arabidopsis thaliana

The floral dip method (Clough and Bent, 1998) was used to generate transgenic lines of *Arabidopsis thaliana*. Agrobacteria transformed with the construct of interest as described in 2.12.2 were cultured in 200 mL YEB with the respective antibiotics. The turbid culture was centrifuged at 4000 rpm for 15 min., the pellet was washed with 10 mL infiltration medium and re-suspended in 150 mL infiltration medium with SILWET. Flowering Arabidopsis thaliana were dipped into the bacterial solution for 5 min. Afterwards plants were incubated in the dark over night before they were transferred into LD condition growth chamber. The seeds of transformed plants were harvested about 2 weeks after the transformation. To select for successful transformants, T1 seeds were sawn on MS plates containing the respective antibiotic or herbicide. To enlarge the probability for single copy lines that are more stable T2 transformants were grown on MS plates containing the respective antibiotic or herbicide and analyzed with respect to there segregation ratio, if possible transformants T3 with a one to three segregation ration in T2 was used for experiments

2.12. Fluorescence confocal microscopy

Fluorescent confocal microscopy was performed on a Leica TCS SP8 II (Leica Microsystems, Mannheim, Germany). To obtain fluorescent signal from stem cross sections a 20x multi-immersion objective as used. To excite the fluorescent signal, an argon or a DPSS laser was used, collecting the emission either via a PMT or a HyD detector. Applied fluorescent proteins, secondary antibodies or dyes are listed below with their excitation wavelength and the range of emission that was collected.

Fluorescent protein/ sec. antibody/ dye	$\lambda_{exc.}$ [nm]	$\lambda_{exc.}$ [nm]
YFP (yellow fluorescent protein)	514	520 - 540
GFP (green fluorescent protein)	488	500 - 570
PI	561	590 - 690
Direct red 23	561	> 660

Alexa 488	488	505 - 545
Alexa 647	633	> 650

Table 8 Settings for confocal fluorescence microscopy used during this study

To prevent cross-talk, a sequential scan was used if two or more fluorescent signals were present in one sample. Images were saved and reviewed using the Leica Application Suite X (LAS X) software. To analyze the intensity or localization of the fluorescent signal imageJ (v. 1.50) was used.

2.13. Immunohistochemistry

Monoclonal antibodies were purchased from Plant Probes (Paul Knox Lab, Leeds, UK) to perform single or double immune staining of cell walls. The protocol for the single immune staining was taken from Dr. Jiyan Qi and adapted with suggestions from Dr. Alexis Peaucelle to obtain a protocol for double immune staining of cell walls.

2.13.1. Fixation

Stem segments of the second internode were harvested and dipped in pre-cold 100 % methanol and vacuum infiltrated two times every 15 min. (approx. 500 mbar). Fixative was exchanged each time. Samples were incubated over night at -20 °C in fresh methanol.

2.13.2. Dehydration

Samples were washed successively with 30 %, 50% and 70 % ethanol each for 30 min on ice, after this step, samples could be stored. To dehydrate the samples further, they were washed successively with 80 %, 90 % and 96 % ethanol each for 30 min on ice and at last incubated for one hour in 100 % pre-heated ethanol at 37 °C.

2.13.3. Embedding in Steedman's wax

Following steps took place in a 40 °C incubator to keep the wax liquid and allow to infiltrate into the tissue. Steedman' s wax is a low temperature melting wax (fresh mixture of PEG 400 di-stearate (Sigma Aldrich, Darmstadt, Germany), and 1-Hexagecanol (Sigma Aldrich,

Darmstadt, Germany)) stays liquid at 40 °C and solidifies quickly at temperatures < 25 °C. Samples were incubated in 50 % wax/ 50 % ethanol over night. Wax-ethanol mixture was exchanged for 75 % wax/ 25 % ethanol and samples were kept in there for four hours. After this samples were incubated at least two times in fresh 100 % wax to remove the alcohol and transferred to cassettes for embedding.

2.13.4. Sectioning

Sections of 6 μm thickness were cut with the help of the microtome RM2235 (Leica Microsystems, Mannheim, Germany). Sections were transferred on water films on poly-Lysine-coated slides (Leica Microsystems, Mannheim, Germany) to allow the sections to stretch themselves. Water was removed and sample was air dried over night.

2.13.5. Immunolocalization

Dewaxing and rehydrating

Slides were dipped in 100 % ethanol to remove the wax between the samples. Sections of interest were surrounded by a hydrophobic PAP-pen. For rehydration samples were subsequently dipped for 10 min. into 96 %, 90 %, 70 %, 50 %, 25 % ethanol and afterwards rinsed with water.

Blocking and incubation with first primary antibody

To block the non-specific sites, the samples were dipped for one hour in two % BSA in 2F4 buffer and rinsed afterwards for 5 min. with 2F4 buffer. The required antibody was diluted in buffer containing 0.1 % BSA and added dropwise in the surrounded areas on the slides. The antibody was left for hybridization on the sample for 3 - 18 hours (usually four hours) at room temperature. After the incubation the remaining free antibody was washed away by bathing the slides for 10 min. in 2F4 buffer, 15 minutes in 2F4 buffer containing 0.3 % Tween20 (Sigma Aldrich, Darmstadt, Deutschland) and 10 min. in 2F4 buffer subsequently.

To block the non-specific sites, the samples were dipped for one hour in two % BSA in 2F4 buffer and rinsed afterwards for 5 min. with 2F4 buffer. The required antibody was diluted in buffer containing 0.1 % BSA and added dropwise in the surrounded areas on the slides. The antibody was left for hybridization on the sample for 3 - 18 hours (usually four hours)

at room temperature. After the incubation the remaining free antibody was washed away by bathing the slides for 10 min. in 2F4 buffer, 15 minutes in 2F4 buffer containing 0.3 % Tween20 (Sigma Aldrich, Darmstadt, Deutschland) and 10 min. in 2F4 buffer subsequently.

Incubation with second primary antibody

If necessary, samples were incubated with a second primary antibody; the procedure was as described above).

Hybridization with second antibodies

To visualize the localisation of the primary antibodies, fluorescent secondary antibodies were used. Secondary antibodies were diluted in 2F4 buffer containing 0.1 % BSA, added dropwise onto the region of interest of the sample on the slide and let cure in for 2 - 4 hours. Remaining free antibodies were washed by bathing slides for 10 min in 2F4 buffer, 15 min in 2F4 buffer containing 0.3 % Tween20 (Sigma Aldrich, Darmstadt, Germany) and 10 min in 2F4 buffer subsequently.

Counterstaining and mounting

Cell walls were counterstained using propidium iodide (0.01 % in 2F4 buffer) for about 5 min. Spare propidium iodide was washed away with 2F4 buffer for 1 min. Samples were mounted in Prolong Gold antifade (Thermo-Scientific, Waltham, USA) and imaged immediately by fluorescent confocal microscopy.

2.14. Brillouin confocal microscopy

2.14.1. Instrumentation

To obtain Brillouin spectra of diverse materials and biological samples a home built Brillouin microscope with a two-VIPA spectrometer was used (G. Scarcelli and S. H. Yun (2011)). Main parts and first assembly was realized by Dr. Kareem Elsayad (Head of the Advanced Microscopy facility at the Vienna Bio Center). Finalization and software development of the Brillouin microscope set-up was done by Dmitry Richter (Harvard Medical School and Massachusetts General Hospital). The microscope is equipped with a Cobolt Samba single frequency CW diode pumped

laser (Cobolt, Solna, Sweden) operating at 532.1 nm. The Nikon eclipse Ti-U microscope body (Nikon, Tokyo, Japan) is equipped with a ASI-stage (Applied Scientific Instrumentation, Eugene, USA), a Basler ac-u camera (Basler, Ahrensburg, Germany) and a mercury lamp (Nikon, Tokyo, Japan) for bright field observations. Brillouin spectra were resolved by a homebuilt two VIPA (virtual image phase array) Brillouin spectrometer with an integrated Lyot stop which enhances the signal contrast (Edrei et al., 2017b). A PCO.edge camera (PCO AG, Kehlheim, Germany) was used to record the spectra. The microscope and the spectrometer were coupled by a single mode fiber.

2.14.2. Operation

To ensure optimal operation of the Brillouin microscope set-up component specific maintenance measures and frequent instrumental alignment are necessary. Running the laser at maximum power (100 mW) for at least one hour prior a Brillouin experiment stabilizes the laser output and prevents signal drifting. To regulate the laser power at the sample a continuously variable, metallic Neutral Density (ND) filter (Thorlabs, Ely, USA) was used and typically adjusted to 5 mW to avoid photo damages. For the optimization of the single-mode fiber coupling a highly reflective mirror was placed on the sample holder. Back reflected light was focused into a single-mode fiber which transfers the light to the spectrometer, and the coupling efficiency was analyzed by comparing the power of the incident light before the fiber coupler with the power behind the collimation lens of the fiber exit using a powermeter (Thorlabs, Ely, USA). The coupling efficiency should be at least 30% to ensure sufficient signal transduction. After optimizing the light coupling the mirror was replaced with a water filled plastic petri dish (MatTek, Ashland, USA) to evaluate the water Brillouin signal which was used as a reference. Here, the stage had to be moved in order to assure that the focal point of the objective lens lies within the water. Now PCO camera could be switched on and the signal was checked by using the open source software MicroManager 1.4. Positioning of the slits within the VIPA-spectrometer is important to check, to avoid overexposure of the camera with stray light. Furthermore, position and angle of the VIPAs need to be readjusted to increase the throughput and to obtain a nearly

symmetric signal across the whole spectrum. Depending on the sample and its optical properties the iris of the lyot stop located in front of the camera was adjusted in order to increase the signal to noise ratio by suppressing diffraction of the stray light.

2.14.3. Data acquisition

After successful (re-)alignment of the Brillouin spectrometer a customized MatLab script operating the microscope, written by Dmitry Richter, can be started. This script is used to drive the PCO camera, the Basler brightfield camera and the microscope stage. It allows to perform raster-scans of the sample which result eventually in representation of Brillouin maps. Parameters that can be chosen freely are acquisition time per single spectrum (typically 550 ms), pixel size (typically 1 μm), start position of the scan and the area that should be scanned. Prior to scanning, the spectral line across the recorded PCO camera image containing the signal has to be selected over which peak finding and signal fitting are performed. During the scan the recorded spectrum was tracked automatically.

It is also possible to capture the brightfield images while performing the Brillopuin scan. For this purpose, the filter needs to be changed from the bandpass filter that is used for the Brillouin signal acquisition only to the dichroic filter that makes it possible to see the Brillouin signal and the brightfield image simultaneously.

2.14.4. Spectral analysis

The Brillouin spectra are acquired along a spectral line between two Rayleigh peaks. The width of the spectral line over which values are being averaged can be set (typically set to be 3). To analyze the spectra a signal calibration with water is needed beforehand. The positions of the two calibration Brillouin peaks as well as the background level are marked by hand to facilitate the peak finding. Peaks are fitted with a Voigt function (“broadened” Lorenzian profile). The calculated peak position of the water signal is then assigned to the known Brillouin shift of water (M'_{water} = 7.46 GHz) which serves as a reference. The positions of the acquired Brillouin peaks are then set in relation to the positional information of the calibration Brillouin peak of water to get information

about the shift of each peak in GHz. Additionally, information about peak height and FWHM (full width at half maximum) are obtained. After the spectral analysis, three matrices (saved as .txt files) are attained with the Brillouin peak shift, intensity and FWHM as entries.

2.14.5. Data analysis

Each matrix represents the scanned area and every matrix entry corresponds to a pixel value in a Brillouin peak shift, intensity and FWHM map, respectively. To transform the .txt file into a map ImageJ was used.

2.14.5. Sample preparation

Root

Seedlings were grown 5 days on vertical full MS plates in LD condition after 2 days of stratification at 4 °C in the dark. Seedlings were placed on glass bottom dishes with No. 0 coverglasses (MatTek, Ashland, USA) and covered with an agar pad before imaging.

Shoot apical meristem

Shoot apical meristems (SAMs) was harvested from 10 – 15 cm tall plants and dissected under a stereo microscope Stemi 2000-C (Carl Zeiss; Oberkochen, Germany). After incubation of the samples with isoxaben or control treatment over night SAMs were transferred to the EMBL. SAMs were placed in petri dishes filled with 5 % agarose and fixed with 1 % low melting agarose. The petri dish was placed up side down on the water droplet on the water immersion objective (40x, NA = 1.2) (Nikon, Tokyo, Japan) so that the SAM was fully immersed in the droplet.

2.16. Figures and illustrations

All data presented in this study was assembled into figures using the open source software Inkscape 1.0 (Inkscape, New York, USA)

3. Results

3.1. Enhanced auxin biosynthesis in starch sheath cells leads to the formation of cells with cambium identity in the interfascicular region

During secondary growth initiation cells with cambium identity that are restricted to the vascular bundles in the upper stem and will finally form a closed cylinder that is able to produce new tissue in a bifacial manner. The starch sheath was determined as the origin of de-novo formed cambium cells in the interfascicular region in a clonal analysis using an ethanol inducible system to express YFP in starch sheath progeny after agglomeration of auxin (application of NPA) (Sanchez, 2013). Also Altamura et al. found the interfascicular cambium (IC) was mainly produced by starch sheath cells (Altamura et al., 2001).To investigate this process further, I analyzed an ethanol inducible system to express the bacterial auxin biosynthesis gene iaaM under the starch sheath specific SCARECROW promoter (Romano et al., 1995).

3.1.1. Histology in a time resolved manner

To examine the process of *de novo* formation of interfascicular cambium I worked with a transgenic line, allowing the induction of auxin biosynthesis in a tissue-specific manner. I used the starch sheath specific *SCRAECROW* promoter (Wysocka-Diller et al., 2000) to drive an ethanol inducible transgene (Roslan et al., 2001) expressing the bacterial auxin biosynthesis gene *iaaM* (Romano et al., 1995) but also *β–glucuronidase* (*GUS*), a reporter gene (Ulmasov et al., 1997) (Figure 8).

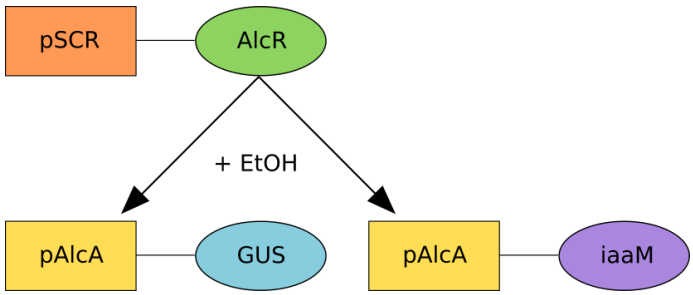

Figure 8 ***Scheme of the construct to express iaaM and the β-glucuronidase (GUS) ethanol inducible under the starch sheath specific SCARECROW promotor (pSCR).***

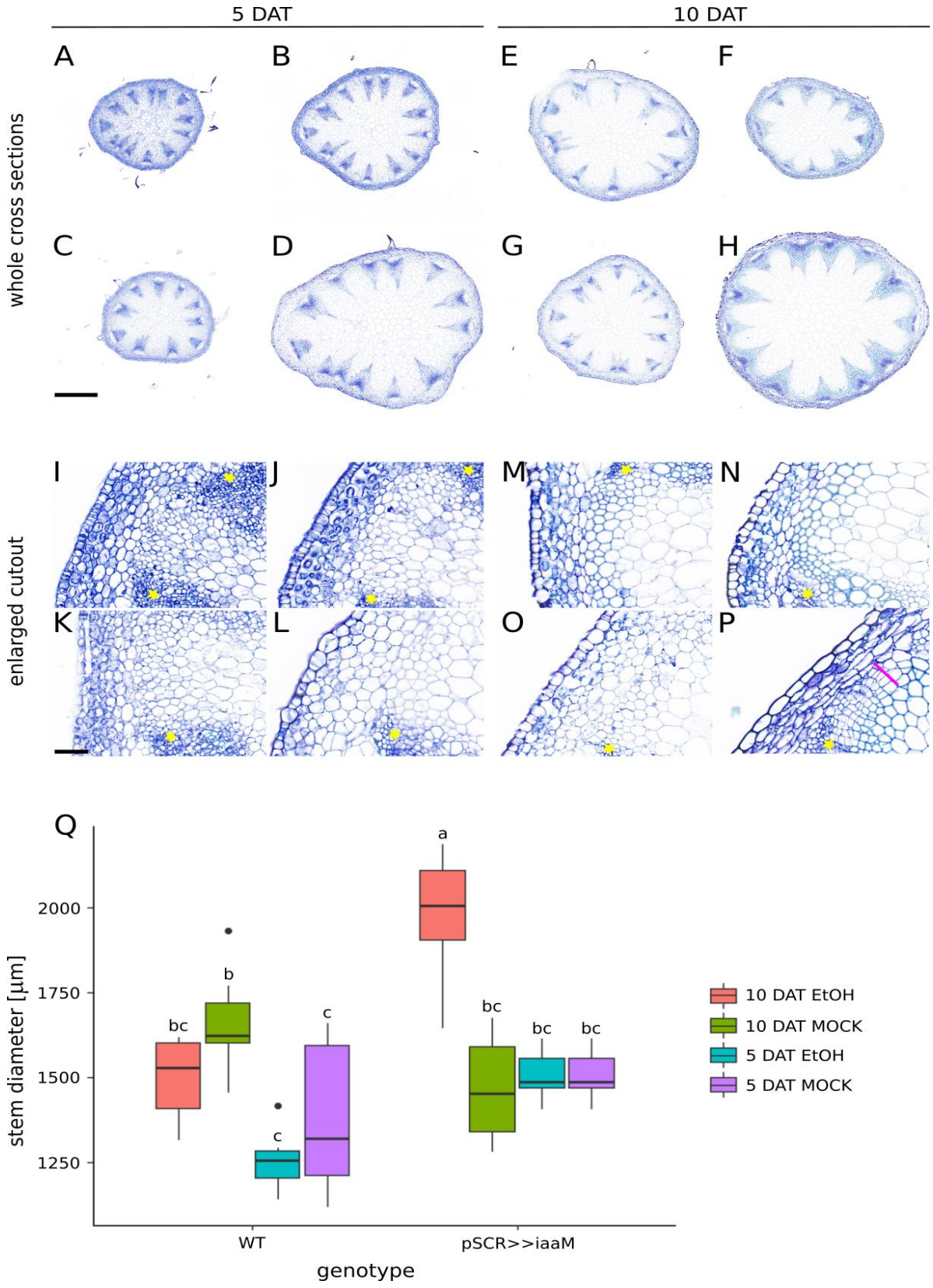

Figure 9 ***Auxin induced cell file formation in ethanol treated transgenic lines is visible 10 days after ethanol treatment (DAT).*** *Toluidin blue stained cross sections of the second internode of the wild type at 5 DAT (A, I) and ethanol treated wild type at 5 DAT (C, K), pSCR:AlcR, pAlcA:iaaM control treated at 5 DAT (B, J), pSCR:AlcR, pAlcA:iaaM ethanol treated at 5 DAT (D, L) and wild type at 10 DAT (E, M) and ethanol treated wild type at*

10 DAT (G, O), pSCR:AlcR, pAlcA:iaaM control treated at 10 DAT (F, N), pSCR:AlcR, pAlcA:iaaM ethanol treated at 10 DAT (H, P) vascular bundles highlighted with a yellow asterisk, de-novo formed cell files are indicated with a purple line. Upper Scale bar equals 500 µm, lower scale bar equals 50 µm. Only ethanol treated plants with the pSCR:AlcR, pAlcA:iaaM construct show 10 DAT the formation of cell files (P). Analysis of the stem diameter revealed a massive thickening of the stem of about 30% compared to wild type and the control. Statistical significant difference of stem diameter is revealed using ANOVA.

To monitor the effect of induction of auxin biosynthesis I performed a histological analysis using toluidine blue stained cross sections of the second internode, a region with primary growth conformation, meaning no cambium in the interfascicular region. To study the dynamics underlying the system I harvested samples for histology 5 days (Figure 9; A – D and I – L) and 10 days (Figure 9; E – H and M – P) after the treatment (5 DAT, 10 DAT). Interestingly I could observe the formation of cell files in the interfascicular region between the vascular bundles in samples of the transgenic line with enhanced auxin biosynthesis in the starch sheath as a consequence of *iaaM* expression, which was never the case for samples from the control and wild type plants. The formation of cell files was observed in 85 % of the cross sections in ethanol induced transgenic plants from samples that where harvested at 10 DAT. At 5 DAT cross sections of the ethanol induced transgenic plants showed cell files in 16 % of cross sections. None of the untreated transgenic plants and wild type controls showed cell files in the interfascicular region. Another phenotypical observation was an increase of stem diameter (Figure 9, I)**Error! Reference source not found.**. Ethanol treated transgenic plants showed an up to 30 % increased stem diameter when harvested 10 DAT in comparison to wild type plants and untreated controls.

Taken together, inducing auxin biosynthesis in starch sheath cells via an ethanol inducible system was able to initiate cell files in the interfascicular region in the second internode of the stem and promote thickening of the stem.

The same transgenic system expressed β-glucuronidase (GUS) as well under the *SCARECROW* promoter (p*SCR*) in an ethanol inducible manner, so that the success of induction could be visualized by GUS-staining (Figure 10). Only the ethanol induced transgenic plants, that carried the GUS, show blue GUS-staining that is restricted to the starch sheath cells. Cells of the cell files did not show blue staining, which can

be taken as the first indication of a different identity of the de-novo formed cells in the files because GUS is only in starch sheath cells expressed. The GUS-staining can also be used as a control for the restricted locality of the construct. It implies that expression of *iaaM* is limited to the starch sheath cells.

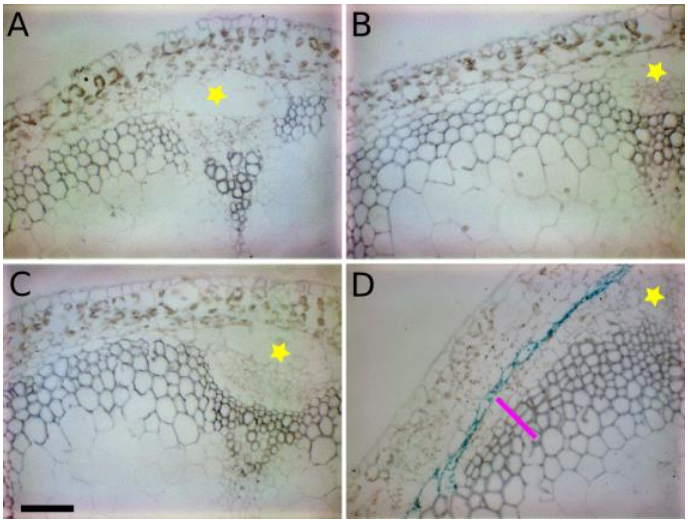

Figure 10 ***GUS staining of cross sections of the second internode is restricted to the starch sheath cells in the transgenic pSCR>>iaaM line upon ethanol treatment.*** *GUS staining of wild type (A), wild type ethanol treated (C), pSCR:AlcR, pAlcA:iaaM, pAlcA:GUS control (B) and pSCR:AlcR, pAlcA:iaaM, pAlcA:GUS ethanol treated (D), only D shows the blue GUS staining, which is restricted to the starch sheath cells; the successful GUS staining is a proof for a functional inducible system, vascular bundles are indicated with a yellow star and cell files are highlighted with a purple line.*

3.1.2. *De novo* formed cells in the interfascicular region have cambium identity

Real time quantitative PCR of markers for cambium identity

To elucidate the effect of local auxin biosynthesis with regard to stem cell activity I performed real-time quantitative PCR and compared the expression levels of *WUSCHEL RELATED HOMEOBOX 4* (*WOX4*) and *PHLOEM INTERCALATED WITH XYLEM* (*PXY*) in samples of the second internode. *WOX4* and *PXY* are promoting cambium activity and their expression suggested the cambium identity, as well as their increase in expression suggested a rise in cambium activity.

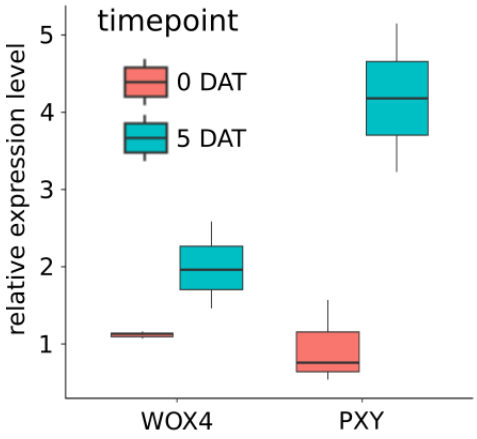

Figure 11 ***qRT-PCR analysis of WOX4 and PXY expression in the second internode of the stem in pSCR:AlcR, AlcA:iaaM*** *before (pink) and 5 days after ethanol treatment (turquoise) in comparison to wild type revealed increased expression level of WOX4 and PXY 5 DAT. ACT2 was used as housekeeping gene and showed the same behavior as the comparison against UBQ10. Relative expression level is calculated against the expression in wild type for 0 DAT and control group of transgenic plants for 5 DAT. Statistical significant difference of dCT values of WOX4 is revealed by pairwise comparison using t-test with pooled SD with n = 3, p < 0.01.*

Both cambium marker genes show an increased expression level when compared to the control group of transgenic plant (5 DAT) (Figure 11). This is particular interesting because at this time point only 16 % of the samples showed cell files to some extend (Figure 9). It suggests that the *de-novo* formation of cambium cells in the interfascicular region starts already 5 DAT even though phenotypical differences are less obvious at that time point. As the real-time quantitative PCR does not allow any conclusion on the localisation of events of upregulation of quantified genes, I performed a cambium marker analysis as well with YELLOW FLUORESCENT PROTEIN (YFP) expressed under the cambium specific pWOX4 and pPXY.

Analysis of cambium markers revealed cambium identity of de novo formed cells in the interfascicular region

To determine the identity of the de-novo formed cells in the interfascicular region, I crossed the transgenic line expressing *iaaM* in an ethanol inducible manner with transgenic lines expressing an endoplasmic reticulum (ER)-localized YELLOW FLUORESCENT PROTEIN (YFP) under the control of *PXY* (Figure 12; A and C) or the *WOX4* (Figure 12, B and D) promoters. Samples were harvested 10 DAT and cross sections were counterstained with propidium iodide. In control situation transgenic plants the fluorescent signals of both

cambium markers were restricted to the vascular bundles, no fluorescent signal was observed in the interfascicular region (Figure 12, A and B). In cross sections of the ethanol treated transgenic plant allowing induction of iaaM, cell files were formed (Figure 12, C and D) and showed fluorescent signals of both the *PXY* (Figure 12, C) and the *WOX4* (Figure 12, D) reporters. Therefore, I concluded that local induction of *iaaM* in starch sheath cells is sufficient to initiate the *de-novo* formation of interfascicular cell files with cambium identity 10 DAT.

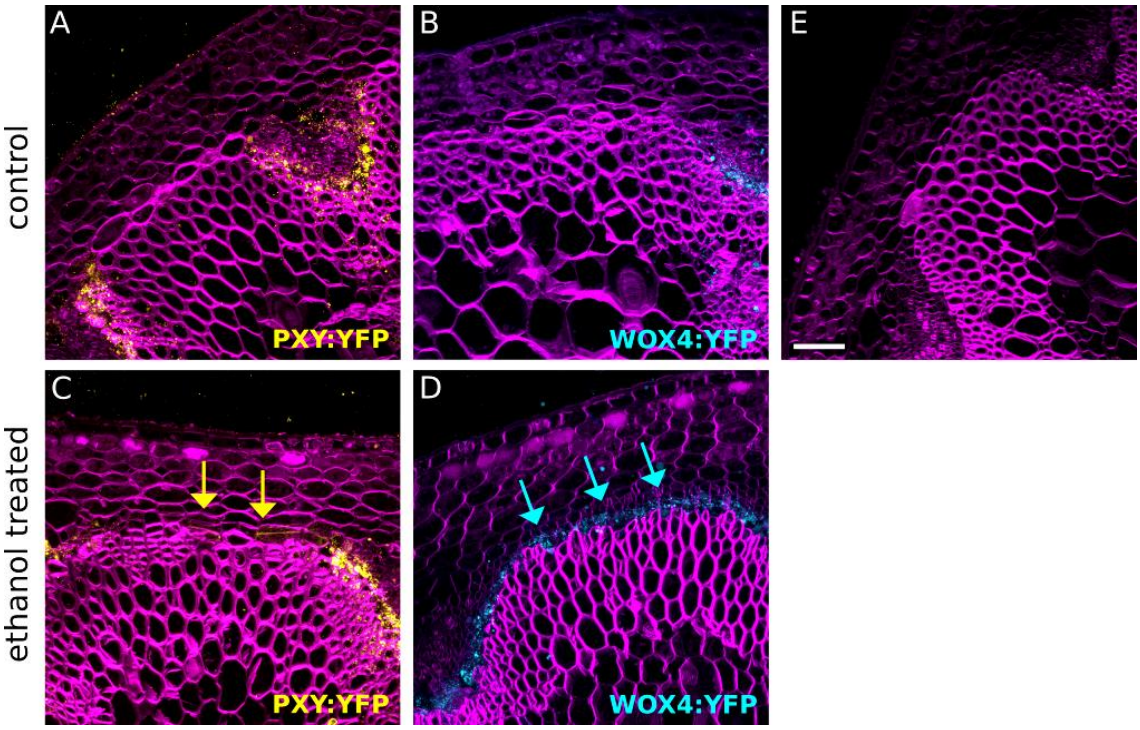

Figure 12 ***De-novo formed cell files in the interfascicular region have cambium identity****; cross sections of the second internode of F1 generation pSCR:AlcR, pAlcA:iaaM crossed with pPXY:YFP or pWOX4:YFP, cross sections were counterstained with propidium iodide, scale bare equals 50 µm; pSCR:AlcR, pAlcA:iaaM, pPXY:YFP control (A), pSCR:AlcR, pAlcA:iaaM, pPXY:YFP ethanol treated, 10 DAT (C), pSCR:AlcR, pAlcA:iaaM, pWOX4:YFP control (B) and pSCR:AlcR, pAlcA:iaaM, pWOX4:YFP ethanol treated 10 DAT, negative control for YFP (E); de-novo formed cells in the interfascicular region are only present in cross sections of the ethanol treated plants, they show pPXY:YFP (yellow arrow) and pWOX4:YFP (turquoise arrow) positive cells indicating their cambial indentity (C, D); in cross sections of the control plants YFP signal is restricted to the vascular bundles (A, B).*

3.2. Nuclear auxin signaling is important for interfascicular cambium formation

3.2.1. Real time quantitative PCR revealed a maximum of IAAM expression 1 DAT

As this study relies on increased auxin biosynthesis upon ethanol induction by expressing the bacterial auxin biosynthesis gene *iaaM* it was necessary to study the expression profile of *iaaM* after ethanol treatment. To investigate the dynamics of the expression of the bacterial Trp-2-monooxygenase *iaaM* expression in the second internode of the stem in pSCR:AlcR, pAlcA:iaaM plant after ethanol treatment, I performed real-time quantitative PCR of *iaaM*. To achieve a resolution in time, samples where collected 0.5, 1, 2 and 5 DAT. As *iaaM* is of bacterial origin and is not expressed in planta, expression was not compared with the wild type situation rather than expression of *iaaM* in plants carrying pSCR:AlcR, pAlcA:iaaM harvested before induction with ethanol. From an earlier study of the ethanol inducible system it is known, that gene expression peaks 5 DAT (Ulmasov et al., 1997). Unexpectedly the expression level of *iaaM* was already high 0.5 DAT and peaked 1 DAT. The expression level of *iaaM* dropped significantly at 5 DAT (Figure 13). This shows the necessity to check expression after an induction because the dynamics and strength of the induction is dependent on the way of application and the tissue of action and so in its interaction very individual. Here, it can be concluded, that the induction of *iaaM* is working and the expression of *iaaM* shows a high dynamic within the first 5 days after its induction.

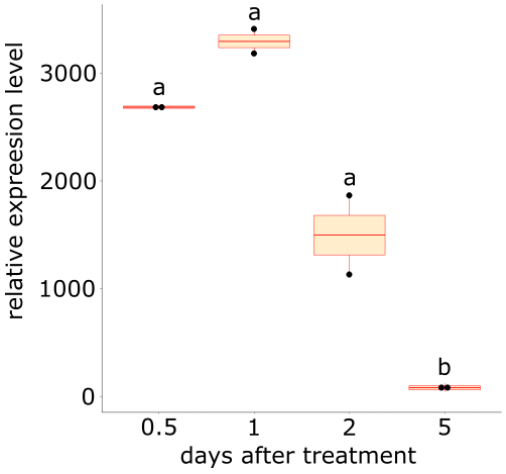

Figure 13 ***qRT-PCR analysis of iaaM expression in the second internode of the stem in pSCR:AlcR, AlcA:iaaM plants in a time-resolved manner*** *showed high expression*

level already 0.5 DAT and a significant lower expression 5 DAT. ACT2 was used as housekeeping gene and showed the same behavior as the comparison against UBQ10. Relative expression level was calculated against the expression in pSCR:AlcR, AlcA:iaaM at 0 DAT. Statistical significant difference of dCT values is revealed by ANOVA.

3.2.2. Blocking of nuclear auxin signaling has a negative effect on IC formation

To address the question whether nuclear signaling is the predominant route by which auxin induces IC formation, I blocked nuclear auxin signaling by expression of the mutated AUX/IAA protein *bodenlos* (*bdl*) which does not respond to auxin and can repress the transcriptional influence of auxin (Hamann et al., 2002) in starch sheath cells. In that way, auxin could still have a non-nuclear effect while specifically nuclear auxin signaling was inhibited.

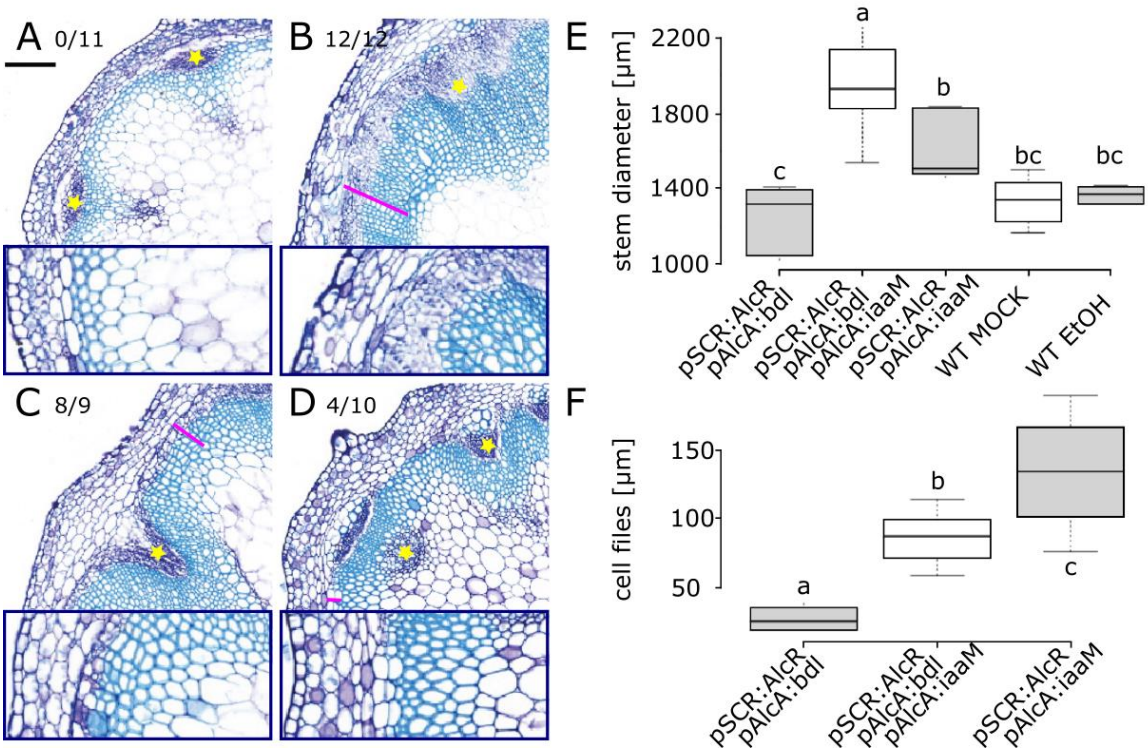

Figure 14 ***Cell files in the interfascicular regions are induced upon ethanol treatment of pSCR:AlcR, pAlcA:iaaM even if nuclear auxin signaling is reduced through the parallel expression of bodenlos (bdl)****, toluidine blue staining of cross sections of the second internode, interfascicular region with vascular bundles highlighted with a yellow asterix de-novo formed cell files are indicated with a purple line; wild type control (A), pSCR:AlcR, pAlcA:iaaM ethanol treated (B), pSCR:AlcR, pAlcA:iaaM, pAlcA:bdl ethanol treated (C) and pSCR:AlcR, pAlcA:bdl ethanol treated (D); cell file formation is visible in all transgenic plants with altered auxin signaling in the starch sheath cells; the analysis of the cross sections revealed that under the influence of iaaM the stem diameter is increased no matter whether bdl is expressed in parallel or not. The expression of bdl under pSCR has even a positive effect on the stem diameter. The lower diagram (F) shows the length of cell files in cross sections of the different genotypes, and shows a significant reduction of cell file length if bdl is expressed in parallel to iaaM, statistical significant difference is revealed by ANOVA.*

I performed a histological analysis on the second internode of wild type plants and plants that express either exclusively *iaaM* or *bdl*, or *iaaM* and *bdl* simultaneously upon ethanol induction in starch sheath cells. I harvested samples for the analysis 10 DAT and stained the cross sections with toluidine blue. While wild type plants did not show the formation of cell files (Figure 14, A) the positive control pSCR:AlcR, pAlcA:iaaM did show in 100 % of the samples cell files (Figure 14, B, F) as well as an increased stem diameter (Figure 14, E). In cross sections of plants that expressed *bdl* in parallel to *iaaM*, cell file formation was significantly decreased compared to plants that only expressed *iaaM*, but was still visible (Figure 14, C, F). Interestingly also plants with expression of *bdl* alone showed cell files in 40 % of the cross sections (Figure 14, D).

From these results I concluded that local nuclear auxin signaling is involved in the process of IC formation and blocking of nuclear auxin signaling influences this process.

3.2.3. Localization of auxin signaling by DR5 marker analysis

After having checked the functionality of the induction system I was interested in the localization and the distribution of auxin signaling. Is a change in auxin signaling only observed in the starch sheath cells or could it potentially act in a non cell-autonomous? To visualize auxin signaling I used a reporter system with the DR5-rev promoter that drives the expression of ER-localized GREEN FLUORESCENT PROTEIN (GFP) (Hanson and Köhler, 2001). I crossed the stable marker line with the ethanol-inducible transgenic line to induce auxin biosynthesis in the starch sheath. I harvested samples of the second internode of the F1 generation 3 DAT and 5 DAT to keep track of the dynamics of auxin signaling by DR5 fluorescent signal intensity and localisation. Samples were counterstained with DirectRed23 to visualize cell walls.

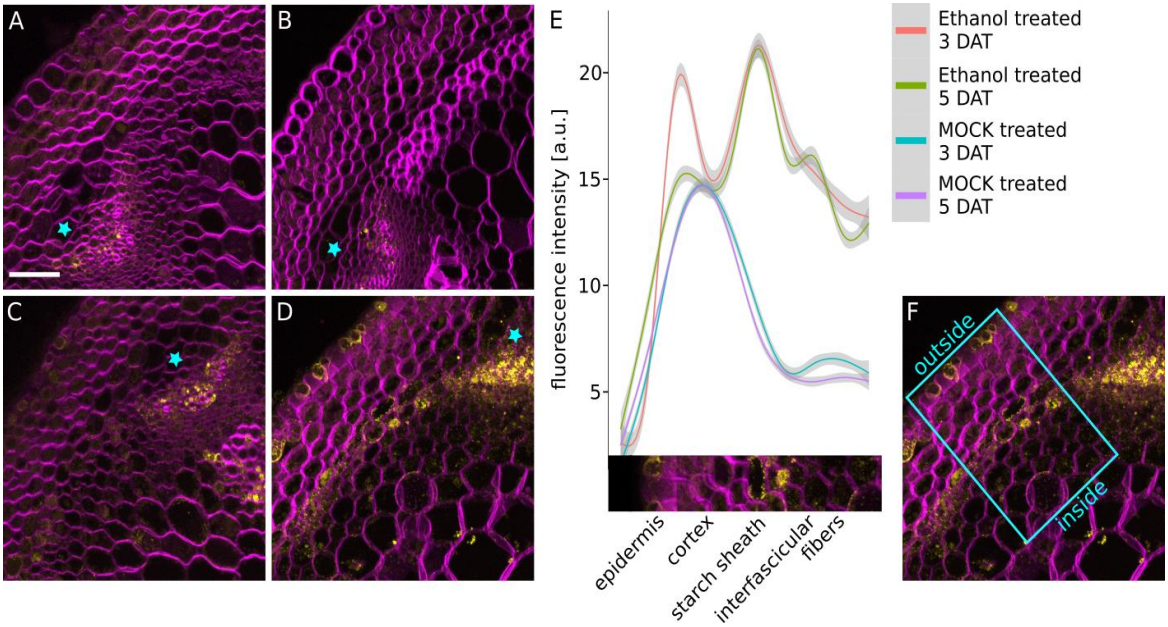

Figure 15 ***Investigation of the dynamics of auxin signaling in pSCR:AlcR, AlcA:iaaM after ethanol treatment.*** *Fluorescence confocal microscopy of DR5:GFP in pSCR:AlcR, AlcA:iaaM three and five days after treatment (DAT), counterstained with DirectRed 23; control, 3 DAT (A) ethanol treated, 3 DAT (C), control, 5 DAT (B) ethanol treated, 5 DAT (D), vascular bundles are highlighted with turquoise stars, increased GFP fluorescence signal is visible in the interfascicular region 5 DAT (D), the distribution of the GFP fluorescence signal was analysed in the interfascicular region €, cross sections of the ethanol treated plants show increased fluorescence intensity at the position of starch sheath cells even though the signal was broadly distributed.*

In the negative control transgenic plants the fluorescent signal from the pDR5rev:GFP reporter system was restricted to the vascular bundles and low in intensity (Figure 15, A and B). There was no difference in signal distribution or in intensity comparing the different time points. Ethanol treated transgenic plants showed a clearly increased fluorescence intensity in the vascular bundles and a supplementary fluorescent signal in the interfascicular region, with its maximum in starch sheath cells (Figure 15, C and D). All samples showed an increased signal intensity in the cortex region of the cross section. I analyzed the fluorescence signal, its distribution and the intensity profile (Figure 15, E). The fluorescent signal in starch sheath cells was 70 % increased compared to the control situation at both time points. Signal intensity was not at control levels at neighboring areas towards the inside of starch sheath cells. For the cortex the signal intensity dropped on signal intensity levels of the control situation at 5 DAT. This indicates a spread of auxin signaling towards xylem tissue in the cross section.

Furthermore, I investigated pDR5rev:GFP fluorescent signals in plants that did not only express *iaaM* upon ethanol induction but *iaaM* and *bdl*

in parallel at 5 DAT. By this way I tested whether the expression of *bdl* can completely supress nuclear auxin signaling.

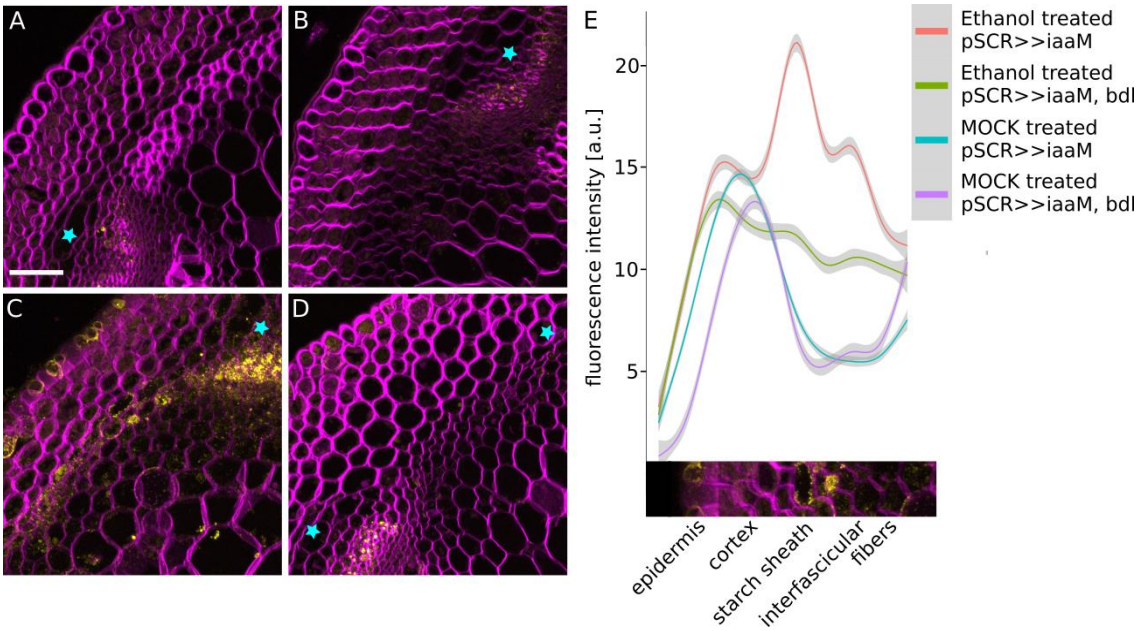

Figure 16 ***Blocking of nuclear auxin signaling though expression of bodenlos (bdl) in parallel to iaaM.*** *Fluorescence confocal microscopy of DR5rev:GFP in pSCR:AlcR, AlcA:iaaM and pSCR:AlcR, AlcA:iaaM, AlcA:bdl, 5DAT, counterstained with DirectRed23; pSCR:AlcR, AlcA:iaaM, control (A) pSCR:AlcR, AlcA:iaaM, ethanol treated (C), pSCR:AlcR, AlcA:iaaM, AlcA:bdl, control (B) pSCR:AlcR, AlcA:iaaM, AlcA:bdl, ethanol treated (D), decreased fluorescent signal intensity of DR5rev:GFP if bdl is expressed simoultaniously with iaam in the starch sheath (E).*

In control plants the fluorescent signal was again restricted to the vascular bundles and was very weak compared to the fluorescent signal in induced transgenic plants with increase auxin biosynthesis (Figure 16, A and B). In cross sections of transgenic plants expressing *iaaM* the fluorescent signal was clearly increased in starch sheath cells but also in cortex cells (Figure 16, C). In comparison to this, transgenic plants expressing *iaaM* and *bdl* simultaneously showed decreased fluorescent signal in starch sheath cells (Figure 16, D) down to 50 % of the signal intensity of the plant expressing *iaaM*. Signal intensity was still around 25 % higher compared to the control situation (Figure 16, E). Those findings confirmed that bdl repressed auxin signaling but did not inhibit it completely.

3.3. Acidification of the cell wall has no effect on IC formation

3.3.1. Real time quantitative PCR revealed a maximum of SAUR19 expression 1 DAT

As it is known that auxin can cause cell wall acidification possibly by SAUR19 expression and subsequent activation of the H+ATPase, this is a possible junction of auxin and the cell wall (Rayle and Cleland, 1992; Spartz et al., 2014; Takahashi et al., 2012). I analyzed the expression profile of SAUR19 via real-time quantitative PCR. Its expression is mediated by the TIR1/AFB receptor and it inhibits the enzymatic activity of a certain subset of type 2C protein phosphatases that dephosphorylate the AHA protein and lower its proton pump activity (Fendrych et al., 2016; Takahashi et al., 2012). In reverse an increase of *SAUR19* expression could lead to a higher proton pump activity.

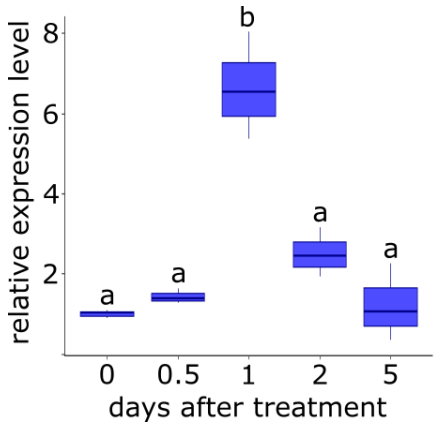

Figure 17 ***qRT-PCR analysis of SAUR19 expression in the second internode of the stem in pSCR:AlcR, AlcA:iaaM*** *in a time resolved manner in comparison to wild type and control group of transgenic plants revealed increased expression level of SAUR19 1 DAT, statistical significant difference of dCT values is revealed by ANOVA with n = 3.*

For the analysis I harvested the second internode of the control and ethanol treated wild type and transgenic plants expressing *iaaM* in an ethanol dependent manner before and at several time points after the treatment (0, 0.5, 1, 2 and 5 DAT). For the analysis 0 DAT I compared *SAUR19* expression to the wild type plants in all other cases I used the comparison of *SAUR19* expression to the control group of transgenic plants. The analysis of the results revealed a significant increase of *SAUR19* expression 1 DAT. After this, expression of *SAUR19* dropped down again to the level of 0 DAT (Figure 17). This suggests an auxin induced higher proton pump activity already after 1 DAT mediated by *SAUR19*. A higher proton pump activity acidifies the cell wall as a possibly very early event after increase of auxin biosynthesis. As *iaaM*

dropped after 1 DAT, auxin biosynthesis decline and expression of auxin downstream targets decrease as well.

3.3.2. Acidification of the cell wall follows increased auxin biosynthesis

Auxin induced acidification of the cell wall mediated by *SAUR19* expression and activation of the proton pump could be a very early auxin induced event in IC formation. *SAUR19* was found to be upregulated 1 DAT in plants with increased auxin biosynthesis in the starch sheath. So the next step was to determine the pH of the cell wall as consequence of enhanced auxin biosynthesis. To measure the acidification of the cell wall of starch sheath cells upon enhanced auxin biosynthesis I made use of a pH sensitive, cell wall anchored, ratiometric pUB10::SYP122-eGFP-mRFP (Kesten et al., 2019). This pH marker combines enhanced GREEN FLUORESCENT PROTEIN (eGFP) fused to monomeric RED FLUORESCENT PROTEIN (mRFP) which is fused to the C-terminus of plasma membrane localized SNARE protein Syntaxis of Plants 122 (SYP122) and expressed under the control of the ubiquitously active UBIQUITIN 10 promoter. This makes it possible that the eGFP protrude into the apoplast. While the eGFP reacts to increased proton concentration in the apoplast with a decrease in fluorescence intensity, mRFP does not react and its fluorescent intensity stays stable in presence of protons. The ratio of both signals can be taken to calculate the pH after calibration.

Since the starch sheath in the stem is not accessible via fluorescence microscopy without cutting the stem which would influence cell wall integrity and impact cell wall pH, I started by measuring the apoplastic pH in roots of transgenic lines expressing *iaaM* under starch sheath specific promotor. This is possible, because the SCR promotor is active in both organs, the stem and the root. So I can use the root to see, whether there is a change in apoplastic pH after ethanol induced *iaaM* expression in the SCR domain. I made use of the pH sensitive, ratiometric pUB10::SYP122-eGFP-mRFP described above and crossed it to the transgenic line with enhanced auxin biosynthesis in the SCR domain. To visualize the *SCR* expression domain in the root, I used a marker line expressing YFP under the starch sheath specific *SCR* promoter. In roots of 5 DAG old seedlings YFP fluorescent signal could

be detected in the endodermis of the elongation zone (Figure 18, B). Calibration of the pUB10::SYP122-eGFP-mRFP line was carried out with roots of 5 DAG seedlings on ½ MS plates grown in long day condition. The seedlings were immersed in buffer solutions of different pH values for 10 minutes before imaging. Fluorescent signal of mRFP was used to define a mask (ROI – region of interest) (Figure 18, A). I used the mask to quantify the fluorescent intensity of mRFP (Figure 18, A´) and eGFP (Figure 18, A´´). The ratio of both was plotted against the pH of the buffer solution and revealed a sigmoidal correlation between pH and eGFP/RFP ratio of the sensor with a linear range between 5.2 and 6.8 (Figure 18, C).

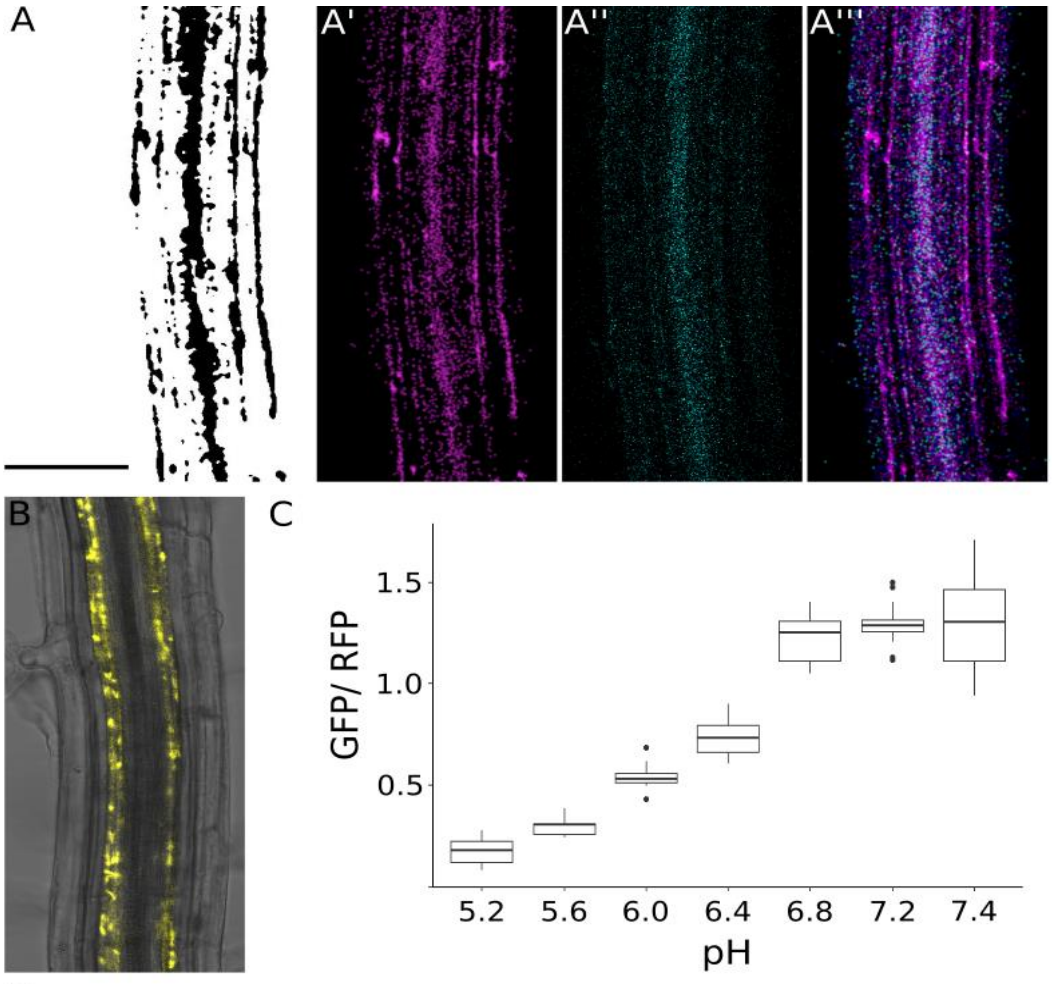

D

	GFP/RFP	pH
WT	0.283 ± 0.079	5.6
pSCR>>iaaM MOCK treated	0.312 ± 0.061	5.7
pSCR>>iaaM EtOH treated	0.132 ± 0.023	out of calibration range
pSCR>>AHAΔ94 EtOH treated	0.153 ± 0.035	out of calibration range

Figure 18 ***Quantification of acidification of the apoplast with pH_{apo} sensor SYP122-pHusion in the root.*** *Roots were imaged with fluorescence confocal microscopy and fluorescence signal of eGFP and mRFP was quantified with FIJI; a ROI was created (A) and used to analyze fluorescence signal of eGFP (A') and mRFP (A'') an overlay of both channels is shown in (A'''), to visualize the localization of the pSCR in the root a root of a transgenic line carrying pSCR:YFP was imaged (B), calibration row was carried out with roots of 5 DAG seedlings on ½ MS plates grown in long day condition, seedling were immersed in buffer solutions of different pH values for 10 minutes before imaging (N=12), fluorescent signal was quantified (C), pH of the apoplast in wild type and transgenic lines was quantified the very same way (D).*

Furthermore, I introgressed the pUB10::SYP122-eGFP-mRFP sensor into my pSCR:AlcR, pAlcA:iaaM line and induced the seedlings on plates with some drops of 70 % ethanol. For the treatment of the control group I dropped an equal amount of water on the plates. Twelve hours after the treatment, I imaged the mRFP and eGFP fluorescent signal of the seedlings and calculated the ratio (Figure 18, D). The seedlings of the control group showed a mRFP-eGFP ratio comparable with the result obtained in wild type seedlings. Seedlings that were ethanol treated showed a significant lower ratio due to quenched eGFP fluorescence. EGFP was indeed quenched so strongly, that the eGFP-mRFP ratio lied outside of the calibration range. This clearly showed that ethanol induced expression of *iaaM* under the control of the SCR promoter was sufficient to acidify cell walls within 12 hours in roots and, potentially, in stems. I analyzed the eGFP/RFP ratio in all cell walls and did not exclusively analyzed the signal in the endodermis (SCR domain), so I can not conclude about the localization of the acidification of the cell wall.

3.3.3. Histological study revealed small effect of cell wall acidification on interfascicular cambium formation

Beside the formation of IC, one effect of increased auxin biosynthesis is the acidification of the cell wall as determined in Figure 18, D. To figure out, whether cell wall acidification is sufficient for IC formation, I generated a transgenic plant line with an ethanol inducible H^+-ATPase (*AHA∆94*) that is constitutively active in the starch sheath upon initial ethanol induction. The hyperactivity of the proton pump resulted from the 94 aminoacid deletion from the protein, which removes of the autoinhibitory domain of the proton pump, which is therefor not responsive to any regulatory inputs (Axelsen et al., 1999). I performed histology analysis of toluidine blue stained cross sections of the second

internode of wild type plants and transgenic plants expressing *iaaM* or *AHA∆94* upon ethanol induction.

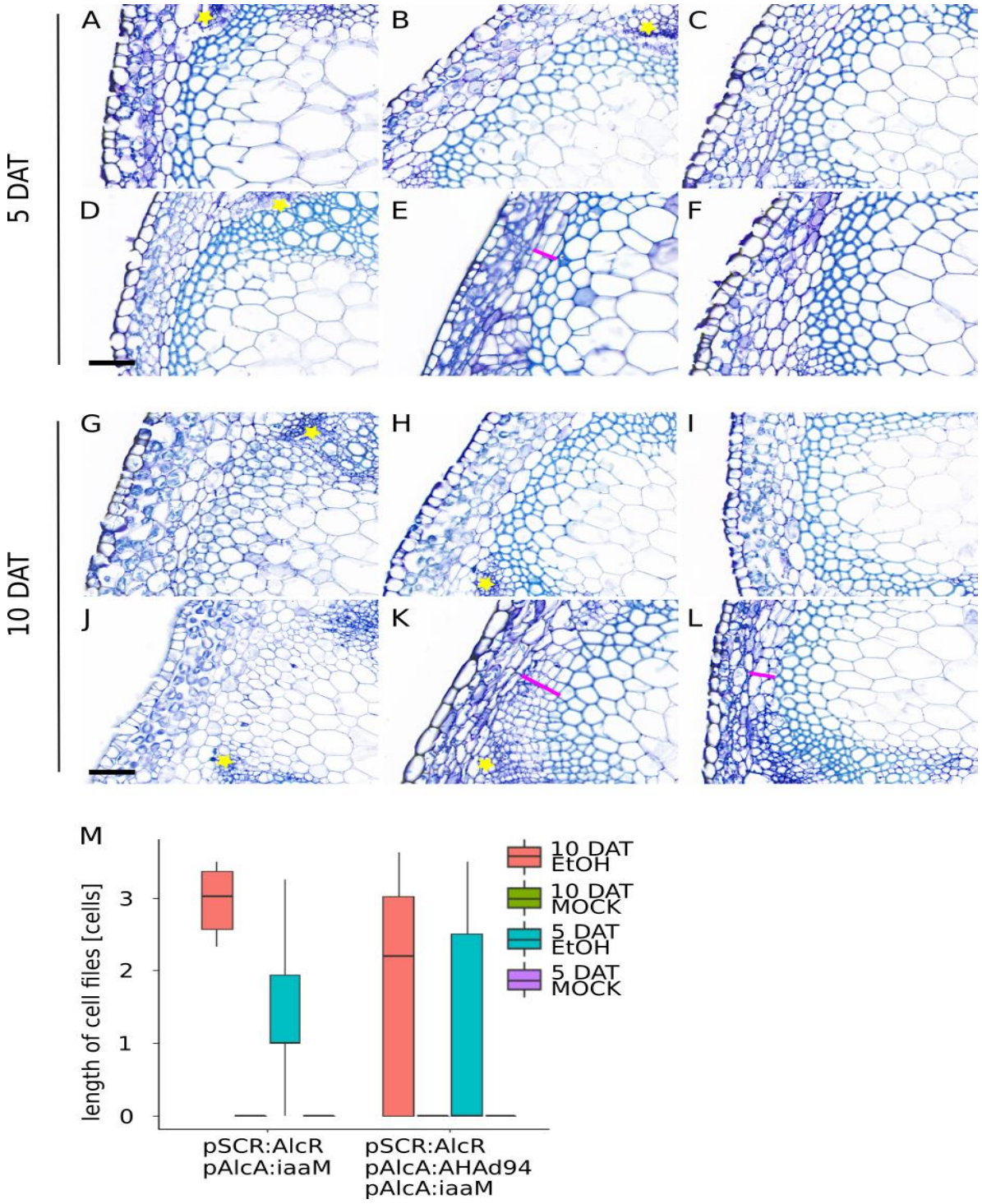

Figure 19 ***Cell files in the interfascicular regions are induced upon ethanol treatment of pSCR:AlcR, pAlcA:iaaM transgenic plants induction of AHA⊿94 in pSCR:AlcR, pAlcA:AHA⊿94 is not sufficient to trigger cell file formation****, additional effects can not be observed in a transgenic line expressing pSCR:AlcR, pAlcA:iaaM, pAlcA:AHA⊿94 , cross sections of the second internode 10 DAT, interfascicular region with vascular bundles highlighted with a yellow star; upper panel: toluidine blue staining of wild type control (A), pSCR:AlcR, pAlcA:iaaM control (B) and pSCR:AlcR, pAlcA:AHA⊿94 control (C) wild type ethanol treated (D), pSCR:AlcR, pAlcA:iaaM ethanol treated (E) and pSCR:AlcR, pAlcA:AHA⊿94 ethanol treated (F), only in (E) cell files are formed in the interfascicular region, highlighted with a purple line; lower panel: toluidine blue staining of wild type control (G), pSCR:AlcR, pAlcA:iaaM control (H) and pSCR:AlcR, pAlcA:iaaM, pAlcA:AHA⊿94 control (I) wild type ethanol treated (J), pSCR:AlcR, pAlcA:iaaM ethanol treated (K) and pSCR:AlcR, pAlcA:iaaM, pAlcA:AHA⊿94 ethanol treated (L).*

Control plants show in none of the cases cell file formation in the interfascicular region. Ethanol treated transgenic plants with *iaaM* expression show cell file formation and are taken as positive control for a successful induction. In cross sections of the transgenic line, expressing *AHA⊿94* upon ethanol induction no cell file formation was observed. I crossed the line to the pH sensitive pUB10::SYP122-eGFP-mRFP and measured the pH of the cell wall in the same way as described earlier. A decrease of eGFP fluorescence intensity was observed (Figure 18, D) confirming cell wall acidification due to *AHA⊿94* expression. From this experimental outcome I concluded that acidification of the cell wall in starch sheath cells is not sufficient to induce cell file formation in the interfascicular region.

To test if acidification of the cell wall plays any role in the process of IC formation I performed a histological analysis of a line that expresses *AHA⊿94* parallel to *iaaM* in the starch sheath cells in an ethanol inducible manner. Using this approach, I tested for additive effects of additional acidification due to constitutive H^+-ATPase activity. The samples were harvested at two different time points. 10 DAT, because I knew that there were IC in the second internode in the transgenic line at this time point, and so I could analyze whether more or bigger cell files were formed. Additionally, I analysed plants 5 DAT, because I knew that *de novo* IC formation is a rare event in the transgenic line with enhanced auxin biosynthesis and I can control whether additional acidification lead to earlier IC formation (Figure 19, A – F). Cross sections of wild type plants, from the control group and ethanol treated (Figure 19, A + D) did not show IC formation and are taken as negative control. Samples from the negative control of the transgenic line showed no cell files in the

control samples (Figure 19, B + C), whereas in ethanol treated samples IC formation was observed not only 10 DAT (10/10 samples) (Figure 19, K) but also in one sample at 5 DAT (1/7 samples) (Figure 19, E). Samples from the plant line expressing *iaaM* in parallel to *AHA⊿94* show cell file formation upon ethanol treatment. More than 50 % of the samples (4/7 samples) (Figure 19, F) harvested 5 DAT and 85 % of the samples (6/7 samples) (Figure 19, L) harvested 10 DAT showed cell files in the interfascicular region. The length of the cell files was very different among and within samples and not significantly different between genotypes (Figure 19, M). The experimental outcome indicated that there is a slightly positive effect of additional acidification of the cell wall by expressing *AHA⊿94* in parallel to *iaaM*. Yet, further experiments are required to confirm this observation.

3.4. Cell wall modifications during interfascicular cambium formation

When comparing treated transgenic lines expressing iaaM in starch sheath cells with the ethanol treated wild type plants I discovered that genes encoded for cell wall remodeling enzymes are differentially expressed in the RNA sequencing suggesting that cell wall was potentially remodeled during or before IC formation. Therefore, I investigated changes of the cell wall composition using immunohistochemistry. I concentrated on two different cell wall epitopes, extensins and pectin and its modifications. It is known that the enzymatic activity of PMEs depend highly on the pH (Denès et al., 2000) and it was hypothesized that cross linking of extensins with the pectin matrix is dependent on the pH (Durachko and Cosgrove, 2009; Schnabelrauch et al., 1996). Hence it would be interesting to detect modification of the cell wall that can be linked with cell wall acidification. Whether the cell wall modification that could be caused by cell wall acidification can be detected.

3.4.1. Immunohistochemistry revealed increased abundance of extensins in the interfascicular region

Extensins, which are known to build scaffolds in newly formed cell walls (Cannon et al., 2008), can be detected by the rat monoclonal antibody

JIM11 (Plant Probes) and can be visualized with a secondary fluorescent antibody, here Alexa Fluor 488 anti-rat. I used propidium iodide to counterstain the cell wall. To test the natural situation and abundance of extensins I performed immunohistochemistry with cross sections in wild type stems. I started to collect cross sections 1 cm above the base and collected samples every 0.2 cm going down to the base (Figure 20 E). Interestingly the fluorescent signal intensity was significantly higher at 1 cm (Figure 20, A) and 0.8 cm (Figure 20, B) compared to the base (Figure 20, D). While the fluorescent signal is very restricted and only observed close to starch sheath cells at 1 cm above the base, the fluorescence signal got more and more diffuse in cross sections that are harvested closer to the base (Figure 20, A – D, F). This suggested that cell wall remodeling took place during the natural process of IC formation in and around the starch sheath.

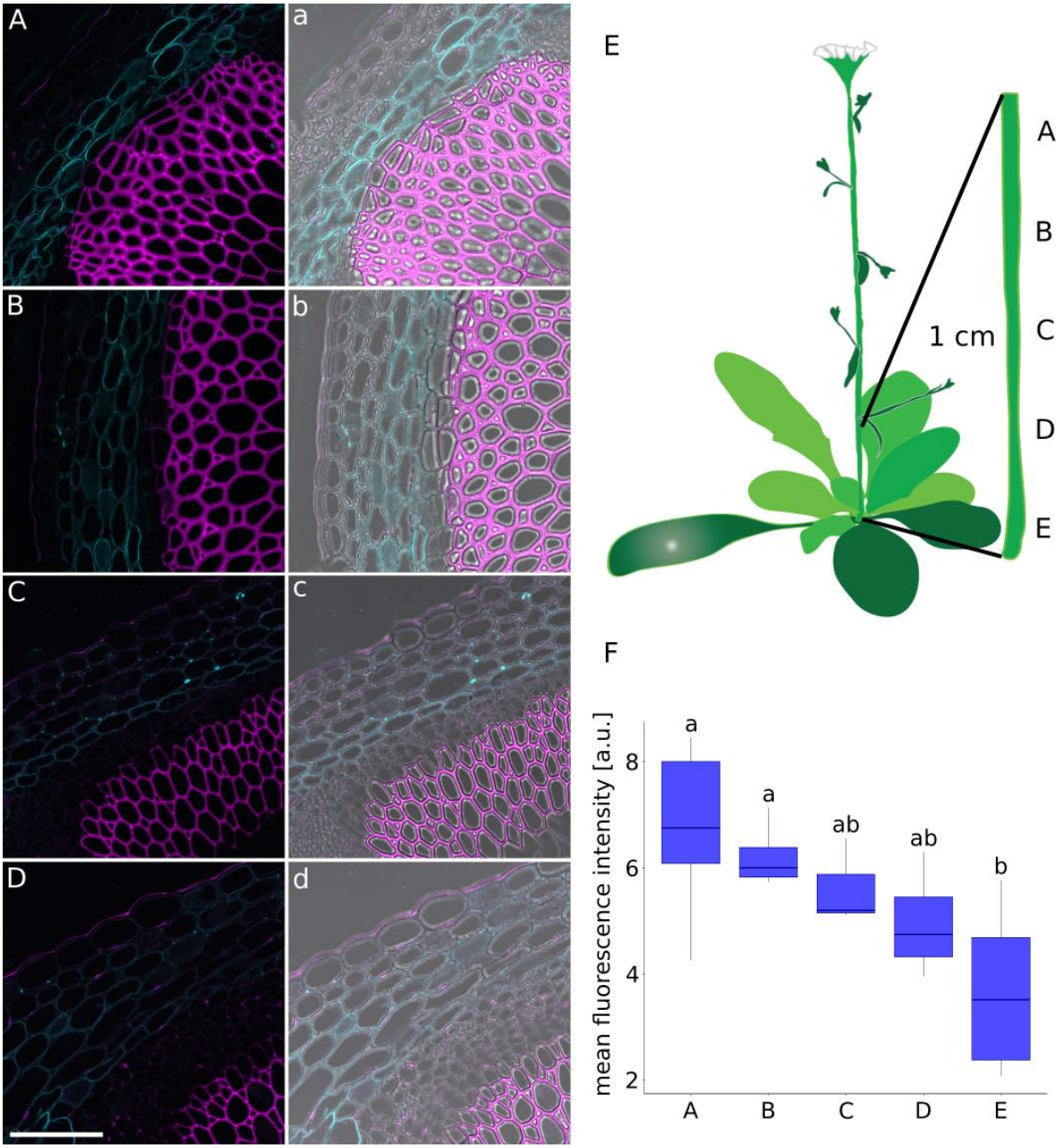

Figure 20 ***Immunohistochemistry of cross section of wild type with α-Extensin (JIM11) and PI counterstaining revealed the change in fluorescence intensity of the second antibody/ Alexa488 depending on the position (in relation to the base).*** *Cross sections show the interfascicular region of the stem 1 cm (A), 0.8 cm (B), 0.6 cm (C) and 0.4 cm (D) above the base stained with JIM11 without bright field (capital letters) and with bright field (small letters), the position of the cross sections can be estimated from the scheme (E). Fluorescence intensity was quantified and is the highest in the area where secondary growth starts to occur (1 cm above the base) and is getting lower the closer the sample was cut at the base (F). Statistically significant difference is revealed by ANOVA with n = 8.*

After investigating the abundance of extensins in the natural situation during IC formation at the stem base I use the same approach to test the abundance in transgenic plants, with increased auxin biosynthesis in the starch sheath, at cross sections of the second internode, where secondary growth can not be found under natural conditions. I harvested

samples 10 DAT let JIM11 cure in and used Alexa fluoro 488 anti-rat as a secondary antibody. In addition, I use propidium iodide to counterstain the cell walls. In wild type samples the fluorescent signal was restricted to starch sheath cells no matter whether plants were treated with ethanol or not (Figure 21, A + C). The fluorescent signal intensity of the ethanol treated transgenic line is significant increased compared to the wild type situation (Figure 21, E). Interestingly the fluorescent signal was also spread to the *de novo* formed cells in the interfascicular region (Figure 21, D). This indicates, that the cell wall of the newly formed cells in the interfascicular region contain more extensin in comparison to cell walls of other cell types, or that extensin is better accessible by the antibody in those cells.

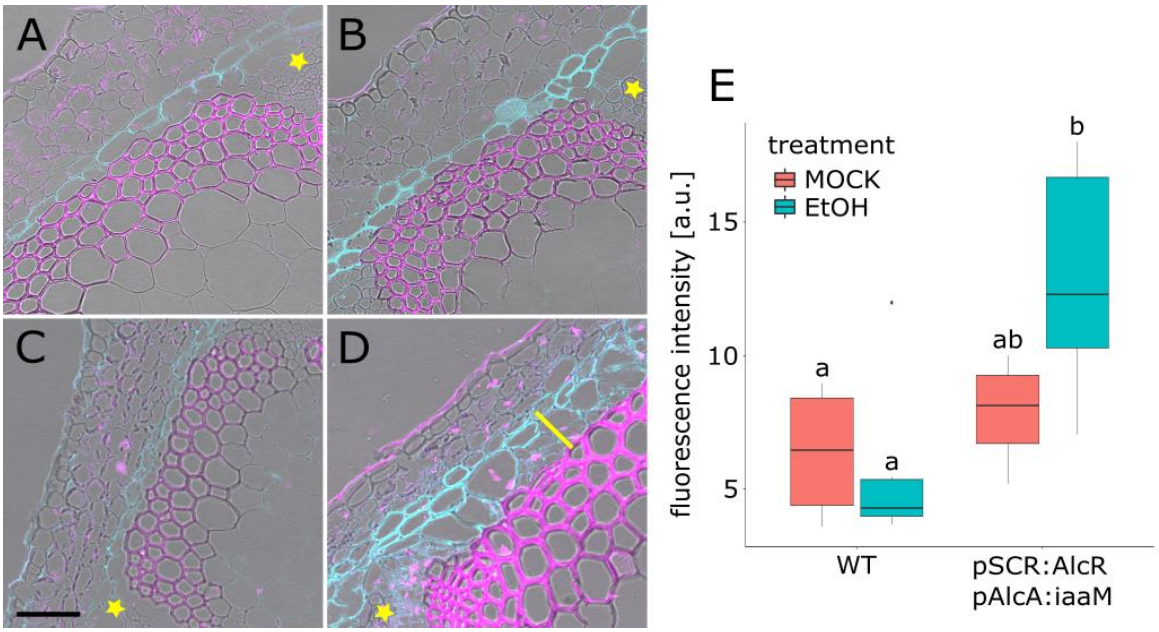

Figure 21 ***Immunohistochemistry of cross section of wild type and pSCR:AlcR, pAlcA:iaaM with α-Extensin (JIM11) and PI counterstaining revealed the change in fluorescence intensity of the second antibody/ Alexa488 depending on the expression of iaaM****. Cross sections show the interfascicular region (vascular bundles are marked with yellow stars) of second internode of wild type control (A), wild type ethanol treated (B), pSCR:AlcR, pAlcA:iaaM control (C) and pSCR:AlcR, pAlcA:iaaM ethanol treated (D) 10 DAT, fluorescence signal is restricted to starch sheath cells and was analyzed and plotted in a diagram (E), fluorescence intensity is the highest in the ethanol treated transgenic line, expressing iaaM that developed cell files (marked with yellow line, D) in the interfascicular region, statistical significant difference is revealed by ANOVA with n = 10.*

3.4.2. Immunohistochemistry revealed modification on the methyl esterification of pectins in starch sheath cells during interfascicular cambium formation

Pectin, which shows a high degree of methylesterfication when it is built in the cell wall, can undergo various modifications until its degradation during the aging of the cell wall (His et al., 2001; Peaucelle et al., 2011). To analyze the state of pectin modification I used again an immunohistological approach. I used two antibodies that are specific for certain pectin states. The monoclonal antibody LM20 which recognises the homogalacturonan domain of pectic polysaccharides and needs methyl-ester to bind (McCartney et al., 2000) and was recognized by the secondary antibody Alexa-Fluor 488. The monoclonal antibody 2F4 which binds specifically to a dimeric association of pectic chains through calcium ions (McCartney et al., 2000) and can be localized and quantified due to the fluorescent signal of the secondary antibody Alexa-Fluor 647. I performed the immunohistochemical staining on cross sections of the second internode of wild type plants from the control group and ethanol treated 10 DAT (Figure 22, A - C). The ethanol treated plants that express *iaaM* after ethanol induction in starch sheath cells show a binding of both pectin specific antibodies in the de novo formed cells in the interfasicular region (Figure 22, D). I measured the fluorescence intensity of both secondary antibodies in radial cell walls of starch sheath cells and calculated the ratio of both. The ratio of Alexa-Fluor 488 to Alexa-Fluor 647 is significantly decreased when *iaaM* is expressed in starch sheath cells upon ethanol induction (Figure 22, F). The decreased ratio of Alexa-Fluor 488 to Alexa-Fluor 647 could be explained by a decrease in binding possibilities for Alexa-Fluor 488 or an increased binding possibility for Alexa-Fluor 647. So that the decreased ratio could be an indication for less binding of LM20 at methyl esterified pectins or more binding of 2F4 of calcified de-methylated pectins. This allows the conclusion, that enhanced auxin biosynthesis in the starch sheath upon ethanol induction influenced pectin modification and had especially a positive effect on de-methyl esterification. The different accessibility of cell wall epitopes can still have an effect on the results but should be rather low, as two epitopes are directly compared to each other.

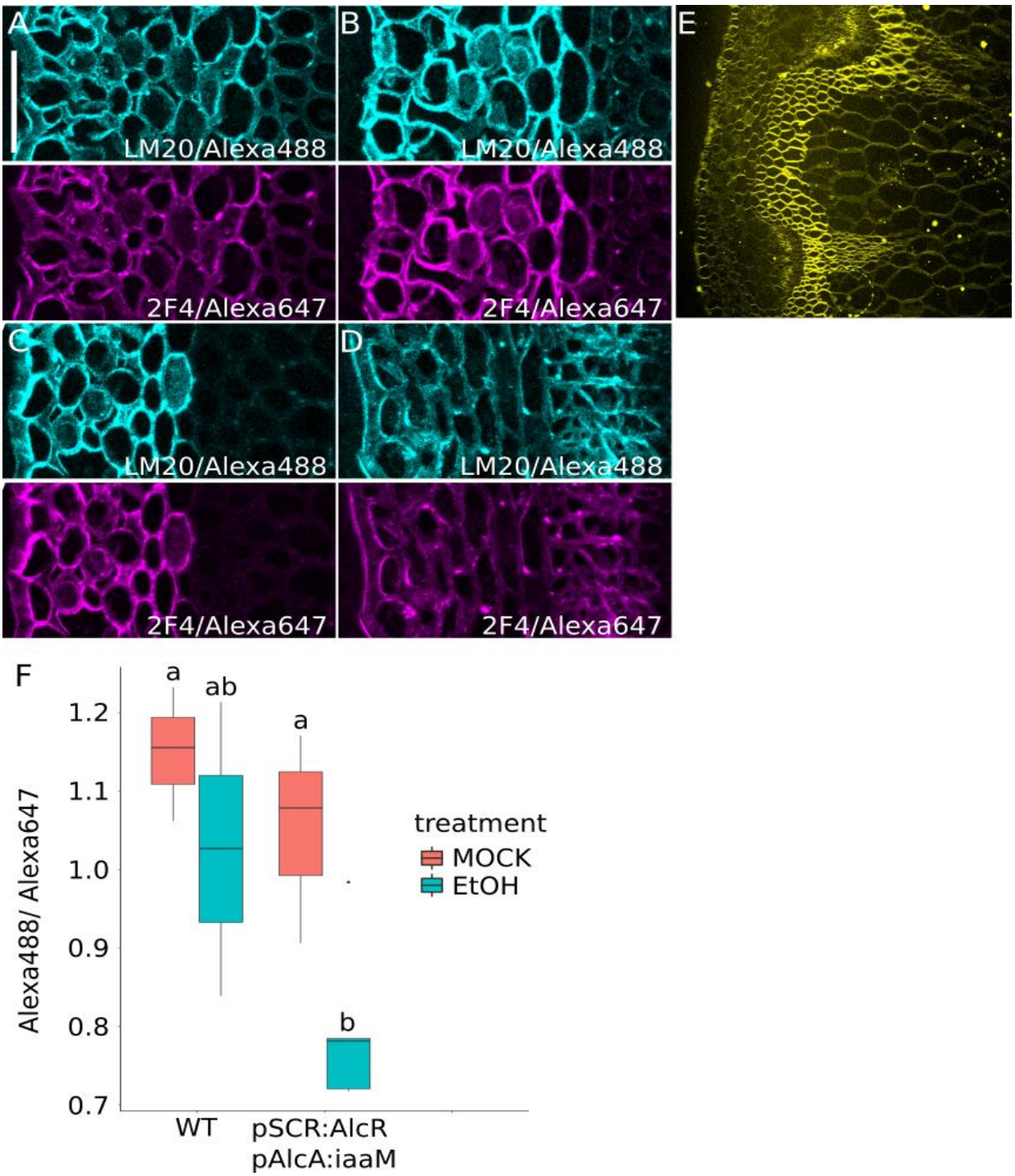

Figure 22 ***Immunohistochemistry of stem cross sections of the second internode 10 DAT with LM20 (antibody binding methyesterfied pectin) with Alexa488 as secondary antibody (turquoise) and 2F4 (antibody binding de-methylesterified calcified pectin) with Alexa647 as secondary antibody (violett) revealed a changed ratio of both in pSCR:AlcR, pAlcA:iaaM ethanol treated samples****. Cross sections show the interfascicular region of the second internode of wild type control (A), wild type ethanol treated (C), pSCR:AlcR, pAlcA:iaaM control (B) and pSCR:AlcR, pAlcA:iaaM ethanol treated (D), DR23 counterstained, negative control usage of the secondary antibody only (E), the ratio of the fluorescence intensity of the respective secondary antibody was analyzed and revealed a lower ratio of Alexa488 and Alexa647 in the ethanol treated transgenic line (F), statistically significant difference is revealed by ANOVA with n = 10.*

3.5. RNA sequencing and GO term analysis of differentially expressed genes upon interfascicular cambium initiation

As histological changes only appeared 10 DAT I performed genome-wide mRNA sequencing and analysed the results to figure out earlier events and differentially expressed genes that paved the way to the histological changes. As samples, exclusively second internodes of the stem were harvested 5 DAT to determine earlier auxin-induced events that are important for interfascicular cambium formation. Second internodes of three individual plants were pooled for one biological replicate. Library preparation and next-generation-sequencing was performed at CellNetworks Deep Sequencing Core Facility using HiSeqV4 (Illumina) with single-end 50-nucleotide reads. Reads were aligned to the A. thaliana Columbia (TAIR10) genome (Bolser et al., 2016) by Dongbo Shi. Ethanol-treated wild type samples were compared with samples from the ethanol-treated transgenic line, carrying the ethanol inducible construct *pSCR:AlcR, pAlcA:iaaM* with a statistical stringency of p-value < 0.01 (Wald Test). Applying these settings, 4400 genes were found to be differentially expressed comparing the transcriptome data of ethanol-treated wild type and ethanol-treated *iaaM* expressing plants (1884 genes upregulated, 2516 genes downregulated). After having classified 1 replicate as outlier, based on principle component analysis (Figure 23, A), a correlation analysis was performed and a high correlation coefficient among samples of the induced *pSCR>>iaaM* line and samples of the ethanol-treated wild type in the correlation plot (Figure 23, B) was found. To classify the differentially expressed genes I performed a gene ontology (GO) term enrichment analysis for “molecular function” (http://pantherdb.org/) and found nearly 800 genes in the dataset are annotated with “catalytic activity” (GO:0071554) which is nearly 20 % of all genes and by far the largest group (Figure 23, C). Afterwards, I classified those genes with the annotation “catalytic activity” after their occurrence in cellular components and identified GO terms that are over- or under-represented in the present set of genes. Surprisingly, genes annotated with the term “cell wall” (GO:0005618) are highly overrepresented with an enrichment of 5.5-fold over the expected number of genes (Fischer’s exact test). But also genes annotated with “extracellular region”

(GO:0005576) or “cytoskeleton” (GO:0005856) are over-represented (figure 23, D). This caught my attention and I performed a GO term analysis for the term “cell wall organization or biogenesis” (GO:0071554) on the whole data set and found 122 genes with this annotation being differentially expressed. For example, *PECTIN METHYLESTERASE 61* (*PME61*) is upregulated and is known to mediate de-methylesterification in primary cell walls (Wolf et al., 2009). Another upregulated cell wall-related gene is *EXPANSIN 20* (*EXP20*) which is known to causes loosening and extension of plant cell walls by disrupting non-covalent bonding between CMFs and matrix glucans (Marga et al., 2005). A third upregulated cell wall gene is *EXTENSIN 1* (*EXT1*) which belongs to cell-wall hydroxyproline-rich glycoproteins (Figure 23 E, last row). Extensins are known to cross link with each other and enforce cell wall strength (Cannon et al., 2008). Also 92 genes with the GO term “response to auxin” (GO:0009733) were found in the data set. Among those you can find *AUXIN RESPONSE FACTOR 4* (*ARF4*) which was found to act positively on cambium activity from outside of the stem cell region (Brackmann et al., 2018). Another auxin-associated gene that was found to be upregulated is *PIN-FORMED 3* (*PIN3*). PIN3 protein is localized at the plasma membrane preferentially in cells of the starch sheath and is necessary for lateral auxin transport (Friml et al., 2002). *SMALL AUXIN UPREGULATED 41* (*SAUR41*) was also upregulated compared to ethanol-treated wild type. *SAUR41* can not only be classified with the GO term “response to auxin” but it was also shown that it can cause acidification of the cell wall when it is overexpressed (Qiu et al., 2020) (Figure 23 E, first row). Furthermore, cambium-related genes like *WUSCHEL RELATED HOMEOBOX 4* (*WOX4*), *PHLOEM INTERCALATED WITH XYLEM* (*PXY*) and *SMAX1-LIKE 5* (*SMXL5*) are upregulated in samples of transgenic plants with enhanced auxin biosynthesis (Figure 23 E, middle row). Here it is important to mention that upregulation of cambium-related genes could be detected even before changes on the histological level got obvious. As those genes are expressed not only in the interfascicular cambium but also in the vascular cambium, it could be interpreted as enhanced expression of those genes in the vascular bundles. It is also possible that cambium-related genes are expressed in the interfascicular region even before

the very rough method of histology can reveal cambium activity in the interfascicular region in form of typical cell files.

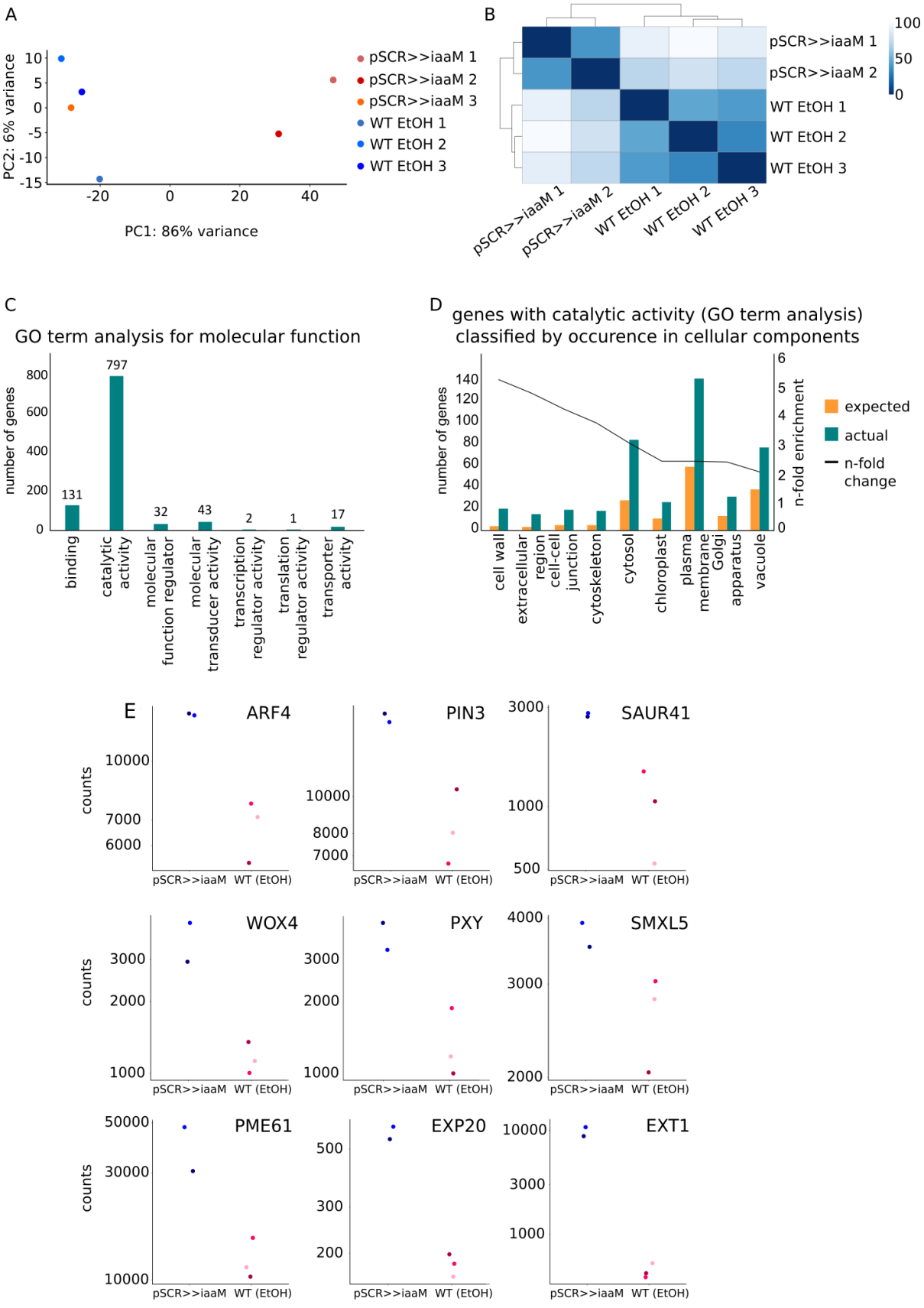

Figure 23 ***Analysis of the RNA sequencing dataset revealed a clear difference between the transcriptional profiles of the ethanol treated wild type and the ethanol treated transgenic line with enhanced auxin biosynthesis in starch sheath cells already 5 DAT.*** *The PCA analysis (A), the correlation plot displaying the statistical distance between each RNA-seq dataset according to the color code N = 2 or 3 (B), GO term analysis of the term "molecular function" on the whole data set (C), GO enrichment analysis by "cellular components" on all genes found annotated with "analytic function" (D), exemplary normalized gene read counts of the indicated genes in both groups of samples (E).*

To find that many cell wall related genes differentially expressed in the RNA sequencing data set upon induction of auxin biosynthesis was not completely surprising as it has been shown in other systems, that auxin can affect for example the degree of methyl esterification of pectin (Lehman and Sanguinet, 2019) or can affect cellulose deposition (Braybrook and Peaucelle, 2013). To investigate the impact of auxin on cell wall in more detail, I compared the obtained data set with RNA sequencing dataset from the rlp44 mutant in the stem (unpublished data). RLP44 is a receptor like kinase that is able to detect cell wall modifications and can react to is in a brassinosteroid hormone signaling depending manner (Wolf et al., 2014). It was found that RLP44 is required for the maintenance of cell fate in the root vasculature and it controls xylem differentiation (Holzwart et al., 2018). It also has been shown that RLP44 is present in the starch sheath cells (unpublished data), so that a regulating role of RLP44 is possible.

The RNA sequencing data set was obtained from samples of the stem in the second internode, that should still have the primary growth conformation. They were sequenced and alignment of the reads were performed as described before. Comparison was performed between the rlp44 mutant and the wild type, obtaining 5833 differentially expressed genes with a stringency of p-value < 0.01. I was particular interested in the potential secondary effect of RLP44 regulation on cell wall related genes. So I compared not only the two datasets but also the cell wall related genes in my data set as a subgroup (Figure 24, A). Interestingly 50 of 122 cell wall related genes were differentially expressed in both data sets and 72 cell wall related genes were differentially expressed only in my RNA sequencing data set. Among those 72 genes were genes related to extensins, pectin modification, expansins and xyloglucans (Figure 24, D). Among those genes that were found in both data sets I found absolutely no extensins but a lot of

cellulose related genes (Figure 24, D). All cellulose related genes (like CESA1, CESA2, CESA3, CESA5) encode cellulose synthase isomers that are important for primary cell wall. They can be found downregulated in the rlp44 mutant transcriptome and upon enhanced auxin biosynthesis. This data could be explained by a first auxin induced cell wall related event, that is potentially sensed by RLP44 and subsequently some cell wall remodeling downstream of RLP44. For a better temporal resolution transcriptome analysis of samples harvested earlier after ethanol treatment would be necessary. It would be interesting to observe the effect of induced auxin biosynthesis in the starch sheath in a rlp44 mutant background. Overall, the RNA sequencing delivered useful information, like the earlier enhancement of transcripts of cambium related genes like WOX4 and PXY, and the differential expression of cell wall related genes, that are potentially eminent for the process of interfascicular cambium formation. The comparison with the rlp44 mutant transcriptomic revealed a possible involvement of RLP44 in this process.

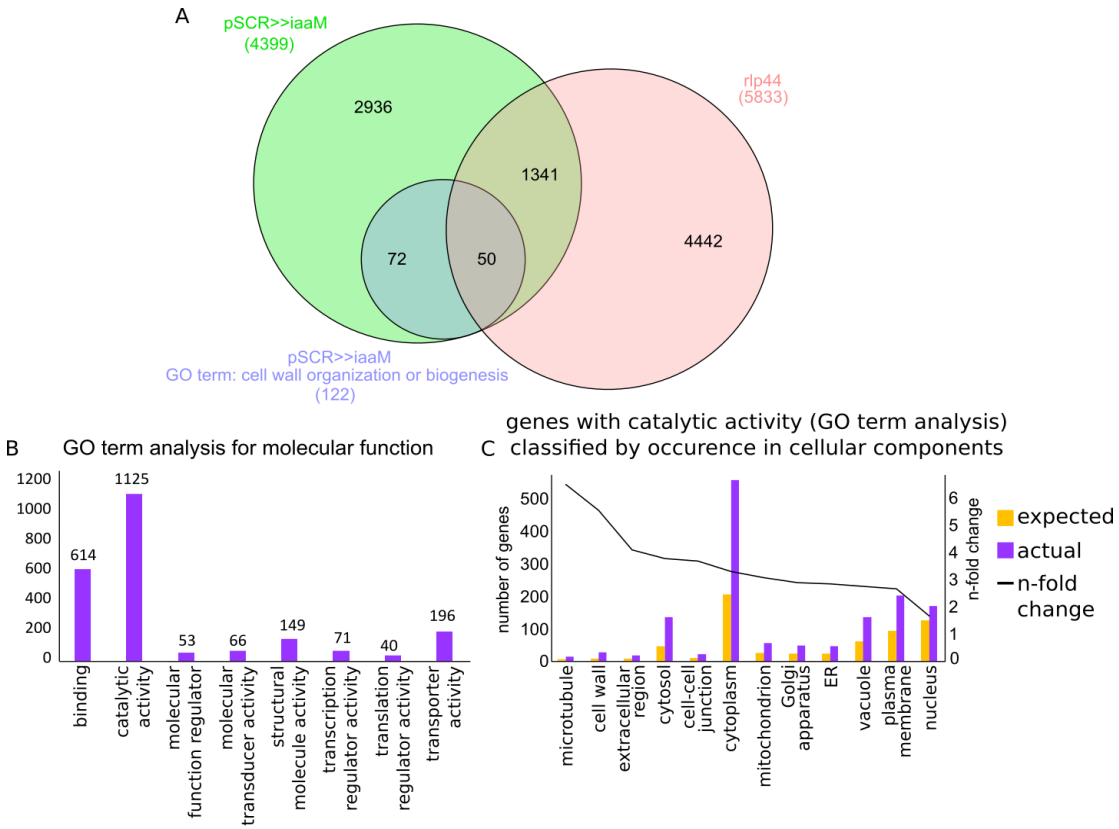

D

			n-fold	
	Gene description	Locus	pSCR>>iaaM	rlp44
both data sets	EXP15	AT2G03090	0.15	0.21
	EXP5	AT3G29030	0.05	0.45
	PME35	AT3G59010	3.18	0.24
	PME44	AT4G33220	0.21	0.61
	PME34	AT3G49220	0.17	0.72
	CESA5	AT5G09870	0.52	0.54
	CESA2	AT4G39350	0.64	0.59
	CESA6	AT5G64740	0.46	0.66
	CESA1	AT4G32410	0.68	0.78
	CESA3	AT5G05170	0.70	0.80
only in pSCR>>iaaM	EXT3	AT1G21310	23.81	
	EXT21	AT2G43150	8.96	
	EXP20	AT4G38210	3.19	
	EXPA4	AT2G39700	2.51	
	EXLA3	AT3G45960	2.49	
	EXP8	AT2G40610	0.03	
	PMEI6	AT2G47670	2.73	
	PME31	AT3G29090	1.88	
	PME17	AT2G45220	0.33	
	XTH23	AT4G25810	9.91	
	XTH28	AT1G14720	5.85	
	XTH6	AT2G36870	0.27	
	XTH18	AT4G30280	0.18	

Figure 24 ***Comparison of the RNA sequencing dataset of pSCR>>iaaM 5 DAT with RNA sequencing dataset of rlp44 mutant from samples collected in the stem of A. thaliana****. Venn diagram (A) and an exemplary list of genes found differentially expressed in both data sets or only in pSCR>>iaaM.*

3.6. Effect of cell wall remodeling on interfascicular cambium initiation

Cell wall remodelling took place during the IC formation, that is induced by expression of *iaaM* in starch sheath cells. Data from the RNA sequencing as well as from the immunohistochemistry assays suggested that especially pectin modification occurred.

3.6.1. Histological study of additive effects of pectin modification during interfascicular cambium formation

As results from the immunohistochemistry assays suggest a change of pectin methyl-esterfication towards the de-methylated calcified state and RNA sequencing show PECTIN METHYL ESTERFERASES (PMEs) in most cases upregulated I tested the effect of *PECTIN METHYL ESTERFERASE3* (*PME3*) on IC formation via histology. I performed histological analysis of toluidine blue stained cross sections of the second internode of wild type and the transgenic lines expressing only *iaaM*, only *PME3* or *iaaM* and *PME3* simultaneously upon ethanol treatment 10 DAT.

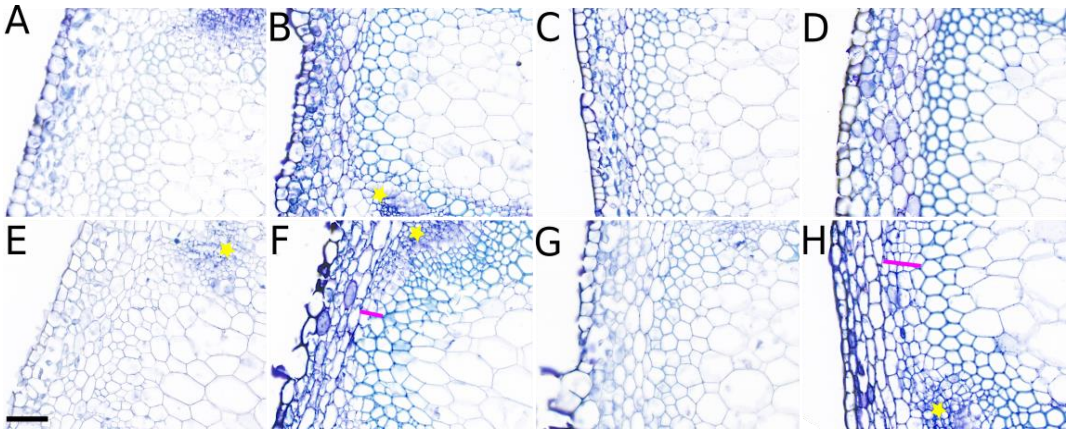

Figure 25 *Histological analysis of toluidine blue stained cross sections of the second internode of transgenic plants expressing iaaM or pme3 or iaaM and pme3 upon ethanol treatment revealed no histological effect of cell wall alteration on de-novo formed IC. Wild type control does not show cell file formation 10 DAT in control groups (A) or ethanol treatment (E). Control plants do not show cell file formation in any case (A – D). Cross sections from the transgenic line expressing iaaM after ethanol treatment show cell file formation, highlighted with a purple line (F). Cross sections of pme3 expressing ethanol treated plants did not show cell file formation in the interfascicular region (G). In plants expressing iaaM and PME3 in parallel after ethanol induction (H) no additive effect of pme3 on cell file formation was observed.*

In the wild type situation (Figure 25, A + E) no formation of cell files is visible no matter of the treatment. In the transgenic line, that expresses

iaaM upon ethanol induction the formation of cell files is visible cross sections of the ethanol treated plants (Figure 25, F). In transgenic plants that express *PME3* under the starch sheath specific SCARECROW promoter no cell files can be found in the interfascicular region (Figure 25, G). To investigate whether cell wall modification can have an additional effect on cell file formation in presence of auxin I checked toluidine blue cross sections of plants that expressed *PME3* and *iaaM* in parallel. I find cell files in the interfascicular regions of the cross sections in ethanol treated plants (Figure 25, H) but could not find any additional effects when I compared the samples with cross sections of the plants with induced auxin biosynthesis.

Furthermore, I explored the additional effect of pectin methyl esterase inhibitors on cell files formation in the interfascicular region if expressed in parallel to auxin. I expressed two different pectin methyl esterase inhibitors, *PECTIN METHYLESTERASE INHIBITOR 3 (PMEI3) and PECTIN METHYLESTERASE INHIBITOR 5* (*PMEI5*) in an ethanol inducible manner under the control of the *SCR* promoter. To catch all possible additive effects and dynamics, I collected samples 5 DAT and 10 DAT for the histological analysis. Wild type plants do not show cell files formation in the interfascicular region no matter how they were treated and when they were harvested (Figure 25, A + E and I + M). In cross sections of the plant line with increased auxin biosynthesis upon ethanol treatment, cell files were observed in the samples that where harvested 10 DAT (Figure 26, N) in samples that were harvested 5 DAT the formation of cell files in the interfascicular region was only observed in one out of seven samples (Figure 26, F). In samples of the plants that expresses *iaaM* and *PMEI5* in parallel two interesting observations could be made. Cell files in the interfascicular region were larger at an earlier time point (Figure 26, Q) and the cortex was enlarged already 5 DAT (Figure 26, G and O) cells in the cortex enlarge, especially 10 DAT starch sheath cells are increased in their size (Figure 26, O). In samples of plants that express *PMEI3* in parallel to *iaaM* a negative effect on cell file formation could be observed (Figure 26, H + P). At 10 DAT only one out of seven samples showed cell files even though *iaaM* was expressed simultaneously. The cortex was not increased in size as it was the case when *PMEI5* was expressed together with *iaaM*. From this results it can be concluded, that cell wall remodeling is an important aspect during IC

formation. Especially de-methyl esterification of the cell wall seems to by an key event. This is supported by the result, that IC formation was partially blocked by inhibiting pectin de-methyl esterification by expressing *PMEI3*. The IC formation could not be induced by expressing *PME3*, which supports together with results from above the importance the nuclear auxin signaling.

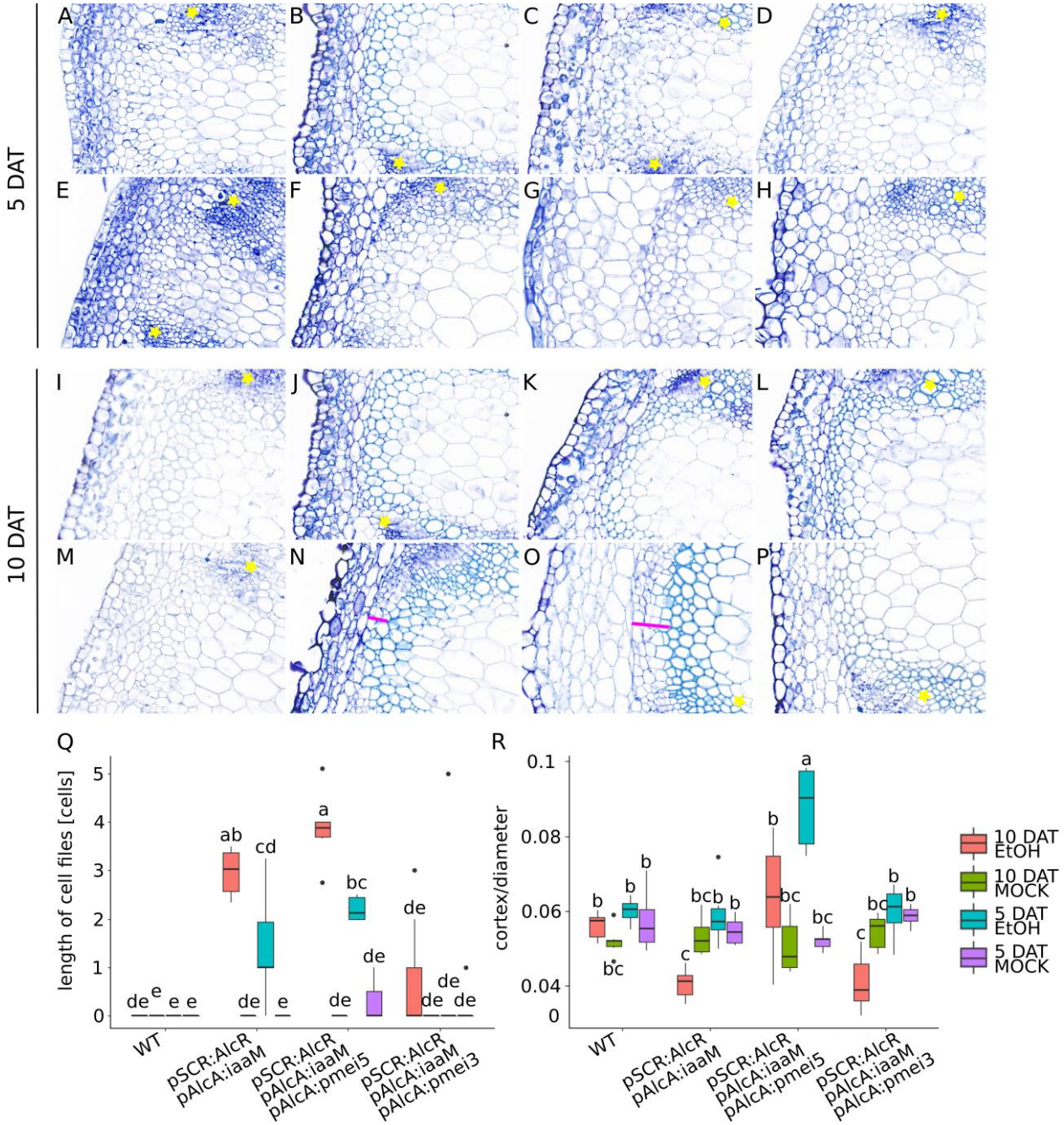

Figure 26 ***Histology of cross sections of the second internode of wild type and transgenic lines expressing pSCR:AlcR, pAlcA:iaaM and cell wall remodeling pmei5 or pmei3 show oposite effects of pmei´s when expressed in parallel to iaaM.*** *Cross sections are toluidine blue stained and show the interfacicular region of the second internode of wild type control (A, I), wild type ethanol treated (E, M), pSCR:AlcR, pAlcA:iaaM control (B, J), pSCR:AlcR, pAlcA:iaaM ethanol treated (F, N) pSCR:AlcR, pAlcA:iaaM, pAlcA:pmei5 control (C, K) pSCR:AlcR, pAlcA:iaaM, pAlcA:pmei5 ethanol treated (G, O), pSCR:AlcR, pAlcA:iaaM, pAlcA:pmei3 control (D, L) and pSCR:AlcR, pAlcA:iaaM, pAlcA:pmei3 ethanol treated (H, P), vascular bundels are marked with a yellow asterisk, cell files are indicated with a purpel line Length of cell files was analyzed and revealed the additive effect of pmei5 when expressed in paralell to iaaM and the repressive effect of pmei3 when expressed in parallel with iaaM. The ratio of cortex to diameter was analyzed and show a reduced cortex in plants expressing iaaM and iaaM + pmei3 10 DAT wheras this ratio was increased in plants expressing iaaM + pmei5 5DAT/ 10DAT (R), statistically significant difference is revealed by ANOVA with n = 7.*

3.7. Brillouin microscopy

The plant cell wall is a multicomponent network that can provide stability for the whole plant while it needs to be flexible at the same time to allow the plant (cell) to grow and extend. This ambivalent properties are realized by changes in cell wall composition or enzymatic activity (Durachko and Cosgrove, 2009; Peaucelle et al., 2011). To access the change of the elasticity modulus (M') of cell walls in response to cell wall modifying treatments or genetic modifications a Brillouin microscope set up was constructed and used. Thereby my work was framed and guided by Dr. Kareem Elsayad, who configured and constructed the first set up and Dmitry Richter who finalized the set up and wrote the Matlab based software to control hardware and analyse the recorded spectral data.

3.7.1. Brillouin microscope set up

The Brillouin microscope set up consists out of three parts, the excitation or illumination part, the microscope and the Brillouin spectrometer (Figure 27 – 29). For the illumination part a stable laser line is needed, here we used a Cobolt samba 532.1 nm, Diode-Pumped Solid-State Laser (DPSSL) (Figure 27, A). The laser line is passed through a Farraday rotator (Figure 27, B) to obtain a large attenuation for back-reflected light. After passing the Farraday rotator the laser beam was filtered by a single-mode fiber for side bands which lead to a Gaussian beam profile at the exit. Leaving the SM fiber, the beam is collimated to a diameter of 3 mm by a collimator lens (Figure 27, E). The polarizing beam splitter with an integrated half-wave plate (Figure 27, G) is used to allow rotation of the linear polarization and a splitting of the beam depending on its polarization. The following narrow band pass filter

(Figure 27, H) transmits light within a band width of 2nm thereby excluding all potentially interfering components. The beam passing the quarter wave plate (Figure 27, I) and a telescope (ratio of focal lengths of 1:3) results in a circular polarized and expanded beam with a diameter of 9 mm which slightly overfills the back aperture of the microscopes objective (20x, 0.5 NA) (Figure 27, L). The low numerical aperture of the microscope objective ensures low spectral broadening (higher spectral resolution) and a closer approximation to the 180° measuring geometry (Antonacci et al., 2013).

Light interacts with the sample and is scattered back, in an angle of 180° through the objective, passing again the beam expander, which now has an opposite effect on the beam diameter and reduces the beam diameter to 3 mm. As light travels back again through the quarter wave plate (90° linearly polarized) it passes the polarizing beam splitter and is coupled with a microscope objective (10x, 0.25 NA) (Figure 27, M) into a single mode fiber (0.12 – 0.14 NA) that placed in a six axis SM fiber coupler (Figure 27, N).

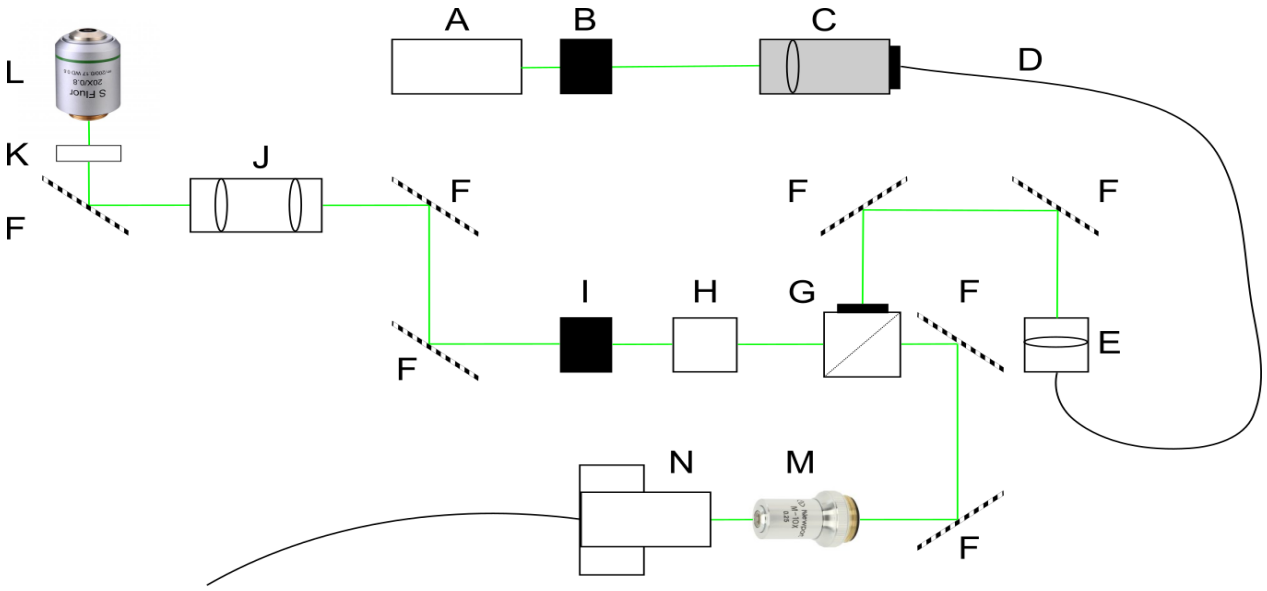

		component	provider	specifications
Excitation path	**A**	Laser	Cobolt	532,1 nm, 100 mW
	B	Farraday rotator/ isolator	Thorlabs	IO-5-532-HP
	C	Fibre coupler	Kinelex	
	D	Single mode fiber	Kineflex	APC, polarizing maintaining, beam diameter 0.7 mm
	E	Colimator	Thorlabs	F260APC-A, f = 15.01 mm
	F	Mirror	Thorlabs	
	G	Polarizing beam splitter	Thorlabs	VA5-532/M
	H	Band pass filter	AHF	HC Laser Clean-up MaxLine 532/2 (D=25mm)
	I	Quarter wave plate	Thorlabs	WPMQ05-M
	J	Beamexpander (1:3)	Thorlabs	f_1 = 25 mm/ f_2 = 75 mm
	K	Bandpassfilter	Thorlabs	
	L	Plan Fluor, Objective	Nikon	20x, 0.5 NA
	M	Objective	Newport	10x, 0.25 NA
	N	SM fiber coupler	Newport	F-91-C1

Figure 27 ***Scheme of the illumination part of the final Brillouin microscope set – up****, laser (A), Farraday rotator (B), fiber coupler (C), SM fiber (D), collimator (E), mirrors (F), polarizing beam splitter (G), narrow band pass filter (H), quarter wave plate (I), beam expander (J), band pass filter (K), microscope objective (L), microscope objective (M) and SM fiber coupler (N).*

The signal from the sample is transmitted though the SM-fiber into the Brillouin spectrometer and collimated at the fiber exit. All used collimators have an 8° beveled APC connector to avoid reflected light to travel back in the fiber and cause any kind of interferences. The collimated light beam passes the first cylindrical lens (Figure 28, P) and is focused on the entrance window of the first VIPA (R_1= 95.0%, R_2 >99.7% at 532 nm), (Figure 28, Q) after which the beam is dispersed. The second cylindrical lens (Figure 28, R) is used to focus the light on the first slit after passing the VIPA. The first adjustable slit (Figure 28, S) is used to spatially filter the elastically scattered light from the sample. The first spherical lens (Figure 28, T) focuses the light at the second

VIPA (Figure 28, U), that is oriented perpendicular to the first VIPA. After the second spherical lens a Lyot stop filter (Figure 28, X) is introduced to enhance the signal contrast by suppression of diffracted light components and enlarge the Brillouin signal pattern by the factor 3 (f_1/f_2 = 3). The sCMOS camera from PCO (Figure 28, Y) acquires the Brillouin signals with its 2048 x 2048 active pixels. To enhance the signal even more, the binning of the camera was set to 2.

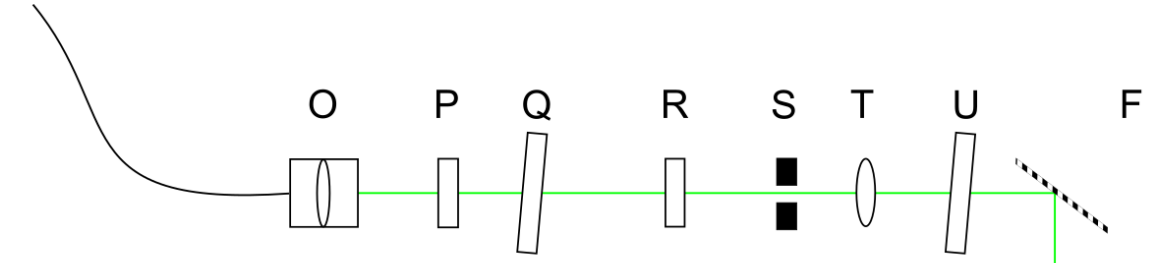

		component	provider	speciications
Spectrometer	**O**	Collimator	Thorlabs	F260APC-A, f = 15.01 mm
	P	1st cylindrical lens	Thorlabs	f = 200 mm
	Q	1st VIPA	SLS Optics	FSR ~30 GHz
	R	2nd cylindrical lens	Thorlabs	f = 200 mm
	S	1st slit	Thorlabs	VA100-M
	T	1st spherical lens	Thorlabs	f = 200 mm
	U	2nd VIPA	SLS Optics	FSR ~30 GHz
	V	2nd spherical lens	Thorlabs	f = 200 mm
	W	2nd slit	Thorlabs	VA100-M
	X	Lyot stop filter	Thorlabs	2 x f = 40 mm
	Y	PCO.edge camera	PCO	sCMOS sensor, 2048 x 2048 pixel

Figure 28 ***Scheme of the spectrometer part of the final Brillouin microscope set – up,*** *collimator (O), 1st cylindrical lens (P), 1st VIPA (Q), 2nd cylindrical lens (R), 1st slit (S), 1st spherical lens (T), 2nd VIPA (U), 2nd spherical lens (V), 2nd slit (W), Lyot stop filter (X), camera (Y).*

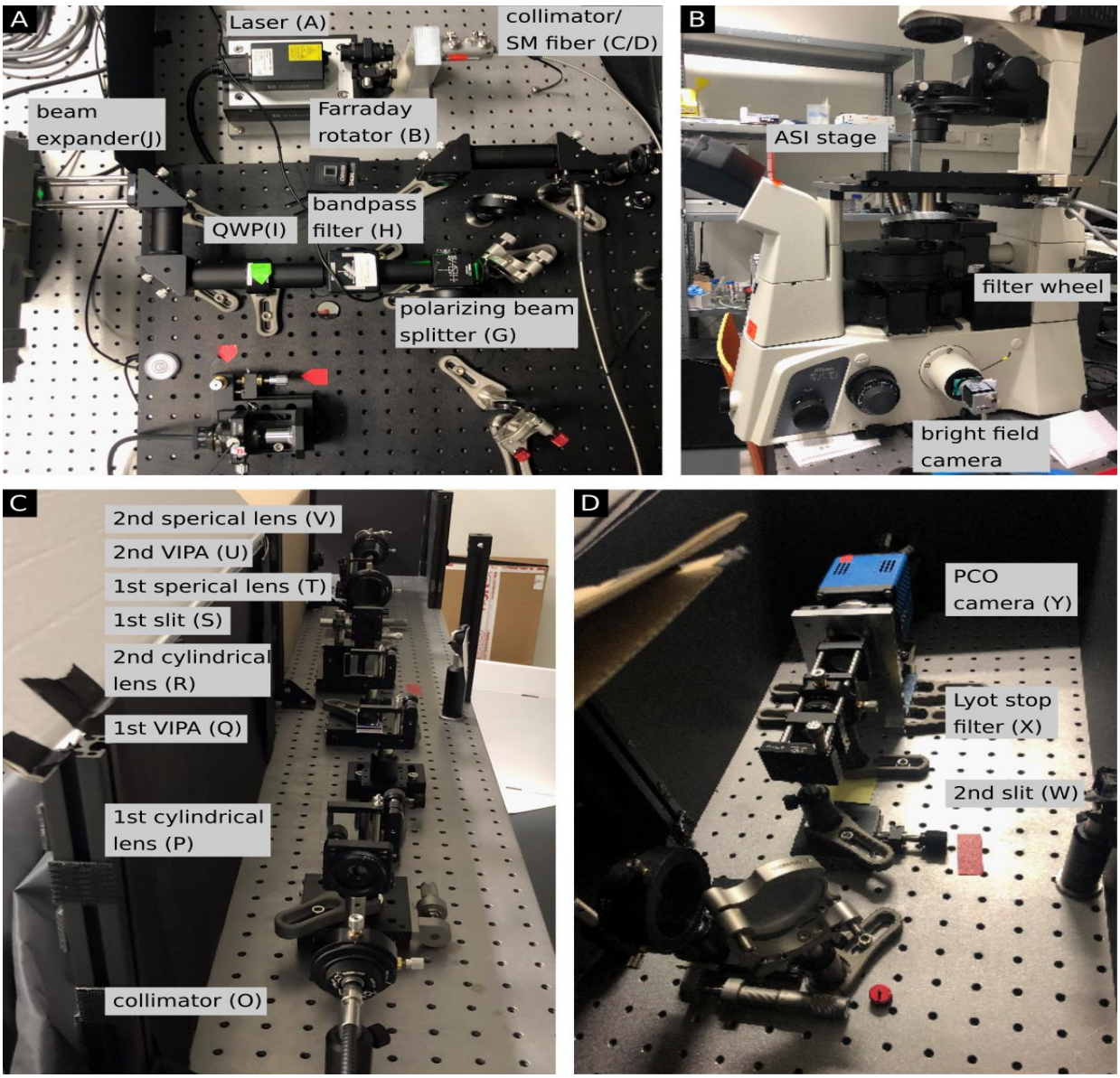

Figure 29 ***Photograph of the Brillouin microscope set up (taken by Dmitry Richter)****, illumination part (A), the microscope body (B), the spectrometer (C) and the camera (D) with all components named in the picture.*

3.7.2. Brillouin signal

To follow up the occurrence of the typical water Brillouin signal I recorded camera images (with open slits) after each component that I placed into the light path at different acquisition times. First, I took a picture of the unprocessed, collimated laser beam delivered by the SM fiber with an acquisition time of 0.5 ms (Figure 30, A). With the first VIPA being in place, the light is reflected several times between the highly reflected surfaces allowing a small portion to exit the VIPA after each round which creates an array of multiple diffraction orders (Figure 30, B). Through the spherical lens that is placed after the VIPAs the signal is Fourier transformed, which results in a transformation from a spectral dispersion into a spatial dispersion along the spectral axis of the VIPA (Scarcelli and Yun, 2011). After adding the second VIPA in a cross axis conformation Rayleigh signal can be found in diagonal points on different diffraction orders (Figure 30, D) as a result of diagonal dispersion due to the second perpendicular VIPA. After closing both slits to physically cut out the Rayleigh signal and increasing the acquisition time to 550 ms I obtained the Brillouin signal of water (Figure 30, E) and poly styrene (Figure 30, F). Next, I acquired the corresponding spectra (Figure 30, C) by analyzing signal intensity across a spectral line (yellow line in Figure 30, E). The Brillouin shift has to be seen relative to the elastic Rayleigh scattering (signal is not shown in Figure 30, C), and so water shows a smaller Brillouin shift compared to the much stiffer material poly styrene. The final step is, to adjust the Lyot stop filter, that is still open in Figure 30, G. After I closed the aperture of the Lyot stop filter (Figure 30, H) the elastically scattered light was suppressed.

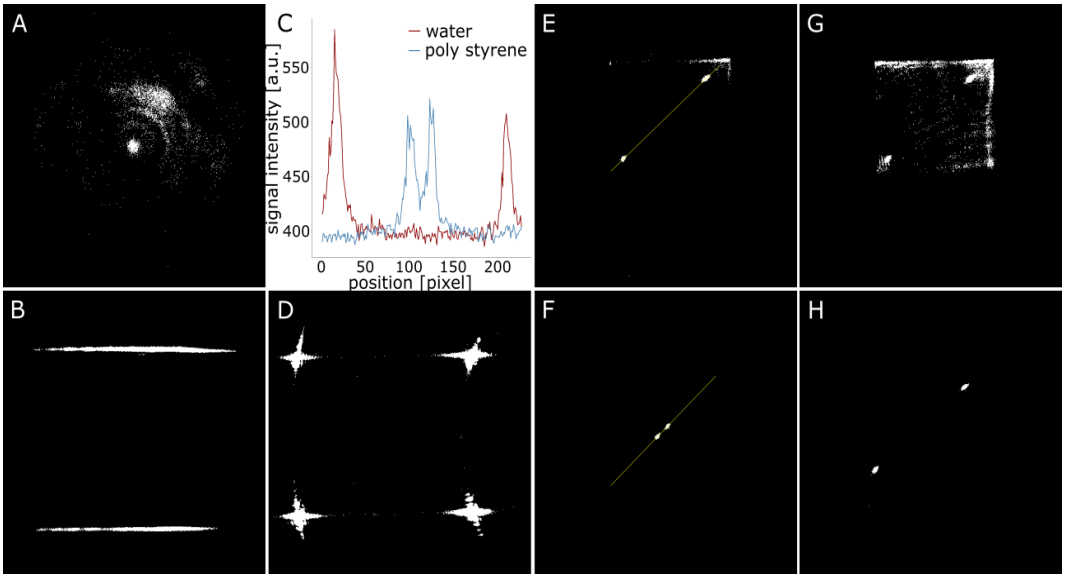

Figure 30 ***Beam profile/ Brillouin spectra of the beam scattered back from the sample and its processing in the spectrometer****; unprocessed beam (A), beam profile after passing the first VIPA (B), beam profile after passing the second VIPA (D), Brillouin signal on the camera of water (E) and poly styrene (F) and the related spectra of both (C),yellow line corresponds to spectral line, Brillouin signal of water on the camera without Lyot stop (G) and with closed Lyot stop (H).*

3.7.3. Shifts of Brillouin signal of glycerol solutions and agarose gels

As a proof of concept I measured the Brillouin signal of different solutions with increasing glycerol concentrations. Glycerol is known for its influence on viscoelastic properties (Bund and Schwitzgebel, 1998). Furthermore, I measured the Brillouin shift in agarose gels of different agarose concentrations. Agarose is a biopolymer that forms a macromolecular three-dimensional network and is in this respect similar to the plant cell wall. I performed 100 measurements in all samples and averaged them.

The relationship between rising glycerol concentrations and increased Brillouin shifts is shown in Figure 31, A. For a pure water sample the typical shift is 7.5 GHz. In contrast, a sample that contained 40% glycerol leads to a shift of 9.0 GHz. The increase can be described as linear by $y = 0.433x + 7.504$ ($R^2 = 0.9989$). As expected, the results can be interpreted by an increase of the elasticity modulus in solutions with higher glycerol concentration. The Brillouin shift measurements of agarose gels at different agarose concentration are displayed in Figure 31, B. With increased agarose concentration, gels showed the expected increase of the Brillouin shift ranging from 7.26 GHz for a gel with 0.5 %

agarose up to 7.34 GHz for a gel containing 2.5 % agarose. The relation between Brillouin shift and agarose concentration can be described as sigmoidal. The sigmoidal relation between Brillouin shift and agarose concentration is surprising, because it is known from compression experiments that the elasticity modulus should increase linearly with the agarose concentration (Ed-Daoui et al., 2019).

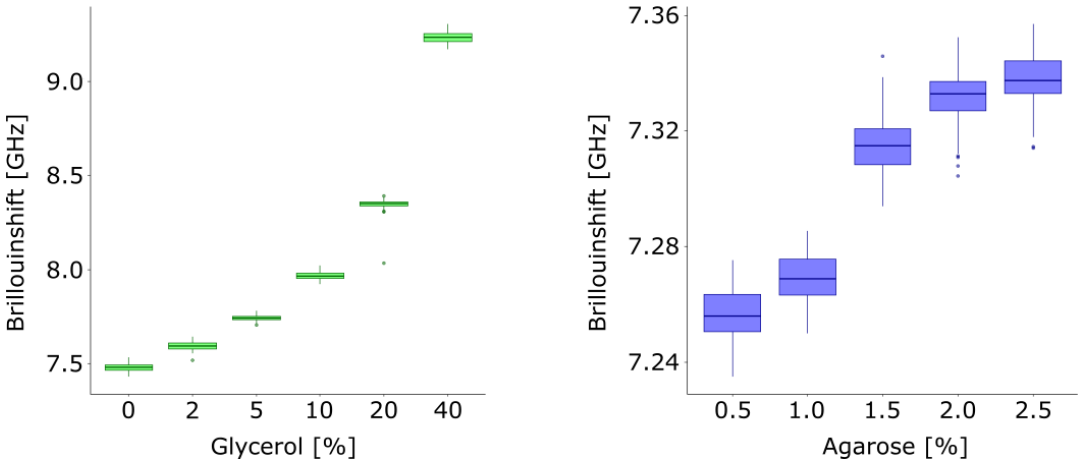

Figure 31 ***Brillouin shift [GHz] increases with higher glycerol content (A) and follows a linear regression, indicating that Brillouin light scattering provides a meaningful measure of bulk stiffness. Brillouin shift increase with increase in agarose concentration (B)***

3.7.4. Shifts of Brillouin signal of cellulose – callose hydrogels

The texture of cell walls can be described as polysaccharide hydrogels. Therefore, I was interested in the behaviour of hydrogels which are composed of typical cell wall polymers. Samples of hydrogels from cellulose and callose were provided by the lab of Yoselin Benitez-Alfonso. Those hydrogels had a polymer content of 10 % in all cases and were mixtures of cellulose and callose at different ratios. I measured 100 data points at three different positions in all provided samples (Figure 32).

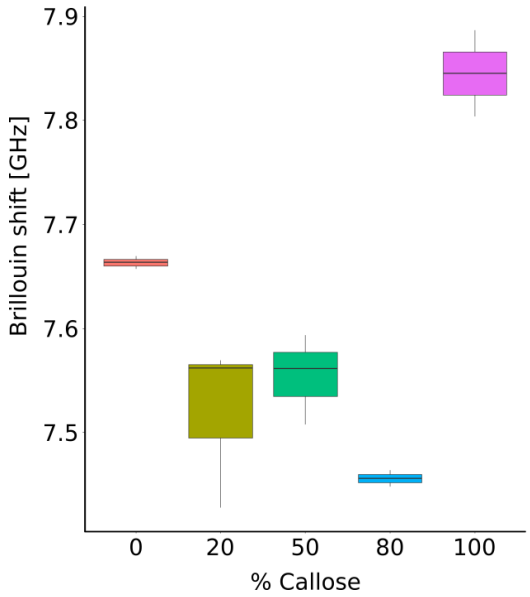

Figure 32 ***Brillouin shift of cellulose-callose hydrogels of different ratios (provided by the lab of Yoselin Benitez-Alfonso).*** *All samples were measured at three different positions with 100 data points each. The average Brillouin shift range from 7.65 GHz for pure Cellulose Hydrogels down to 7.45 GHz for Hydrogels with 80 % Callose, the differences between the samples are not significant due to the high variability within one sample.*

In conclusion it can be said, that Brillouin shifts are getting smaller with higher callose content, indicating a material with smaller elasticity modulus which is consistent with the AFM measurements on cellulose-callose hydrogels determining the Youngs modulus of the material with the same trend (R. Abou-Saleh et al. (2018)). The interesting behaviour of pure callose, showing a much higher Brillouin shift indicating a much higher elasticity modulus than pure cellulose but also than mixtures with cellulose and callose was not shown in published AFM measurements of those hydrogels.

3.7.5. 2D map of Brillouin shift of the cell wall in different developmental zones of the root revealed differences in cell wall elasticity modulus

After having established Brillouin spectroscopy as reliable method to study a materials stiffness, I investigated the stiffness of a root sample. From the side of developmental biology roots are an interesting system to study, because they provide a developmental gradient along their longitudinal axes, with young cells located close to the root tip and the root meristem (RM) and older cells being at the root base. Apart from that, roots can be easily imaged because they are mostly transparent. Cells in different regions show different behavior and so it can be

assumed that cell walls in different zones have different properties e.g. composition and elasticity. Cells in the meristematic zone are dividing very frequently and the surrounding cell wall is very thin (Pacifici et al., 2018; Rahni and Birnbaum, 2019). Cells in the elongation zone need to expand along the longitudinal axes which is mainly realized by cell wall remodeling enzymes that loosen the cell wall and allow the cell to give in the turgor pressure (Pacifici et al., 2018). In the differentiation zone, cells reach their final size and are fully functional.

Because of this very different requirements, cell walls should have different properties with regard to their elasticity and are a perfect system to investigate further with the help of Brillouin microscopy.

I used roots of wild type (Col-0) plants 5 DAG, grown on vertical plates in long day condition and investigated the Brillouin shifts of cell walls of the epidermal layer in the meristematic zone, the elongation and the differentiation zone, respectively. In Figure 19, results of these measurement are displayed. Each column in Figure 19 corresponds to one sample (meristematic zone, the elongation and the differentiation zone). The bright field pictures in the first column of Figure 33 were used to localize the cell wall within each sample. The heat maps used for the representation of the signal intensity and the Brillouin shifts (2nd and 3rd column in Figure 32) display low values with dark purple color and high values with yellow color. Pixels where the underlying spectrum could not be fit are black. Pixel values for all Brillouin shift maps were set to a range from 7.38 GHz and 8.08 GHz. The lower end of the Brillouin shift scale corresponds to the medium outside of the samples which are mainly water and agarose and have pixel values of around 7.4 GHz.

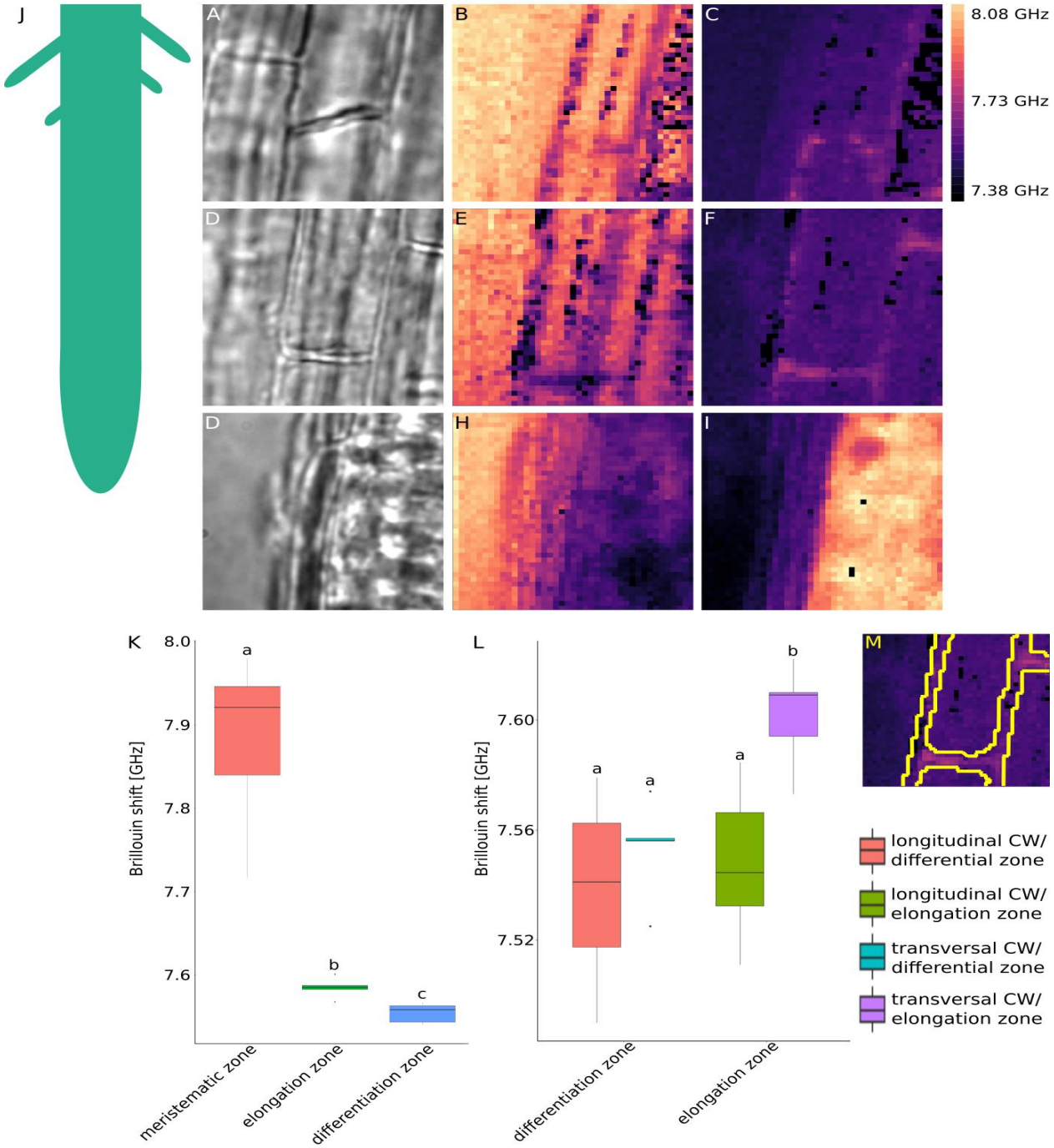

Figure 33 ***Brillouin shift and intensity map revealed differences in mechanical properties within the cell walls in different zones in root****. Brightfield picture of the differentiation zone (A) corresponding Brillouin intensity map (B) and Brillouin shift map (C) brightfield picture of epidermal cells in the elongation zone (D) corresponding Brillouin intensity map (E) and Brillouin shift map (F), brightfield picture of epidermal cells in the meristematic zone (G) corresponding Brillouin intensity map (H) and Brillouin shift map (I), quantification of the Brillouin shift all zones (K) and longitudinal and transversal cell walls separately (L), statistically significant difference is revealed by ANOVA with n = 9, exemplary mask (M).*

To analyse the Brillouin shifts of cell walls I created a mask (ROI – region of interest) with the open source software FIJI (example given in Figure 33, M) utilising the signal intensity map. Pixels within the mask belong to the cell wall were averaged and summarized in Figure 33 K. Starting with cell walls in the differentiation zone (Figure 33, A, B and C) the average Brillouin shifts of the cell walls is around 7.55 GHz. Cells of the elongation zone are shown in the second line, bright field pictures (Figure 33, D), Brillouin signal intensity map (Figure 33, E) and Brillouin shift map (Figure 33, F) respectively. Signal analysis was done as described earlier, cell walls of the elongation zone have an average Brillouin shift of 7.58 GHz. The last row shows the bright field pictures (Figure 33, G), Brillouin signal intensity map (Figure 33, H) and Brillouin shift map (Figure 33, I) of cells in the meristematic zone. Interestingly cell walls cannot be distinguished in the meristematic zone, neither in the Brillouin signal intensity map nor in the Brillouin shift map. Here, the whole sample gives relatively high values for the Brillouin shift compared to the other zones. To analyze this particular zone, I created a mask covering the meristematic area and averaged all pixel value which resulted in an averaged Brillouin shift of 7.93 GHz.

As bigger Brillouin shifts can be correlated with a larger elasticity modulus, I can conclude that the meristematic zone of the root is “stiffer” than the elongation and differentiation zone. The “stiffness” difference is not as big between elongation and differentiation zone, but the differentiation zone is “softer” than the elongation zone. This result was unexpected because cells in the elongation zone expand and therefor their wall needs to be softer to be able to stretch.

3.7.6. 2D map of Brillouin shift of the cell wall of any1 and kor1-3 mutants revealed changes in cell wall elasticity modulus

To investigate changes of the Brillouin shifts of cell walls in mutants that are known for their changed cell wall properties, like composition, crystallinity and elasticity I used the *anisotropy1* mutant (*any1*) and the *korregan1* mutant (*kor1-3*). I chose the *any1* mutant because it is known that the *ANY1* gene encodes for a cellulose synthase and the corresponding mutant shows reduced cell wall crystallinity (Fujita et al., 2013) and a smaller Young´s modulus in the SAM compared to the wild

type (Sampathkumar et al., 2019) and smaller longitudinal modulus in pavement cells (Altartouri et al., 2019). *KOR1* is also associated with the cellulose synthesis complex and organizes, as membrane-associated endoglucanase, cellulose in the wall. The *kor1-3* mutant is known to have altered cell wall composition (His et al., 2001). From studies in rice and poplar it had been suggested that endoglucanases can hydrolyze cellulose and xyloglucan and cause wall relaxation and expansion (Shani et al., 2006). Both mutants are dwarf and affected in the length of their elongation zone (Figure 34, J), so I scanned cell walls of the epidermal layer in the elongation zone.

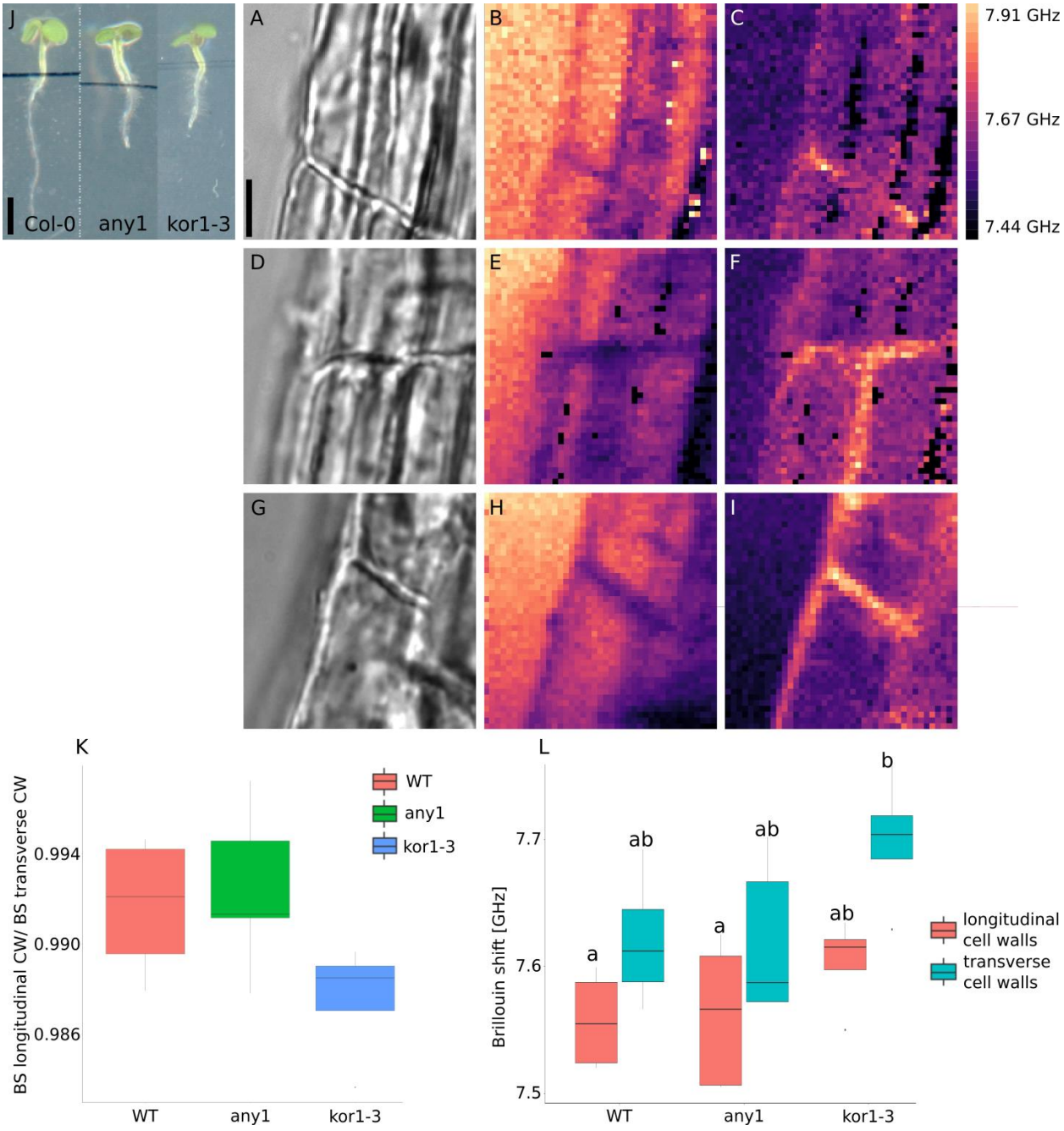

Figure 34 ***Brillouin shift and intensity map of longitudinal and transversal cell walls in the elongation zone of the root revealed differences in mechanical properties between cell walls of different orientation and between wild type and KORREGAN mutant****. Brightfield picture of epidermal cells in the elongation zone of wild type with scale bar = 10 µm (A) and corresponding Brillouin intensity map (B) and Brillouin shift map (C) Brightfield picture of epidermal cells in the elongation zone of any1 mutant (D) and corresponding Brillouin intensity map (E) and Brillouin shift map (F), Brightfield picture of epidermal cells in the elongation zone of kor1-3 mutant (G) corresponding Brillouin intensity map (H) and Brillouin shift map (I), quantification of the Brillouin shift of longitudinal and transverse cell walls in wild type, any1 and kor1-3 mutant (L) statistically significant difference is revealed by ANOVA with n = 5, ratio of the Brillouin shift of longitudinal cell walls and the Brillouin shift of transverse cell walls is not significant different but shows a trend for kor1-3 (K).*

The scanned area was 40 μm x 40 μm with an acquisition time of 550 ms per pixel while the laser power on the sample was around 5 – 6 mW. To localize the region of interest I used the bright field picture (Figure 34 A, D, G). The Brillouin signal was analyzed with a Matlab script and results in a map of pixel properties like, signal intensity, peak width and Brillouin shift. The color code of Brillouin intensity (Figure 34 B, E, H) and Brillouin shift maps (Figure 34 C, F, I) are similar as described in the previous section. The lower limit of the Brillouin shift value was set to 7.44 GHz whereas the upper limit was 7.91 GHz, respectively.

As the Brillouin signal intensities shows clear differences between cell wall and lumen, possibly because of the difference in optical density of both regions. I used the Brillouin signal intensity maps to create a mask for longitudinal and transversal cell walls and applied the masks to the Brillouin shift maps and averaged the contained pixel values in each map.

I found significant differences when I compared the Brillouin shift of longitudinal and transversal cell walls in all three genotypes. The Brillouin shift was smaller in the longitudinal cell walls indicating a more elastic longitudinal cell wall compared to the transverse cell wall. Interestingly the any1 mutant did not show differences in Brillouin shift compared to the WT while the difference between longitudinal and transverse cell walls remained. In the kor1-3 mutant longitudinal cell walls generated a slightly bigger Brillouin shift than those in WT and any1 mutants. Transverse cell walls have a significantly bigger Brillouin shift compared to those in WT and any1 mutants. This trend is confirmed by the ratio of the Brillouin shift of longitudinal cell walls and the Brillouin shift of transverse cell walls (figure 34 K) even though results are not significantly different. The differences between longitudinal and transversal cell walls were expected, because cells in the elongation zone need to stretch along the longitudinal axis. It is surprising that the any1 mutant does not show any differences from the WT regarding the Brillouin shift in the elongation zone of the root, because it was shown that in pavement cells any1 mutants show clear differences to the WT regarding their longitudinal modulus (Altartouri et al., 2019).

3.7.7. 2D map of Brillouin shifts of the shoot apical meristem after isoxaben treatment revealed lower elasticity modulus in deeper tissue layer

Another plant organ that is interesting with respect to its mechanical properties is the shoot apical meristem. This is the location where the stem cell niche is residing, which gives rise to the most tissue that is produced above the ground. The stem cells can be found in the central zone within three clonally distinct cell layers (L1–L3), which give rise to epidermis, ground tissue and vasculature (Gaillochet et al., 2015). The shoot apical meristem (SAM) is nearly transparent and colourless, which makes it easy accessible for all kinds of optics. In the past it was subject of various studies about mechanical properties with atomic force microscopy (AFM) (Peaucelle et al., 2011; Sampathkumar et al., 2019) that were restricted to the surface. As the SAM consists of various cell layers with different fates it would be interesting to analyse also deeper cell layers regarding the mechanical properties. Here, I show results of an experiment where I treated a dissected SAM with isoxaben, like it was done for an experiment with following AFM measurements and compared Brillouin shifts of different cellular layers in the control and in isoxaben treated plants. Isoxaben is known to inhibit cellulose synthesis and decrease the Young's modulus determined with AFM (Sampathkumar et al., 2019).

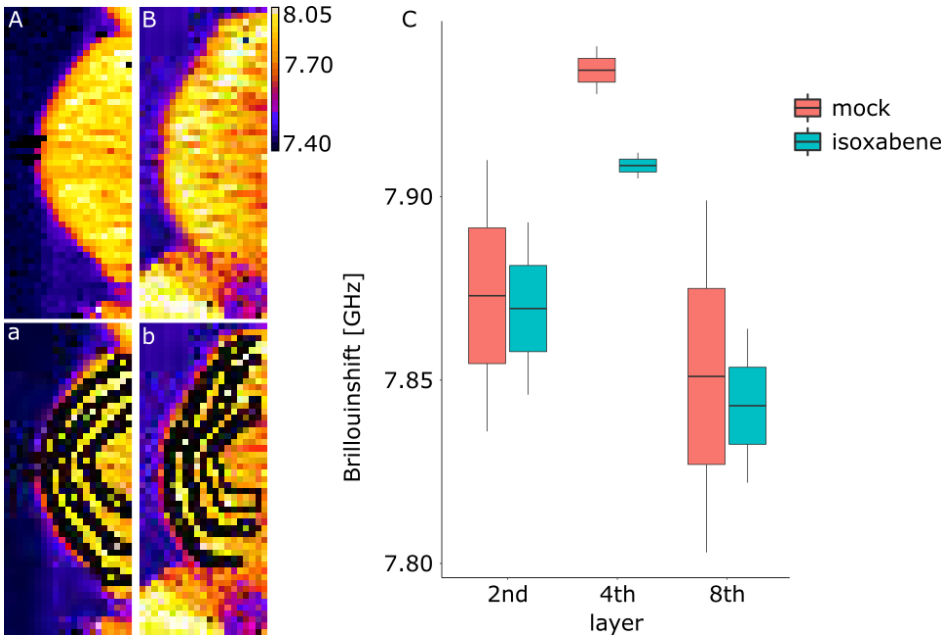

Figure 35 **Optical cross sections (xz) of the shoot apical meristem revealed differences of Brillouin shifts depending of the cell layer.** Treatment with the cellulose synthesis inhibitor isoxaben shows in the L2 layer a “softening” effect. Optical cross section of WT SAM (A) with analyzed layers (a), optical cross section of isoxaben treated WT SAM (B) and analyzed layers (b). Quantification of Brillouin shifts in analyzed layers of the control group and isoxaben treated WT SAMs (C).

I measured the Brillouin shift in shoot apical meristems and their reaction to a treatment with isoxaben. SAMs were dissected and immersed in a solution of 40 μM isoxaben over night. I imaged the SAMs at the home built Brillouin microscope at the “European Molecular Biology Laboratory” (EMBL) in cooperation with Carlo Bevilacqua at the laboratory of Robert Prevedel. As the used Brillouin microscope has an inverted design as well, I dipped the SAM into the droplet on the used water immersion objective while it was attached on the other side to an agar block to ensure position stability. This had the advantage that the Brillouin signal does not have to go through the coverglass and working distance is no restriction. For better orientation at the sample I used the expression pattern of the synthetic DR5rev::GFP reporter in the inflorescence meristem and the available GFP excitation and detection system at this microscope.

As all experiments regarding the mechanical properties within the SAM were done with the surface restricted, tactile method AFM I was interested in the behavior and differences of cell layers towards the inside of the SAM. So I took optical cross section in xz orientation of the control group of SAMs (Figure 35, A) and those that were treated with isoxaben (Figure 35, B). To analyse the effect of the isoxaben treatment I defined masks that correspond to one cell layer and analyzed pixel values in those regions (Figure 35, C). To facilitate the analysis, I analyzed only Brillouin shifts in the 2nd, 4th and 8th cell layer of the SAM. I measured a significant difference of the Brillouin shift between the 2nd and the 4th layer in the control group of samples. The 2nd layer produced a lower Brillouin shift, which indicated a more elastic material, whereas the 4th layer shows a higher Brillouin shift that should correspond to a less elastic material. The 3rd layer that was analyzed was the 8th cell layer that can be found already deep in the rib zone, that will produce the inner tissues of the stem. Here I observed lower Brillouin shifts comparable with those in the 2nd layer.

It is interesting, that different cell layers showed not only different mechanical properties in the control group but also reacted very

differently to the treatment. With a rigid cell layer (4th cell layer) that is not only especially “ridged” (like a protective shell) but also shows the biggest impact when treated with isoxaben. This kind of shell structure has been proposed by L. Beauzamy et al. (Beauzamy et al., 2015) but has never been observed before because of the lack of methods.

Interestingly, I could not observe a difference between control and isoxaben treated SAMs regarding the average Brillouin shift in the 2nd layer or in the 8th layer. However, when I checked the Brillouin shifts of the isoxaben treated SAMS in the 4th layer I could find significant differences compared to the Brillouin shifts in the 4th layer of the control treated SAMs. As smaller Brillouin shifts correlate with smaller elasticity modulus, those results recapitulate the results that were obtained with AFM, where isoxaben treated SAMs show a lower Youngs modulus.

4. Discussion

4.1. Enhanced auxin biosynthesis in the starch sheath can induce secondary growth

4.1.1. Developmental processes and their dynamics during interfascicular cambium formation

The underlying step of IC formation is the de-differentiation of differentiated cells in the interfascicular region. During this study I investigated the sequence of developmental processes and how they are coordinated during IC formation. From earlier experiments it is known that weight-induced IC initiation correlates with an auxin maximum in the interfascicular region (Mazur et al., 2014). Furthermore, it is assumed that starch sheath cells can serve as IC progenitors (Altamura et al., 2001; Sanchez, 2013). For cambium activity, WOX4 and PXY are necessary mediators of auxin signaling (Suer et al., 2011). Before the IC is initiated, no *WOX4* is expressed in the interfascicular region, the mediators between nuclear auxin signaling and IC initiation remain still unknown. In this study the starch sheath-specific *SCARECROW* promotor was used to drive auxin biosynthesis in an ethanol inducible manner to initiate the IC. I was able to induce the formation of cell files in the interfascicular region by ethanol treatment. Those *de novo* formed cell files, that were never present in the control or wild type situation, can be taken as an indicator for secondary growth. This system, will be used to study underlying events that lead to secondary growth in more detail. The ethanol inducible system was tested earlier and revealed that induction of expression starts within hours and reaches its maximum of *alcR*-mediated gene expression 5 days after treatment (DAT) (Roslan et al., 2001). Interestingly, the expression profile of *iaaM,* which is mediated by *alcR* and induced by ethanol had its maximum already 1 DAT. This relatively fast drop of expression after the induction could be explained by a negative feedback on *iaaM* expression. The system was tested at 2-week old soil grown seedlings whereas the plants that were treated in this study were about two bolt and 5 – 6 weeks old. Penetration depth of ethanol and general accessibility of the ethanol inducible construct is potentially not comparable to the previous study and could be tested easily by testing

alcR expression dynamics by qRT-PCR. The expression of the bacterial auxin biosynthesis gene *iaaM* causes higher levels of auxin (Romano et al., 1995). Auxin signaling analyzed with the auxin sensitive DR5 marker, revealed high auxin signaling output 3 and 5 DAT in the interfascicular region compared to the control situation (Figure 15). This suggests, that even though *iaaM* transcript drops, auxin biosynthesis is still high at this time. From the DR5 marker analysis it can also be concluded, that auxin signaling, even though *iaaM* is expressed only locally in the starch sheath, does not stay local but spreads along the stem radius. Auxin is a small and mobile molecule, that can be actively transported by polarized efflux carrier (PINs) or via diffusion (Friml, 2003; Kramer and Bennett, 2006). One starch sheath localized auxin efflux carrier is PIN3 (Friml et al., 2002), which I found upregulated in the RNA sequencing dataset (Figure 23). PIN3 has been found to be enriched localized at the lateral inner side of the starch sheath cells (Friml et al., 2002). The spreading of DR5 signal towards the inner stem (Figure 15), together with the upregulation of PIN3 expression could be explained by active efflux of auxin from the starch sheath towards the inner stem after being synthesized in starch sheath cells or even by passive diffusion. For a clear differentiation between active and passive transport of auxin further experiments would be necessary.

The ethanol inducible system promoting enhanced auxin biosynthesis in the starch sheath cells was used to study IC initiation on a cellular level and to investigate the dynamics of underlying developmental processes. *De novo* initiation of IC and radial growth can be subdivided into a necessary sequence of developmental steps, the de-differentiation of specified cells into cambial stem cells, subsequent proliferation of the cambium, followed by differentiation of vascular tissues. Histological analysis revealed, that 10 DAT 85 % of the cross sections of the second internode show cell files in the interfascicular region in transgenic lines with induced auxin biosynthesis. Those are completely absent in the wild type and in the control situation. Interestingly, only at this point a significant increase in diameter was observed in ethanol-treated plants carrying the above-mentioned constructs (Figure 9). An increase in stem diameter is the product of cambium proliferation and differentiation of generated cells into phloem and xylem. As the increase in stem diameter can only be observed 10 DAT and not 5 DAT and most of the cross

sections show cell files only 10 DAT the onset of cambium proliferation and differentiation can be placed between 5 DAT and 10 DAT. A significant increase of *WOX4* and *PXY* expression 5 DAT in the quantitative real-time PCR analysis (Figure 10) suggests an earlier onset of de-differentiation of starch sheath cells into the IC. Starch sheath cells were postulated as the origin of the IC (Altamura et al., 2001; Sanchez, 2013). To determine the onset of de-differentiation an expression analysis of *WOX4* and *PXY* with multiple points would be necessary. The marker analysis with cambium-specific *WOX4* and *PXY* marker lines that was performed 10 DAT revealed that the *de novo* initiated cambium cells in the interfascicular region keep their identity (Figure 11). Maintenance of their stemness and the balance between stem cell proliferation and differentiation seemed to be ensured. The results of experiments that drove the suggested sequence of developmental steps are listed in the figure below. Those are: expression profile of *iaaM* with its peak 1 DAT (represented by the blue triangle with its peak at 1 DAT), the stable auxin signaling determined by fluorescence signal intensity of DR5:YFP (represented by a yellow, uniform rectangle), *WOX4* and *PXY* expression determined at one point at 5 DAT (represented as a violet circle), WOX:YFP and PXY:YFP positive cells determined at one point 10 DAT (represented as a green circle) and the IC formation determined via histology, with an increase in cell file length between 5 DAT and 10 DAT (represented with a brown rectangle). The necessary developmental steps that lead to those results were de-differentiation starting from 5 DAT at the latest, because of the increase in expression of *WOX4* and *PXY* (depicted as a light red circle), the maintenance of stemness and proliferation of cambium cells, suggested by the pWOX4:YFP and pPXY:YFP signal in the interfascicular region (depicted as light yellow circle) and the de-differentiation suggested by the elongating cell files visible in the histology (depicted in the blue circle).

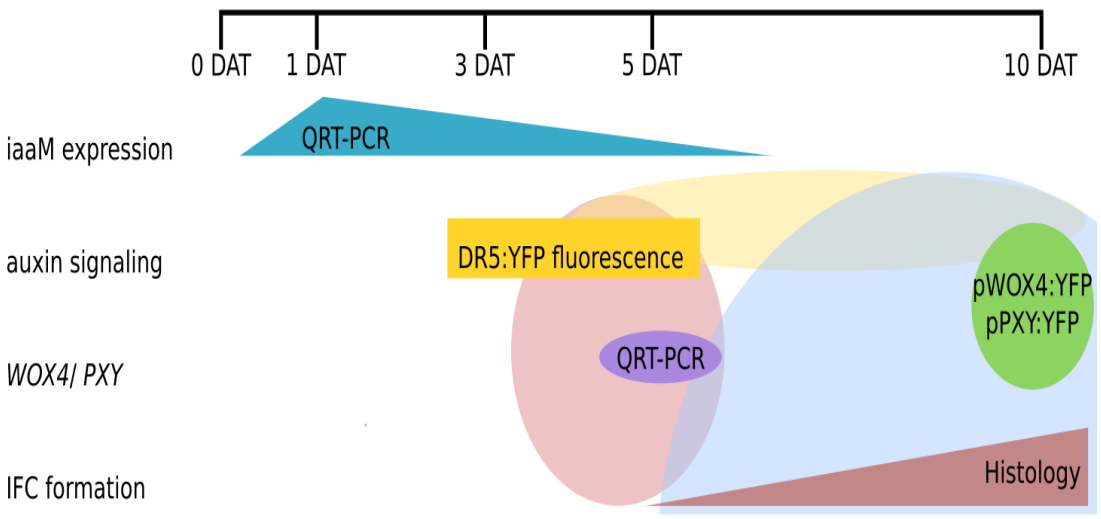

Figure 36 ***Experimental results and hypothetical sequence of developmental steps that lead to secondary growth****. Experimental results are: the schematic expression profile of iaaM tested by qRT-PCR (turquoise triangle), the stable YFP signal intensity under auxin responsive DR5 promotor at 3DAT and 5DAT (yellow square), WOX4 and PXY expression tested by qRT-PCR at 5 DAT and pWOX4:YFP and pPXY:YFP marker analysis performed 10 DAT, IC formation shown in histological analysis 5 DAT and 10 DAT. The hypothetical sequence of developmental steps consists of: de-differentiation (light red circle), maintenance of stemness and proliferation of cambium cells (light yellow oval), differentiation of vascular tissues and secondary growth (light blue circle).*

4.1.2. Nuclear auxin signaling is important during interfascicular cambium formation

Nuclear auxin signaling is dependent on TRANSPORT INHIBITOR RESPONSE1 (TIR1) (Gray et al., 2001; Tan et al., 2007) and other receptors. Once TIR1 is activated, it initiates degradation of AUX/IAA proteins (Figure 2). Using a stabilized version of the AUX/IAA protein IAA12 also known as BODENLOS (BDL) makes it possible to block nuclear auxin signaling. In this study the stabilized version of BDL (*bdl*) was expressed in an ethanol inducible manner in the starch sheath in parallel to *iaaM* or alone, to study the effect of enhanced auxin biosynthesis while blocking nuclear auxin signaling. The results in figure 14 show, that length of the *iaaM* induced cell files is significantly reduced (around 20%) in the line expressing *bdl* in parallel to *iaaM* when compared with the line with exclusive *iaaM* expression. Taking the formation of cell files as a result of cambium proliferation and differentiation, it can be stated, that nuclear auxin signaling is involved in IC formation. This is supported by earlier results from our lab, expressing *bdl* inducible under the control of the cambium-specific PXY

promotor, resulting as well in a reduction of 20 – 40 % of cambium derived tissue at the base of the stem (Brackmann et al., 2018). As in this study *bdl* was expressed under the control of the SCARECROW promotor only, nuclear auxin signaling was exclusively blocked in starch sheath cells. Auxin signaling was found to have spread towards the xylem at 3 DAT and 5 DAT but was never present in the interfascicular region in the control situation (Figure 15). Hence, auxin could still affect neighboring cells of the starch sheath as its signaling was not blocked there. It has been shown, that IAA proteins form complexes with AUXIN RESPONSIVE FACTORS (ARFs) transcription factors and that those pairs are specific for the developmental state and their expression pattern (Weijers et al., 2005). BDL (IAA12) binds to ARF5 (MONOPTEROS – MP) and can inhibit thereby ARF5 mediated embryo patterning (Hamann et al., 2002) and possibly other ARF5 mediated developmental processes. It was further demonstrated that BDL does not bind other ARFs like ARF7 or ARF19 (Weijers et al., 2005). So it is possible, that auxin can still fulfill its signaling function through other ARFs. In the RNA sequencing dataset (figure number), analyzing differentially expressed genes 5 DAT and comparing ethanol treated wild type against ethanol treated transgenic line with induced auxin biosynthesis in the starch sheath, ARF19 can be found upregulated. In the tissue-specific transcriptome of Arabidopsis thaliana inflorescence stem, ARF19 can be found to be expressed in starch sheath cells (Shi et al., 2020). I hypothesize that auxin still induces de-differentiation through ARF19. ARF19 overlaps in its functions with ARF7, so it cannot be excluded that also ARF 7 is important in this context (Okushima et al., 2005) even though there is no indication for this, as ARF7 is not significantly differential expressed in my RNA dataset. To test the hypothesis, that nuclear auxin signaling via ARF19 is important during IC formation, histological analysis of the transgenic line expressing *iaaM* in the starch sheath in an ethanol inducible manner should be performed in the arf7 arf19 double mutant background.

4.2. Cell wall remodeling in the starch sheath affect interfascicular cambium formation

One big aim of this study was to characterize the role of the cell wall in the formation of the IC. My questions were how does the cell wall change during IC formation and can IC formation be controlled by the cell wall?

4.2.1. Acidification of the starch sheath is not sufficient to induce IC formation but has an additive effect on cell file formation

It is known that auxin causes cell wall acidification within minutes or hours and, furthermore, that acidification is sufficient to induce growth, which is thereby named “acid growth” (Fendrych et al., 2016; Rayle and Cleland, 1992; Takahashi et al., 2012). In most cases, this growth is related to weakening of the plant cell wall and a subsequent turgor-driven expansion of the cell (Cosgrove, 2000; Durachko and Cosgrove, 2009; Majda and Robert, 2018). The developmental step of differentiation can be triggered by acidification of the cell wall, as it was shown in a study about the influence of cell wall acidification on root length (Barbez et al., 2017; Chen et al., 2017) and root meristem size (Pacifici et al., 2018). Because acidification of the cell wall is an important step during growth and other developmental processes and it can be induced by auxin, I was interested in the role of cell wall acidification during IC formation. Data obtained by quantitative realt-time PCR revealed an increase of *SAUR19* expression after *iaaM* induction which peaked 1 DAT (figure number). SAUR19 is known to have an activating effect on the plasmamembrane-localized H^+-ATPases via inhibition of the PP2C-D phosphatase (Spartz et al., 2014). Thus, the increase of *SAUR19* expression can be taken as a hint for cell wall acidification. It is noteworthy, that ARF19 was shown to mediate auxin induced *SAUR19* expression during gravitropic response of the hypocotyl (Wang et al., 2020). This could explain earlier observations made in this study, which are that bdl has a negative effect on IC formation but cannot completely block auxin signaling potentially downstream of ARF19. As ARF19 cannot be blocked by *bdl* it could still mediate the auxin induced cell wall acidification even though other auxin signaling is partially blocked by bdl. Therefore, it would be interesting to determine the pH of the cell wall in the lines expressing *iaaM* and *bdl*

together. Acidification of the cell wall after *iaaM* expression was determined with a pH-sensitive, ratiometric marker. Already 12 hours after induction of the auxin biosynthesis gene *iaaM* by ethanol treatment a significant drop of cell wall pH was determined in the endodermis of the root (Figure 18). The temporal correlation of *SAUR19* induction and the acidification of the cell wall in the endodermis root can be taken as a strong hint for auxin induced cell wall acidification very early after ethanol induced *iaaM* expression.

To investigate the role of cell wall acidification during IC formation a hyperactive version of H^+ATPase ($AHA1^{\Delta 94}$) was expressed in an ethanol-inducible manner under the control of the starch sheath-specific *SCARECROW* promotor. The determination of the pH of the cell wall with the pH sensitive, ratiometric pH sensor revealed an acidification of the cell wall upon ethanol induction of $AHA1^{\Delta 94}$ expression in the root endodermis in the same range caused by *iaaM* induction. Based on my observations I concluded, that expression of $AHA1^{\Delta 94}$ leads to cell wall acidification 12 hours after induction. Histological analysis showed that cell wall acidification of starch sheath cells had no effect on IC formation at 10 DAT because no cell file formation in the interfascicular region was observed (Figure 19). Interestingly, combined expression of $AHA1^{\Delta 94}$ and *iaaM* resulted in a bigger proportion of plants with cell files in the interfascicular region in the second internode 5 DAT (Figure 19). Only 14 % of the induced plants expressing *iaaM* in starch sheath cells showed cell files 5 DAT, whereas 57 % of induced plants expressing *iaaM* and $AHA1^{\Delta 94}$ in parallel showed cell files in the interfascicular region 5 DAT. From those experimental results it can be concluded, that acidification is not sufficient to initiate de-differentiation but once *de novo* formed cambium is present acidification of the cell wall of starch sheath cells can promote cambium proliferation or differentiation. It would be interesting to investigate whether acidification is essential for cambium proliferation and differentiation by blocking the H^+ATPase during auxin induced IC formation.

4.2.2. Pectin modifications of cell walls in the starch sheath are important during interfascicular cambium formation

Pectin as one of the most abundant cell wall components was part of studies about cell wall remodeling during developmental processes in the past (Altartouri et al., 2019; His et al., 2001; Peaucelle et al., 2008, 2011; Wolf et al., 2009). The homogalacturonan backbone of pectin is synthesised in the Golgi apparatus and methyl-esterified before secreted into the apoplast (Wolf et al., 2009). During development and cell wall modification, pectin can be de-methyl esterified by 'pectin methyl esterases' (PMEs), which can be blocked by their inhibitors 'pectin methyl esterase inhibitors' (PMEIs) by complex formation (Paynel et al., 2014). The precise mode of action on homogalacturonan remains still unclear and seems to be dependent on multiple factors like the pH of the cell wall and the degree of methyl esterification of the homogalacturonan (Wolf et al., 2009). To investigate modifications of pectin during IC formation an immunohisto-chemical approach was used. The analysis of cross sections incubated with primary antibodies raised against highly methyl esterified pectin (LM20) and de-methyl esterified, calcified pectin (2F4) revealed a higher amount of de-methyl esterified pectin under the influence of *iaaM* expression in starch sheath cells (Figure 22). This effect is consistent with the effect of auxin-induced de-methyl esterification found in the shoot apical meristem after IAA application (Braybrook and Peaucelle, 2013). Auxin has a positive effect on *PME* expression (Laskowski et al., 2006) and the acidic pH that results from auxin can affect PME activity (Hocq et al., 2017). In my RNA sequencing dataset two *PMEs* were found to be upregulated (*PME61* and *PME31*) but two others were downregulated (*PME44* and *PME1*) five days after ethanol induction of *iaaM* expression. Among the PMEIs that were found to be differentially expressed, ten were downregulated and three were upregulated after *iaaM* induction. Therefore, auxin showed an effect on the transcript levels of *PMEs* and *PMEIs* but a coherent picture cannot be drawn from the data available (Figure 23). It has been shown, that pectin has different modifications depending on organ, developmental stage and tissue (Denès et al., 2000; Hall et al., 2013) and the target specificity of certain pectin remodeling enzymes plays a role in the mode of action (Hothorn et al., 2004). But also the

expression profile of certain genes of pectin modifying enzymes is dependent on tissue and developmental stage (Klepikova et al., 2016). To better understand the auxin-dependent PME induction in the starch sheath during IC formation, sequencing data on single cell level would be necessary. As we have quite some experience with combining genetically encoded fluorescent reporters driven by tissue-specific promoters and fluorescence-activated nuclei sorting (FANS) (Shi et al., 2020), this technique could be used to obtain the expression profile of starch sheath cells during IC formation and more specific PME regulation during this process.

Taking the de-methyl esterification as a read out of higher abundance or/and higher PME activity it was interesting to analyse the effect of pure de-methyl esterification by PME expression on IC formation. Therefore, I created lines to induce *PME3* expression in an ethanol-inducible manner under the control of the *SCR* promotor alone or simultaneously with *iaaM*. I performed histological analysis on cross section of the second internode, harvested 10 DAT and could not find any effect of *PME3* on IC formation (Figure 25). *PME3* expression in the starch sheath was not able to induce de-differentiation and cambium formation. Also in combination with *iaaM*, *PME3* expression showed no additive effect on IC formation or cambium differentiation. As I did not test whether changes in pectin methyl-esterification were induced in this line, I cannot conclude whether PME3 was active in the starch sheath and non-existing PME3 activity could explain the missing histological effect. The lacking activity could be caused by a suboptimal pH for enzymatic activity (Denès et al., 2000; Hocq et al., 2017) or PME3 was not able to fulfill its function because of a suboptimal pattern/degree of methyl-esterification of the pectin. It is also known, that the pH influences the binding affinity of PMEs to their inhibitors (Hocq et al., 2017).

In a next approach, I tested whether it is possible to inhibit auxin-induced IC formation by inhibiting the de-methyl esterification of pectin by expressing *PMEI*s in parallel to *iaaM*. Histological analysis of cross sections of plants expressing *PMEI3* and *iaaM* or *PMEI5* and *iaaM* revealed a strong effects of both PMEIs on IC formation (Figure 26). Expressing *PMEI5* in parallel to *iaaM* caused swelling of cells in the whole cortex already 5 DAT, which is remarkable because *PMEI5* was only expressed in the starch sheath. It was shown, that blocking de-

methyl esterification (by *PMEI* expression) can affect the localization of the auxin transporter PIN1 (Braybrook and Peaucelle, 2013). Altered auxin distribution by blocked de-methyl esterification (by *PMEI5* expression) could therefore be the reason for swollen cells in the cortex, possibly as a result of higher auxin concentration in the cortex. It has been shown that auxin affects CMF alignment and cellulose biosynthesis (Lehman and Sanguinet, 2019). It would be interesting to check the pattern of auxin signaling in those lines to prove the change in auxin distribution by blocked de-methyl esterification. It has been shown recently, that the expression of pectin remodeling enzymes such as PMEs or PMEIs affects the anisotropy of pectin methyl esterification and thereby the anisotropy of cell wall mechanics (Bou Daher et al., 2018; Peaucelle et al., 2015). This alteration of pectin biochemistry can modulate the effect of microtubule-derived cell swelling and isotropy (Bou Daher et al., 2018) and could be a possible explanation for the cell swelling that was observed in this study after *PMEI5* expression. Expressing *PMEI5* in addition to *iaaM* in starch sheath cells also showed a slightly positive effect on IC formation, by an increased cell file length, but there was no obvious earlier onset of cell file formation compared to the line with only *iaaM* expression. Interestingly, expression of *PMEI3* in parallel to *iaaM* had a negative effect on IC formation. Even at 10 DAT only one out of seven cross sections showed cell file formation, indicating that PMEI3 in the starch sheath can block auxin induced de-differentiation (Figure 26). It would be interesting to investigate the effect of *PMEI3* expression in the starch sheath on IC formation in the natural situation at the base of the plant, to analyze whether PMEI3 can suppress secondary growth also there. It has been shown that over-expression of *PMEI3* can suppress auxin-induced organ formation in the shoot apical meristem (Braybrook and Peaucelle, 2013). Furthermore, the expression of *PMEI3* disrupted native pectin anisotropy (distribution of methyl esterified and de-methyl esterified pectin in the cell wall depending on the position within the cell wall) and affected cell elongation in the hypocotyl (Bou Daher et al., 2018). Overexpression of *PMEI3* led to stiffening of the cell wall in the shoot apical meristem (Peaucelle et al., 2011) and in epidermal cell walls in the hypocotyl (Peaucelle et al., 2015). Different scenarios can by hypothesized to explain the inhibitory effect on IC formation. PMEI3 possibly prevents

de-methyl esterification and subsequent lysis of pectin. Thereby, the accessibility of other cell wall components would be limited and secondary cell wall remodeling enzymes could be hindered in their action.

It has been shown that changes in the mechanical forces can influence secondary growth (Ko et al., 2004). The possible change in cell wall mechanics, that was potentially induced by auxin-dependent de-methyl esterification could be an important signal for the plant to initiate IC. If this starting shot is missing because the change is hindered by the expression and action of the inhibitor of PME, initiation of IC formation possibly fails.

The receptor-like protein RLP44 could be a possible mediator for this signal, as it is known that it senses pectin modification and is involved in controlling vascular cell fate in the root by activating brassinosteroid signaling (Holzwart et al., 2018; Wolf et al., 2014).

4.3. Enhanced auxin biosynthesis has a major impact on transcriptional regulation – especially of cell wall related genes

Enhanced auxin biosynthesis and nuclear auxin signaling is important for interfascicular cambium formation as my extensive histological analyses have shown. Histological analysis showed major changes at 10 DAT but increased auxin signaling was already demonstrated to occur at 3 DAT as well as a change in transcriptional regulation of cambium-specific genes like WOX4 and PXY at 5 DAT. To identity bridging elements between the early event of auxin signaling and the late event of cell file formation I performed genome-wide mRNA sequencing.

Auxin is an important plant hormone that is able to control a lot of processes like tropic responses to light and gravity, general root and shoot architecture, organ patterning, vascular development and growth. The versatility of auxin explains the large number of genes that are differentially expressed comparing the ethanol-treated wild type with the ethanol-treated transgenic line with enhanced auxin biosynthesis in the starch sheath. Interestingly, not only expected auxin signaling-related genes and genes correlated with the cambium were differentially

expressed but also, and especially, cell wall-related genes encoding for proteins holding catalytic activity (i.e. enzymes, Figure 23 D). This finding indicates auxin-induced cell wall remodeling even bevor changes on the histological level is detectable. Among the cell wall-related genes that are differentially expressed there are PMEs, extensins, expansins, cellulose synthases and xyloglucans.

To get an idea about the downstream processes and regulatory networks involved in cell wall modification, I compared the RNA-seq data set which I obtained when inducing secondary growth by enhancing auxin biosynthesis with an RNA-seq data-set obtained by comparing the *rlp44* mutant with wild type plants. This comparison is particular interesting because RLP44 was found to sense and communicate cell wall modifications especially in the pectin matrix in a brassinosteroid signaling-dependent manner (Wolf et al., 2014). When I compared both data sets, three groups of genes caught my attention. The first two groups were genes encoding for extensins and genes encoding for xyloglucans. These genes were differentially expressed exclusively upon enhanced auxin biosynthesis in the starch sheath. The third group were cellulose synthases genes which I found in both comparisons (Figure 24 D). The transcriptional upregulation of extensins recapitulates what was found in the immunohistochemistry experiments (Figure 21), where the abundance of extensins was increased 10 DAT in the induced *pSCR>>iaaM* line. As extensins are not differentially regulated in the *rlp44* mutant, it can be suggested that their expression is not dependent on RLP44 but purely a response to an auxin-induced cell wall modification. Similarly, the xyloglucan genes can only be found to be differentially expressed upon enhanced auxin biosynthesis, with some genes up- and with some downregulated. So, the picture is not very conclusive in this case. The function of xyloglucans in general is the interaction with CMFs, lowering their crystallinity and potentially increasing the resilience to strain (Xiao et al., 2016). The differential expression of xyloglucans (no matter whether down- or up-regulated) could, therefore, be taken as an indicator for an RLP44-independent change in cellulose crystallinity.

Interestingly, the differentially expressed cellulose synthase genes were found in both data sets. This suggests that the regulation of cellulose biosynthesis depends not only on auxin but also on RLP44. This is

particularly interesting because it has been shown by Jiyan Qi and Stephanie Werner (Greb lab) that in the *rlp44* mutant secondary growth is increased (data not published). Also it is known that brassinosteroids can regulate cellulose biosynthesis by controlling the expression of CESA genes in Arabidopsis (Xie et al., 2011). Considering that, it would be interesting to further investigate the role of RLP44 and the importance of brassinosteroid signaling in secondary growth and to observe the effect of enhanced auxin biosynthesis in the starch sheath in an *rlp44* mutant background.

4.4. Brillouin microscopy can determine mechanical properties of plant cell walls in different tissues

During the period of this study I constructed a home-built Brillouin microscope and established the technique of Brillouin microscopy in the lab in a collaborative effort. Main parts were chosen and assembled in Vienna by our cooperation partner Kareem Elsayad and afterwards shipped to Heidelberg. It consisted out of the laser source with an isolator, a beam expander and a 90:10 beam splitter, a narrow bandpass filter and the microscope body. The signal was directed freely into the 2 VIPA spectrometer with a cMOS camera. Unfortunately, the system was not functional and to overcome potential sources of error and to make the system more stable and more applicable to our purposes I changed and added some components. After the laser source with the isolator I added a collimator and a single mode fiber, to clean the illumination beam and gain a purely Gaussian beam profile. Furthermore, I could chose the beam diameter by the choice of the output collimator to make it more convenient to guide the beam through the system without clipping off the beam. I exchanged the non-polarizing beam splitter (90:10) to a polarizing beam splitter which gives me flexibility in choosing the power at the sample and does not cut of 90 % of the signal intensity automatically. I optimized the beam diameter of the illumination beam so that is slightly overfill the back aperture of the microscope objective, which optimize the illumination of the sample, and lower the loss (Figure 27). To guide the signal from the sample into the spectrometer I choose a single mode fiber instead of guiding it freely into the spectrometer. That fulfills two functions at the same time, it acts as a pinhole and ensure confocality of the system and it makes it more robust against

small changes, because illumination part and spectrometer part are separated. At last I built in a Lyot stop filter to enhance the spectral contrast, which is essential in non-transparent, turbid samples like plants (Figure 28). Dmitry Richter helped me to re-assemble the spectrometer after putting in the Lyot stop filter and wrote the software to analyze the signal. And we were able to gain the first Brillouin spectrum of water (Figure 30).

To test whether the system delivers trustable results I first tested glycerol aqueous solutions and agarose gels with known mechanical properties to compare results with knowledge from the literature. For both experiments increasing Brillouin shift with increasing concentration of either glycerol or agarose was correlated with increasing longitudinal elasticity modulus (Figure 31). This concentration-dependent behavior was found in the past as well (Adichtchev et al., 2019; Normand et al., 2000; Slie et al., 1966) and can be taken as a proof for a well working set up. Because this method was applied to determine mechanical properties and their changes in plant cell walls I also tested a hydrogel that consisted of the cell wall polymers cellulose and callose and was tested regarding its mechanical properties via AFM earlier (Abou-Saleh et al., 2018). A drop of Brillouin shift caused by higher amount of callose in the hydrogel was observed, that can be interpreted as a decrease in the longitudinal elasticity modulus (Figure 32). The same behavior of the Youngs modulus was observed with AFM (Abou-Saleh et al., 2018). Callose and cellulose interact with each other and callose has a negative impact on cellulose crystallinity (Abou-Saleh et al., 2018) and anisotropy, which can affect the Brillouin shift (Webb et al., 2020). It has been shown that the Brillouin shift is the smallest if the light hits the material perpendicular to the major fiber orientation. Interestingly the pure callose did not have the lowest longitudinal elasticity modulus (which would follow the trend and the described Youngs modulus) and showed indeed the highest Brillouin shift in my analyses, indicating a big longitudinal elasticity modulus. Thus, pure callose behaved more according to its predicted function of stiffening the cell wall. This could explain the high Youngs modulus in tissues with high callose content that was detected earlier (Parre and Geitmann, 2005; Vogler et al., 2013). Another way to explain the results is the aging of the pure callose hydrogel. It has been described earlier, that hydrogels from β(1-3),(1-6)-

D-glucan stiffen if they are stored over a long time (Blahovec et al., 2011). It seems that callose can have a “softening” effect on cellulose, that potentially increases the resilience of cellulose to strain. Pure callose seems to be “stiffer” than crystalline cellulose and mixtures of crystalline cellulose with callose and can thereby increase the elasticity modulus of the cell wall.

4.4.1. Mechanics of the cell wall in roots depends on orientation and localization

After testing the system with materials closely related to cell wall and the proof that it can deliver reliable and comprehensible results, I used the Brillouin microscope to determine mechanical properties of cell walls in different developmental zones of the root. The results show very different properties of the cell wall depending on the position of the cell (Figure 33) but also on the orientation of the cell wall (figure number). Interestingly, the meristematic zone with cells of high mitotic activity and thin cell walls (Baluska et al., 1996) appear as the zone with the most prominent Brillouin shift indicating the largest longitudinal elasticity modulus. This could be explained by the high content of callose in the newly formed cell plate of freshly divided cells (De Cnodder et al., 2007). Interestingly, the values of the Brillouin shift of the meristematic zone in roots matches quiet well with values of the Brillouin shift of pure callose (Figure 32). In the maturating cell wall the callose is replaced by cellulose, which is first randomly oriented and start to align transversely in the elongation zone (Anderson et al., 2010; Sugimoto et al., 2000).

The elongation and differentiation zone show a decreased Brillouin shift in comparison to the meristematic zone (Figure 33) which suggests a lower elasticity modulus in those zones. This can be reasoned by the absence of callose (De Cnodder et al., 2007), that had been replaced by highly oriented CMFs. Additional cell wall remodeling and loosening allows turgor-driven cell elongation in the elongation zone. Cell wall remodeling enzymes like expansins or XYLOGLUCAN ENDOTRANSGLUCOSYLASE/HYDROLASEs (XTHs) are activated and/or expressed in the elongation and differentiation zone of the root, changing the interaction between CMFs and xyloglucan and finally cause cell wall softening (Cosgrove, 2005; McQueen-Mason et al.,

1992). The softer cell walls allow cell elongation in the elongation zone and processes like lateral root emergence in the differentiation zone (Péret et al., 2012; Swarup et al., 2008). Brillouin shifts of the longitudinal cell walls are not different from transversal cell walls in the differentiation zone. The transversal cell walls in the elongation zone show an increased Brillouin shift compared to the longitudinal cell wall in the differentiation zone, indicating a larger longitudinal elasticity modulus. Those results confirm findings about the Young's modulus, which was higher in transversal cell walls and lower in longitudinal cell walls of the hypocotyl (Bou Daher et al., 2018; Peaucelle et al., 2015) but stand in contrast to Brillouin shifts that were found to be smaller in transversal cell walls and bigger in longitudinal cell walls of the hypocotyl (Elsayad et al., 2016). In the same study, no differences in longitudinal and transversal cell walls was found in roots, like in my case for cell walls of the differentiation zone. Possible reasons for different results can be found in differences in growth conditions and age of the seedlings used or the exact position of the measurements as the cell wall along the root is very heterogenic in its composition. In conclusion it can be said, that Brillouin microscopy is an appropriate method to determine mechanical properties in plants on a subcellular level. The spectral resolution of the set-up is sufficient to differ mechanical properties in cell walls of different tissues and cell types. For the interpretation of the results it is necessary to take into account, that cell composition and CMF orientation, that are influencing the properties of the cell wall in accordance to the demands, also effect the elasticity modulus.

4.4.2. Cell wall mutants impaired in root elongation show differences in the elasticity modulus of the cell wall

As it was discussed earlier (5.3.1.), two main aspects are important for cell elongation in the root, the orientation of CMFs perpendicular to the growth axis and activity and expression of cell wall remodeling enzymes. To test whether plants with impaired root elongation show an altered Brillouin shift of the cell wall I chose certain cell wall mutants. Those mutants were affected in a cellulose synthase (ANISOTROPY1 – ANY1) and an endo-1,4-β-glucanase important for cellulose synthesis and the trafficking of cellulose synthases complexes (KORRIGAN1 – KOR1)

(Fujita et al., 2013; His et al., 2001; Vain et al., 2014). In former studies, *any1* showed CMFs in roots and dark grown hypocotyl in a transversal orientation like in the wild type situation, but those were found to be misaligned in the epidermis of the stem. The overall cellulose content was not altered but the cellulose crystallinity and the velocity of the cellulose synthase complex was reduced (Fujita et al., 2013). In pavement cells and in the shoot apical meristem it was found that *any1* mutants have a reduced longitudinal elasticity modulus (Altartouri et al., 2019) (Sampathkumar et al., 2019). For *kor1-3* mutants it was shown, that the cellulose content is reduced as well as the velocity of the cellulose synthase complex and the crystallinity of cellulose. Even though the endo-1,4-β-glucanase has no direct influence on pectin, the *kor1-3* mutant showed altered pectin composition with a higher probability for cross linking (His et al., 2001; Vain et al., 2014). My investigation of cell walls of cells in the root elongation zone of the cell wall mutants, revealed a stiffening of the cell wall in the *kor1-3* mutant in transversal and longitudinal cell walls, whereas cell walls of the *any1* mutant showed Brillouin shifts comparable to those detected in the wild type (Figure 34). The unchanged elasticity modulus of the *any1* mutants comes with a surprise because it was shown that the Young's modulus and longitudinal elasticity modulus are reduced in pavement cells and the shoot apical meristem in this mutant (Altartouri et al., 2019; Sampathkumar et al., 2019). Those studies were restricted to cell walls at the epidermis, were this mutant also showed an impaired CMF orientation in comparison to the wild type. It can be hypothesized that the CESA1 is especially important in the epidermis and so the *any1* mutation affects mostly cell wall mechanics in the epidermal cells. In the present study longitudinal cell walls of all different cell layers were analyzed what maybe lead to a dilution of the *any1*-caused changes in cell wall mechanics. In this way it could still restrict elongation of the root and cause the dwarf phenotype, while cells in the sub-epidermal layers staying mostly unaffected. A cell specific localization of CESA1 would be helpful to discuss this result in more detail. The *kor1-3* mutant showed larger Brillouin shifts in longitudinal and transversal cell walls, the ratio between Brillouin shifts of both regions was slightly smaller than in the wild type indicating a larger difference between longitudinal and transversal cell walls. The indicated stiffening of the cell wall could be

reasoned by pectin cross linking, which is known to have a stiffening effect on the cell wall. It would be necessary to show the abundance of calcified pectate with the help of the specific antibody to verify this hypothesis.

4.4.3. The shoot apical meristem reacts below the surface on isoxaben treatment

The shoot apical meristem (SAM) is the source of most aerial parts of the plant and is a dome like structure build up by cell layers of different cell wall properties (Peaucelle et al., 2008, 2011; Sampathkumar et al., 2019). It was found, that the alignment of cortical microtubules is regulated by physical stress during SAM development (Peaucelle et al., 2008). Microtubules direct the deposition of CMFs, the load barring component in the cell wall, which affect morphological events like leaf and flower initiation (Sassi et al., 2014). CMFs were found to have a different degree of alignment depending on the cell layer of the SAM (Sampathkumar et al., 2019). In this study I used isoxaben, an inhibitor of cellulose synthesis to study its effect on the elasticity modulus of the SAM. It was found that the disruption of cellulose synthesis results in a decrease of the Young's modulus of the SAM, determined with AFM (Sampathkumar et al., 2019). I could repeat this effect on the longitudinal elasticity modulus, determined by Brillouin microscopy (Figure 35). Interestingly, different cell layers reacted differently to the treatments and also showed a difference in their basal properties. While the second cell layer showed Brillouin shifts around 7.87 GHz in the control group of SAMs, the 4^{th} cell layer showed significantly larger Brillouin shifts of around 7.93 GHz and the 8^{th} cell layer showed a decreased Brillouin shift of around 7.85 GHz. The isoxaben treatment showed a significant reduction of the Brillouin shift only in the 4^{th} cell layer, there the Brillouin shift dropped down to 7.905 GHz. This difference was not detectable in the AFM measurements and provide new insights in the elasticity of the SAM depending on the cell layer. Those differences can be explained by the difference in cell wall composition of different cell layers, that was detected earlier (Peaucelle et al., 2008), but also the orientation of the CMFs can affect the measured Brillouin shift. It only has been shown

recently that fiber orientation and their angle regarding the incident light of the Brillouin microscope set up can have a grave impact on the longitudinal modulus detected by Brillouin microscopy (Webb et al., 2020), because the longitudinal elasticity modulus is determined by fiber orientation. It is of eminent importance to keep this in mind when interpreting results.

5. Conclusion

This study underlines the importance of auxin for IC formation and secondary growth in plants. I have extensively investigated the process of a major cell fate change in a differentiated organ and was able to show how important local nuclear auxin signaling is for the processes of cambium proliferation and differentiation. The fundamental process of de-differentiation prior to proliferation and differentiation can still be realized even though parts of the nuclear auxin signaling are suppressed, which enables us to narrow down possible downstream targets of nuclear auxin signaling. I determined genome-wide changes of gene expression upon the auxin induced initialization of IC formation. Furthermore, indications have been found that auxin induces cell wall acidification. Even though, cell wall acidification itself is not sufficient to induce IC formation, it showed a positive effect on IC formation. Intriguingly, auxin induced IC formation could be blocked by counteracting the pectin modifications that were induced by auxin. It can be concluded, that different aspects of auxin-dependent changes in cell fate like acidification, nuclear signaling and cell wall modification are all contributing to IC formation.

Furthermore, I have helped to establish a method to determine mechanical properties in planta. I have shown, that Brillouin microscopy is a valid method to detect changes in mechanical properties on sub-cellular structures like the plant cell wall in different parts of the plant. I was able to determine changes in Brillouin shift depending on orientation but also on the localization of the cell walls. This new method enables us to ask new questions and find possible answers on the impact of mechanical properties of the extracellular matrix on developmental processes in plants.

6. List of Publications

Co-Authorship

Brackmann, K., Qi, J., Gebert, M., Jouannet, V., Schlamp, T., Grünwald, K., Wallner, E.-S., *No*vikova, D.D., Levitsky, V.G., Agustí, J., et al. (2018). Spatial specificity of auxin responses coordinates wood formation. Nat. Commun. *9*, 875.

López-Salmerón V, Schuerholz A-K, Li Z, Schlamp T, Wenzl C, Lohmann JU, Greb T, Wolf S (2019) Inducible, cell type-specific expression in Arabidopsis thaliana through LhGR-mediated trans-activation. J Vis Exp 146:e59394.

7. Index of Figures

Index of Figures

8. Bibliography

Abou-Saleh, R.H., Hernandez-Gomez, M.C., Amsbury, S., Paniagua, C., Bourdon, M., Miyashima, S., Helariutta, Y., Fuller, M., Budtova, T., Connell, S.D., et al. (2018). Interactions between callose and cellulose revealed through the analysis of biopolymer mixtures. Nat. Commun. *9*, 4538.

Adamowski, M., Li, L., and Friml, J. (2019). Reorientation of Cortical Microtubule Arrays in the Hypocotyl of Arabidopsis thaliana Is Induced by the Cell Growth Process and Independent of Auxin Signaling. Int. J. Mol. Sci. 20.

Adichtchev, S.V., Karpegina, Y.A., Okotrub, K.A., Surovtseva, M.A., Zykova, V.A., and Surovtsev, N.V. (2019). Brillouin spectroscopy of biorelevant fluids in relation to viscosity and solute concentration. Phys. Rev. E 99, 062410.

Agusti, J., and Greb, T. (2013). Going with the wind--adaptive dynamics of plant secondary meristems. Mech. Dev. 130, 34–44.

Agusti, J., Herold, S., Schwarz, M., Sanchez, P., Ljung, K., Dun, E.A., Brewer, P.B., Beveridge, C.A., Sieberer, T., Sehr, E.M., et al. (2011a). Strigolactone signaling is required for auxin-dependent stimulation of secondary growth in plants. Proc. Natl. Acad. Sci. USA 108, 20242–20247.

Agusti, J., Lichtenberger, R., Schwarz, M., Nehlin, L., and Greb, T. (2011b). Characterization of transcriptome remodeling during cambium formation identifies MOL1 and RUL1 as opposing regulators of secondary growth. PLoS Genet. 7, e1001312.

Altamura, M.M., Possenti, M., Matteucci, A., Baima, S., Ruberti, I., and Morelli, G. (2001). Development of the vascular system in the inflorescence stem of Arabidopsis. New Phytol. 151, 381–389.

Altartouri, B., Bidhendi, A.J., Tani, T., Suzuki, J., Conrad, C., Chebli, Y., Liu, N., Karunakaran, C., Scarcelli, G., and Geitmann, A. (2019). Pectin chemistry and cellulose crystallinity govern pavement cell morphogenesis in a multi-step mechanism. Plant Physiol. 181, 127–141.

Anderson, C.T., Carroll, A., Akhmetova, L., and Somerville, C. (2010). Real-time imaging of cellulose reorientation during cell wall expansion in Arabidopsis roots. Plant Physiol. 152, 787–796.

Antonacci, G., Foreman, M.R., Paterson, C., and Török, P. (2013). Spectral broadening in Brillouin imaging. Appl. Phys. Lett. 103, 221105.

Antonacci, G., Beck, T., Bilenca, A., Czarske, J., Elsayad, K., Guck, J., Kim, K., Krug, B., Palombo, F., Prevedel, R., et al. (2020). Recent progress and current opinions in Brillouin microscopy for life science applications. Biophys. Rev. 12, 615–624.

Aryal, B., Jonsson, K., Baral, A., Sancho-Andres, G., Routier-Kierzkowska, A.-L., Kierzkowski, D., and Bhalerao, R.P. (2020). Interplay between cell wall and auxin mediates the control of differential cell elongation during apical hook development. Curr. Biol. 30, 1733–1739.e3.

Axelsen, K.B., Venema, K., Jahn, T., Baunsgaard, L., and Palmgren, M.G. (1999). Molecular dissection of the C-terminal regulatory domain of the plant plasma

membrane H+-ATPase AHA2: mapping of residues that when altered give rise to an activated enzyme. Biochemistry 38, 7227–7234.

Baluska, F., Volkmann, D., and Barlow, P.W. (1996). Specialized zones of development in roots:' ' view from the cellular level. Plant Physiol. 112, 3–4.

Barbez, E., Dünser, K., Gaidora, A., Lendl, T., and Busch, W. (2017). Auxin steers root cell expansion via apoplastic pH regulation in Arabidopsis thaliana. Proc. Natl. Acad. Sci. USA 114, E4884–E4893.

Barra-Jiménez, A., and Ragni, L. (2017). Secondary development in the stem: when Arabidopsis and trees are closer than it seems. Curr. Opin. Plant Biol. 35, 145–151.

Basile, A., Fambrini, M., and Pugliesi, C. (2017). The vascular plants: open system of growth. Dev. Genes Evol. 227, 129–157.

Baskin, T.I. (2005). Anisotropic expansion of the plant cell wall. Annu. Rev. Cell Dev. Biol. 21, 203–222.

Baumberger, N., Ringli, C., and Keller, B. (2001). The chimeric leucine-rich repeat/extensin cell wall protein LRX1 is required for root hair morphogenesis in Arabidopsis thaliana. Genes Dev. 15, 1128–1139.

Beauzamy, L., Louveaux, M., Hamant, O., and Boudaoud, A. (2015). Mechanically, the Shoot Apical Meristem of Arabidopsis Behaves like a Shell Inflated by a Pressure of About 1 MPa. Front. Plant Sci. 6, 1038.

Benková, E., Michniewicz, M., Sauer, M., Teichmann, T., Seifertová, D., Jürgens, G., and Friml, J. (2003). Local, efflux-dependent auxin gradients as a common module for plant organ formation. Cell 115, 591–602.

Blahovec, J., Hejlová, A., Čopíková, J., and Novák, M. (2011). Tensile properties of microbial β-glucan films. Polym. Eng. Sci. 51, 2564–2570.

Bolser, D., Staines, D.M., Pritchard, E., and Kersey, P. (2016). Ensembl Plants: integrating tools for visualizing, mining, and analyzing plant genomics data. Methods Mol. Biol. 1374, 115–140.

Brackmann, K., Qi, J., Gebert, M., Jouannet, V., Schlamp, T., Grünwald, K., Wallner, E.-S., Novikova, D.D., Levitsky, V.G., Agustí, J., et al. (2018). Spatial specificity of auxin responses coordinates wood formation. Nat. Commun. 9, 875.

Braybrook, S.A., and Peaucelle, A. (2013). Mechano-chemical aspects of organ formation in Arabidopsis thaliana: the relationship between auxin and pectin. PLoS One 8, e57813.

Bund, A., and Schwitzgebel, G. (1998). Viscoelastic properties of low-viscosity liquids studied with thickness-shear mode resonators. Anal. Chem. 70, 2584–2588.

Burton, R.A., Gidley, M.J., and Fincher, G.B. (2010). Heterogeneity in the chemistry, structure and function of plant cell walls. Nat. Chem. Biol. 6, 724–732.
Cannon, M.C., Terneus, K., Hall, Q., Tan, L., Wang, Y., Wegenhart, B.L., Chen, L., Lamport, D.T.A., Chen, Y., and Kieliszewski, M.J. (2008). Self-assembly of the plant cell wall requires an extensin scaffold. Proc. Natl. Acad. Sci. USA 105, 2226–2231.

Caño-Delgado, A., Yin, Y., Yu, C., Vafeados, D., Mora-García, S., Cheng, J.-C., Nam, K.H., Li, J., and Chory, J. (2004). BRL1 and BRL3 are novel brassinosteroid receptors that function in vascular differentiation in Arabidopsis. Development 131, 5341–5351.

Carpita, N.C., and Gibeaut, D.M. (1993). Structural models of primary cell walls in flowering plants: consistency of molecular structure with the physical properties of the walls during growth. Plant J. 3, 1–30.

Chan, C.J., Heisenberg, C.-P., and Hiiragi, T. (2017). Coordination of Morphogenesis and Cell-Fate Specification in Development. Curr. Biol. 27, R1024–R1035.

Chen, H., Zhang, Q., Cai, H., and Xu, F. (2017). Ethylene Mediates Alkaline-Induced Rice Growth Inhibition by Negatively Regulating Plasma Membrane H+-ATPase Activity in Roots. Front. Plant Sci. 8, 1839.

Chen, S., Ehrhardt, D.W., and Somerville, C.R. (2010). Mutations of cellulose synthase (CESA1) phosphorylation sites modulate anisotropic cell expansion and bidirectional mobility of cellulose synthase. Proc. Natl. Acad. Sci. USA 107, 17188–17193.

Clough, S.J., and Bent, A.F. (1998). Floral dip: a simplified method for Agrobacterium-mediated transformation of Arabidopsis thaliana. The Plant Journal 16, 735–743.

De Cnodder, T., Verbelen, J.-P., and Vissenberg, K. (2007). The control of cell size and rate of elongation in the arabidopsis root. In The Expanding Cell, J.-P. Verbelen, and K. Vissenberg, eds. (Berlin, Heidelberg: Springer Berlin Heidelberg), pp. 249–269.

Cosgrove, D.J. (2000). Loosening of plant cell walls by expansins. Nature 407, 321–326.

Cosgrove, D.J. (2005). Growth of the plant cell wall. Nat. Rev. Mol. Cell Biol. 6, 850–861.

Bou Daher, F., Chen, Y., Bozorg, B., Clough, J., Jönsson, H., and Braybrook, S.A. (2018). Anisotropic growth is achieved through the additive mechanical effect of material anisotropy and elastic asymmetry. Elife 7.

Daza, R., González-Bermúdez, B., Cruces, J., De la Fuente, M., Plaza, G.R., Arroyo-Hernández, M., Elices, M., Pérez-Rigueiro, J., and Guinea, G.V. (2019). Comparison of cell mechanical measurements provided by Atomic Force Microscopy (AFM) and Micropipette Aspiration (MPA). J Mech Behav Biomed Mater 95, 103–115.

Denès, J.M., Baron, A., Renard, C.M., Péan, C., and Drilleau, J.F. (2000). Different action patterns for apple pectin methylesterase at pH 7.0 and 4.5. Carbohydr. Res. 327, 385–393.

Draeger, C., Ndinyanka Fabrice, T., Gineau, E., Mouille, G., Kuhn, B.M., Moller, I., Abdou, M.-T., Frey, B., Pauly, M., Bacic, A., et al. (2015). Arabidopsis leucine-rich repeat extensin (LRX) proteins modify cell wall composition and influence plant growth. BMC Plant Biol. 15, 155.

Durachko, D.M., and Cosgrove, D.J. (2009). Measuring plant cell wall extension (creep) induced by acidic pH and by alpha-expansin. J. Vis. Exp. 1263.

Eckardt, N.A. (2008). Role of xyloglucan in primary cell walls. Plant Cell 20, 1421–1422.

Ed-Daoui, A., Benelmostafa, M., and Dahmani, M. (2019). Study of the viscoelastic properties of the agarose gel. Materials Today: Proceedings 13, 746–751.

Edrei, E., Gather, M.C., and Scarcelli, G. (2017a). Noise reduction in Brillouin microscopy via spectral coronagraphy. In Frontiers in Optics 2017, (Washington, D.C.: OSA), p. FM4B.2.

Edrei, E., Gather, M.C., and Scarcelli, G. (2017b). Integration of spectral coronagraphy within VIPA-based spectrometers for high extinction Brillouin imaging. Opt. Express 25, 6895–6903.

Elsayad, K., Werner, S., Gallemí, M., Kong, J., Sánchez Guajardo, E.R., Zhang, L., Jaillais, Y., Greb, T., and Belkhadir, Y. (2016). Mapping the subcellular mechanical properties of live cells in tissues with fluorescence emission-Brillouin imaging. Sci. Signal. 9, rs5.

Engler, A.J., Sen, S., Sweeney, H.L., and Discher, D.E. (2006). Matrix elasticity directs stem cell lineage specification. Cell 126, 677–689.

Esmon, C.A., Tinsley, A.G., Ljung, K., Sandberg, G., Hearne, L.B., and Liscum, E. (2006). A gradient of auxin and auxin-dependent transcription precedes tropic growth responses. Proc. Natl. Acad. Sci. USA 103, 236–241.

Etchells, J.P., Provost, C.M., Mishra, L., and Turner, S.R. (2013). WOX4 and WOX14 act downstream of the PXY receptor kinase to regulate plant vascular proliferation independently of any role in vascular organisation. Development 140, 2224–2234.

Fendrych, M., Leung, J., and Friml, J. (2016). TIR1/AFB-Aux/IAA auxin perception mediates rapid cell wall acidification and growth of Arabidopsis hypocotyls. Elife 5.

Fisher, K., and Turner, S. (2007). PXY, a receptor-like kinase essential for maintaining polarity during plant vascular-tissue development. Curr. Biol. 17, 1061–1066.

Friml, J. (2003). Auxin transport — shaping the plant. Curr. Opin. Plant Biol. 6, 7–12.

Friml, J., Wiśniewska, J., Benková, E., Mendgen, K., and Palme, K. (2002). Lateral relocation of auxin efflux regulator PIN3 mediates tropism in Arabidopsis. Nature 415, 806–809.

Fujita, M., Himmelspach, R., Ward, J., Whittington, A., Hasenbein, N., Liu, C., Truong, T.T., Galway, M.E., Mansfield, S.D., Hocart, C.H., et al. (2013). The anisotropy1 D604N mutation in the Arabidopsis cellulose synthase1 catalytic domain reduces cell wall crystallinity and the velocity of cellulose synthase complexes. Plant Physiol. 162, 74–85.

Gaillochet, C., Daum, G., and Lohmann, J.U. (2015). O cell, where art thou? The mechanisms of shoot meristem patterning. Curr. Opin. Plant Biol. 23, 91–97.

Gonzalez-Perez, O., López-Virgen, V., and Ibarra-Castaneda, N. (2018). Permanent Whisker Removal Reduces the Density of c-Fos+ Cells and the Expression of Calbindin Protein, Disrupts Hippocampal Neurogenesis and Affects Spatial-Memory-Related Tasks. Front. Cell Neurosci. 12, 132.

Gray, W.M., Kepinski, S., Rouse, D., Leyser, O., and Estelle, M. (2001). Auxin regulates SCF(TIR1)-dependent degradation of AUX/IAA proteins. Nature 414, 271–276.

Greb, T., and Lohmann, J.U. (2016). Plant Stem Cells. Curr. Biol. 26, R816–21.

Gutierrez, R., Lindeboom, J.J., Paredez, A.R., Emons, A.M.C., and Ehrhardt, D.W. (2009). Arabidopsis cortical microtubules position cellulose synthase delivery to the plasma membrane and interact with cellulose synthase trafficking compartments. Nat. Cell Biol. 11, 797–806.

Hall, H.C., Cheung, J., and Ellis, B.E. (2013). Immunoprofiling reveals unique cell-specific patterns of wall epitopes in the expanding Arabidopsis stem. Plant J. 74, 134–147.

Hamann, T., Benkova, E., Bäurle, I., Kientz, M., and Jürgens, G. (2002). The Arabidopsis BODENLOS gene encodes an auxin response protein inhibiting MONOPTEROS-mediated embryo patterning. Genes Dev. 16, 1610–1615.

Hamant, O., and Traas, J. (2010). The mechanics behind plant development. New Phytol. 185, 369–385.

Han, S., Cho, H., Noh, J., Qi, J., Jung, H.-J., Nam, H., Lee, S., Hwang, D., Greb, T., and Hwang, I. (2018). BIL1-mediated MP phosphorylation integrates PXY and cytokinin signalling in secondary growth. Nat. Plants 4, 605–614.

Hanson, M.R., and Köhler, R.H. (2001). GFP imaging: methodology and application to investigate cellular compartmentation in plants. J. Exp. Bot. 52, 529–539.

Haruta, M., Gray, W.M., and Sussman, M.R. (2015). Regulation of the plasma membrane proton pump (H(+)-ATPase) by phosphorylation. Curr. Opin. Plant Biol. 28, 68–75.

Heisler, M.G., Hamant, O., Krupinski, P., Uyttewaal, M., Ohno, C., Jönsson, H., Traas, J., and Meyerowitz, E.M. (2010). Alignment between PIN1 polarity and microtubule orientation in the shoot apical meristem reveals a tight coupling between morphogenesis and auxin transport. PLoS Biol. 8, e1000516.

His, I., Driouich, A., Nicol, F., Jauneau, A., and Höfte, H. (2001). Altered pectin composition in primary cell walls of korrigan, a dwarf mutant of Arabidopsis deficient in a membrane-bound endo-1,4-beta-glucanase. Planta 212, 348–358.

Hocq, L., Pelloux, J., and Lefebvre, V. (2017). Connecting Homogalacturonan-Type Pectin Remodeling to Acid Growth. Trends Plant Sci. 22, 20–29.

Holzwart, E., Huerta, A.I., Glöckner, N., Garnelo Gómez, B., Wanke, F., Augustin, S., Askani, J.C., Schürholz, A.-K., Harter, K., and Wolf, S. (2018). BRI1 controls vascular cell fate in the Arabidopsis root through RLP44 and phytosulfokine signaling. Proc. Natl. Acad. Sci. USA 115, 11838–11843.

Hothorn, M., Wolf, S., Aloy, P., Greiner, S., and Scheffzek, K. (2004). Structural insights into the target specificity of plant invertase and pectin methylesterase inhibitory proteins. Plant Cell 16, 3437–3447.

Jacobowitz, J.R., Doyle, W.C., and Weng, J.-K. (2019). PRX9 and PRX40 Are Extensin Peroxidases Essential for Maintaining Tapetum and Microspore Cell Wall Integrity during Arabidopsis Anther Development. Plant Cell 31, 848–861.

Kesten, C., Gámez-Arjona, F.M., Menna, A., Scholl, S., Dora, S., Huerta, A.I., Huang, H.-Y., Tintor, N., Kinoshita, T., Rep, M., et al. (2019). Pathogen-induced pH changes regulate the growth-defense balance in plants. EMBO J. 38, e101822.

Kiehart, D.P., Galbraith, C.G., Edwards, K.A., Rickoll, W.L., and Montague, R.A. (2000). Multiple forces contribute to cell sheet morphogenesis for dorsal closure in Drosophila. J. Cell Biol. 149, 471–490.

Klepikova, A.V., Kasianov, A.S., Gerasimov, E.S., Logacheva, M.D., and Penin, A.A. (2016). A high resolution map of the Arabidopsis thaliana developmental transcriptome based on RNA-seq profiling. Plant J. 88, 1058–1070.

Ko, J.-H., and Kojima, S. (2009). Angular Dispersion-type Nonscanning Fabry-Perot Interferometer Applied to Ethanol-water Mixture. J. Opt. Soc. Korea 13, 261–266.

Ko, J.-H., Han, K.-H., Park, S., and Yang, J. (2004). Plant body weight-induced secondary growth in Arabidopsis and its transcription phenotype revealed by whole-transcriptome profiling. Plant Physiol. 135, 1069–1083.

Kramer, E.M., and Bennett, M.J. (2006). Auxin transport: a field in flux. Trends Plant Sci. 11, 382–386.

Kramer, E.M., Lewandowski, M., Beri, S., Bernard, J., Borkowski, M., Borkowski, M.H., Burchfield, L.A., Mathisen, B., and Normanly, J. (2008). Auxin gradients are associated with polarity changes in trees. Science 320, 1610.

Lamport, D.T.A., Kieliszewski, M.J., Chen, Y., and Cannon, M.C. (2011). Role of the extensin superfamily in primary cell wall architecture. Plant Physiol. 156, 11–19.

Lampropoulos, A., Sutikovic, Z., Wenzl, C., Maegele, I., Lohmann, J.U., and Forner, J. (2013). GreenGate---a novel, versatile, and efficient cloning system for plant transgenesis. PLoS One 8, e83043.

Laskowski, M., Biller, S., Stanley, K., Kajstura, T., and Prusty, R. (2006). Expression profiling of auxin-treated Arabidopsis roots: toward a molecular analysis of lateral root emergence. Plant Cell Physiol. 47, 788–792.

Lavy, M., Prigge, M.J., Tao, S., Shain, S., Kuo, A., Kirchsteiger, K., and Estelle, M. (2016). Constitutive auxin response in Physcomitrella reveals complex interactions between Aux/IAA and ARF proteins. Elife 5.

Lee, L.M., and Liu, A.P. (2014). The application of micropipette aspiration in molecular mechanics of single cells. J. Nanotechnol. Eng. Med. 5, 0408011–0408016.
Lehman, T.A., and Sanguinet, K.A. (2019). Auxin and Cell Wall Crosstalk as Revealed by the Arabidopsis thaliana Cellulose Synthase Mutant Radially Swollen 1. Plant Cell Physiol. 60, 1487–1503.

Leroux, O., Knox, J.P., Leroux, F., Vrijdaghs, A., Bellefroid, E., Borgonie, G., and Viane, R.L.L. (2007). Intercellular pectic protuberances in Asplenium: new data on their composition and origin. Ann. Bot. 100, 1165–1173.

Leyser, O. (2018). Auxin Signaling. Plant Physiol. 176, 465–479.

Li, H.Y., McSharry, M., Walker, D., Johnson, A., Kwak, J., Bullock, B., Neuwelt, A., Poczobutt, J.M., Sippel, T.R., Keith, R.L., et al. (2018). Targeted overexpression of

prostacyclin synthase inhibits lung tumor progression by recruiting CD4+ T lymphocytes in tumors that express MHC class II. Oncoimmunology e1423182.

Li, Y., Jones, L., and McQueen-Mason, S. (2003). Expansins and cell growth. Curr. Opin. Plant Biol. 6, 603–610.

Liners, F., Thibault, J.F., and Van Cutsem, P. (1992). Influence of the degree of polymerization of oligogalacturonates and of esterification pattern of pectin on their recognition by monoclonal antibodies. Plant Physiol. 99, 1099–1104.

Ljung, K., Bhalerao, R.P., and Sandberg, G. (2001). Sites and homeostatic control of auxin biosynthesis in Arabidopsis during vegetative growth. Plant J. 28, 465–474.

Ma, Y., Miotk, A., Šutiković, Z., Ermakova, O., Wenzl, C., Medzihradszky, A., Gaillochet, C., Forner, J., Utan, G., Brackmann, K., et al. (2019). WUSCHEL acts as an auxin response rheostat to maintain apical stem cells in Arabidopsis. Nat. Commun. 10, 5093.

Majda, M., and Robert, S. (2018). The role of auxin in cell wall expansion. Int. J. Mol. Sci. 19.

Marchant, A., Kargul, J., May, S.T., Muller, P., Delbarre, A., Perrot-Rechenmann, C., and Bennett, M.J. (1999). AUX1 regulates root gravitropism in Arabidopsis by facilitating auxin uptake within root apical tissues. EMBO J. 18, 2066–2073.

Marga, F., Grandbois, M., Cosgrove, D.J., and Baskin, T.I. (2005). Cell wall extension results in the coordinate separation of parallel microfibrils: evidence from scanning electron microscopy and atomic force microscopy. Plant J. 43, 181–190.

Mayer, K.F., Schoof, H., Haecker, A., Lenhard, M., Jürgens, G., and Laux, T. (1998). Role of WUSCHEL in regulating stem cell fate in the Arabidopsis shoot meristem. Cell 95, 805–815.

Mazur, E., and Kurczynska, E.U. (2012). Rays, intrusive growth, and storied cambium in the inflorescence stems of Arabidopsis thaliana (L.) Heynh. Protoplasma 249, 217–220.

Mazur, E., Kurczyńska, E.U., and Friml, J. (2014). Cellular events during interfascicular cambium ontogenesis in inflorescence stems of Arabidopsis. Protoplasma 251, 1125–1139.

McCartney, L., Ormerod, A.P., Gidley, M.J., and Knox, J.P. (2000). Temporal and spatial regulation of pectic (1-->4)-beta-D-galactan in cell walls of developing pea cotyledons: implications for mechanical properties. Plant J. 22, 105–113.
McQueen-Mason, S., Durachko, D.M., and Cosgrove, D.J. (1992). Two endogenous proteins that induce cell wall extension in plants. Plant Cell 4, 1425–1433.

Meng, Z., Traverso, A.J., and Yakovlev, V.V. (2014). Background clean-up in Brillouin microspectroscopy of scattering medium. Opt. Express 22, 5410–5415.

Muday, G.K. (2001). Auxins and Tropisms. J. Plant Growth Regul. 20, 226–243.

Müller, D.J., and Dufrêne, Y.F. (2011). Atomic force microscopy: a nanoscopic window on the cell surface. Trends Cell Biol. 21, 461–469.

Mutwil, M., Debolt, S., and Persson, S. (2008). Cellulose synthesis: a complex complex. Curr. Opin. Plant Biol. 11, 252–257.

Nemhauser, J.L., Hong, F., and Chory, J. (2006). Different plant hormones regulate similar processes through largely nonoverlapping transcriptional responses. Cell 126, 467–475.

Nieminen, K., Blomster, T., Helariutta, Y., and Mähönen, A.P. (2015). Vascular Cambium Development. Arabidopsis Book 13, e0177.

Normand, V., Lootens, D.L., Amici, E., Plucknett, K.P., and Aymard, P. (2000). New insight into agarose gel mechanical properties. Biomacromolecules 1, 730–738.

O'Neill, M.A., Ishii, T., Albersheim, P., and Darvill, A.G. (2004). Rhamnogalacturonan II: structure and function of a borate cross-linked cell wall pectic polysaccharide. Annu. Rev. Plant Biol. 55, 109–139.

Okushima, Y., Overvoorde, P.J., Arima, K., Alonso, J.M., Chan, A., Chang, C., Ecker, J.R., Hughes, B., Lui, A., Nguyen, D., et al. (2005). Functional genomic analysis of the AUXIN RESPONSE FACTOR gene family members in Arabidopsis thaliana: unique and overlapping functions of ARF7 and ARF19. Plant Cell 17, 444–463.

Pacheco-Villalobos, D., Díaz-Moreno, S.M., van der Schuren, A., Tamaki, T., Kang, Y.H., Gujas, B., Novak, O., Jaspert, N., Li, Z., Wolf, S., et al. (2016). The Effects of High Steady State Auxin Levels on Root Cell Elongation in Brachypodium. Plant Cell 28, 1009–1024.

Pacifici, E., Di Mambro, R., Dello Ioio, R., Costantino, P., and Sabatini, S. (2018). Acidic cell elongation drives cell differentiation in the Arabidopsis root. EMBO J. 37.

Paredez, A.R., Somerville, C.R., and Ehrhardt, D.W. (2006). Visualization of cellulose synthase demonstrates functional association with microtubules. Science 312, 1491–1495.

Parre, E., and Geitmann, A. (2005). More than a leak sealant. The mechanical properties of callose in pollen tubes. Plant Physiol. 137, 274–286.

Paynel, F., Leroux, C., Surcouf, O., Schaumann, A., Pelloux, J., Driouich, A., Mollet, J.C., Lerouge, P., Lehner, A., and Mareck, A. (2014). Kiwi fruit PMEI inhibits PME activity, modulates root elongation and induces pollen tube burst in Arabidopsis thaliana. Plant Growth Regul. 74, 285–297.
Peaucelle, A., Louvet, R., Johansen, J.N., Höfte, H., Laufs, P., Pelloux, J., and Mouille, G. (2008). Arabidopsis phyllotaxis is controlled by the methyl-esterification status of cell-wall pectins. Curr. Biol. 18, 1943–1948.

Peaucelle, A., Braybrook, S.A., Le Guillou, L., Bron, E., Kuhlemeier, C., and Höfte, H. (2011). Pectin-induced changes in cell wall mechanics underlie organ initiation in Arabidopsis. Curr. Biol. 21, 1720–1726.

Peaucelle, A., Wightman, R., and Höfte, H. (2015). The control of growth symmetry breaking in the arabidopsis hypocotyl. Curr. Biol. 25, 1746–1752.

Pek, Y.S., Wan, A.C.A., and Ying, J.Y. (2010). The effect of matrix stiffness on mesenchymal stem cell differentiation in a 3D thixotropic gel. Biomaterials 31, 385–391.

Péret, B., Li, G., Zhao, J., Band, L.R., Voß, U., Postaire, O., Luu, D.-T., Da Ines, O., Casimiro, I., Lucas, M., et al. (2012). Auxin regulates aquaporin function to facilitate lateral root emergence. Nat. Cell Biol. 14, 991–998.

Petersson, S.V., Johansson, A.I., Kowalczyk, M., Makoveychuk, A., Wang, J.Y., Moritz, T., Grebe, M., Benfey, P.N., Sandberg, G., and Ljung, K. (2009). An auxin gradient and maximum in the Arabidopsis root apex shown by high-resolution cell-specific analysis of IAA distribution and synthesis. Plant Cell 21, 1659–1668.

Proseus, T.E., and Boyer, J.S. (2005). Turgor pressure moves polysaccharides into growing cell walls of Chara corallina. Ann. Bot. 95, 967–979.

Qiu, T., Qi, M., Ding, X., Zheng, Y., Zhou, T., Chen, Y., Han, N., Zhu, M., Bian, H., and Wang, J. (2020). The SAUR41 subfamily of SMALL AUXIN UP RNA genes is abscisic acid inducible to modulate cell expansion and salt tolerance in Arabidopsis thaliana seedlings. Ann. Bot. 125, 805–819.

Quint, M., and Gray, W.M. (2006). Auxin signaling. Curr. Opin. Plant Biol. 9, 448–453.

Rahni, R., and Birnbaum, K.D. (2019). Week-long imaging of cell divisions in the Arabidopsis root meristem. Plant Methods 15, 30.

Rashotte, A.M., Brady, S.R., Reed, R.C., Ante, S.J., and Muday, G.K. (2000). Basipetal auxin transport is required for gravitropism in roots of Arabidopsis. Plant Physiol. 122, 481–490.

Rayle, D.L., and Cleland, R.E. (1992). The Acid Growth Theory of auxin-induced cell elongation is alive and well. Plant Physiol. 99, 1271–1274.

Reinhardt, D., Wittwer, F., Mandel, T., and Kuhlemeier, C. (1998). Localized upregulation of a new expansin gene predicts the site of leaf formation in the tomato meristem. Plant Cell 10, 1427–1437.

Romano, C.P., Robson, P.R., Smith, H., Estelle, M., and Klee, H. (1995). Transgene-mediated auxin overproduction in Arabidopsis: hypocotyl elongation phenotype and interactions with the hy6-1 hypocotyl elongation and axr1 auxin-resistant mutants. Plant Mol. Biol. 27, 1071–1083.

Roslan, H.A., Salter, M.G., Wood, C.D., White, M.R., Croft, K.P., Robson, F., Coupland, G., Doonan, J., Laufs, P., Tomsett, A.B., et al. (2001). Characterization of the ethanol-inducible alc gene-expression system in Arabidopsis thaliana. Plant J. 28, 225–235.

Sampathkumar, A., Peaucelle, A., Fujita, M., Schuster, C., Persson, S., Wasteneys, G.O., and Meyerowitz, E.M. (2019). Primary wall cellulose synthase regulates shoot apical meristem mechanics and growth. Development 146.

Sanchez, P. (2013). Cell fate regulation in the Arabidopsis thaliana stem. (:none).

Sasaki, K., Himeno, A., Nakagawa, T., Sasaki, Y., Kiyonari, H., and Iwai, K. (2019). Modulation of autoimmune pathogenesis by T cell-triggered inflammatory cell death. Nat. Commun. 10, 3878.

Sassi, M., Ali, O., Boudon, F., Cloarec, G., Abad, U., Cellier, C., Chen, X., Gilles, B., Milani, P., Friml, J., et al. (2014). An auxin-mediated shift toward growth isotropy promotes organ formation at the shoot meristem in Arabidopsis. Curr. Biol. 24, 2335–2342.

Scarcelli, G., and Yun, S.H. (2007). Confocal Brillouin microscopy for three-dimensional mechanical imaging. Nat. Photonics 2, 39–43.

Scarcelli, G., and Yun, S.H. (2011). Multistage VIPA etalons for high-extinction parallel Brillouin spectroscopy. Opt. Express 19, 10913–10922.

Scarcelli, G., Polacheck, W.J., Nia, H.T., Patel, K., Grodzinsky, A.J., Kamm, R.D., and Yun, S.H. (2015). Noncontact three-dimensional mapping of intracellular hydromechanical properties by Brillouin microscopy. Nat. Methods 12, 1132–1134.

Scheller, H.V., and Ulvskov, P. (2010). Hemicelluloses. Annu. Rev. Plant Biol. 61, 263–289.

Schnabelrauch, L.S., Kieliszewski, M., Upham, B.L., Alizedeh, H., and Lamport, D.T. (1996). Isolation of pl 4.6 extensin peroxidase from tomato cell suspension cultures and identification of Val-Tyr-Lys as putative intermolecular cross-link site. Plant J. 9, 477–489.

Schötz, E.-M., Burdine, R.D., Jülicher, F., Steinberg, M.S., Heisenberg, C.-P., and Foty, R.A. (2008). Quantitative differences in tissue surface tension influence zebrafish germ layer positioning. HFSP J 2, 42–56.

Schürholz, A.-K. (2019). Spatio-temporal control of cell wall propterties and signalling networks in Arabidopsis meristems. Heidelberg University Library.

Schürholz, A.-K., Lopez-Salmeron, V., Li, Z., Forner, J., Wenzl, C., Gaillochet, C., Augustin, S., Vilches-Barro, A., Fuchs, M., Gebert, M., et al. (2018). A comprehensive toolkit for inducible, cell type-specific gene expression in Arabidopsis. Plant Physiol. 178, 40–53.

Sehr, E.M., Agusti, J., Lehner, R., Farmer, E.E., Schwarz, M., and Greb, T. (2010). Analysis of secondary growth in the Arabidopsis shoot reveals a positive role of jasmonate signalling in cambium formation. Plant J. 63, 811–822.

Shani, Z., Dekel, M., Roiz, L., Horowitz, M., Kolosovski, N., Lapidot, S., Alkan, S., Koltai, H., Tsabary, G., Goren, R., et al. (2006). Expression of endo-1,4-beta-glucanase (cel1) in Arabidopsis thaliana is associated with plant growth, xylem development and cell wall thickening. Plant Cell Rep. 25, 1067–1074.

Shi, D., Jouannet, V., Agusti, J., Kaul, V., Levitsky, V., Mironova, V.V., Sanchez, P., and Greb, T. (2020). Tissue-specific transcriptome profiling of the Arabidopsis thaliana inflorescence stem reveals local cellular signatures. BioRxiv.

Slie, W.M., Donfor, A.R., and Litovitz, T.A. (1966). Ultrasonic shear and longitudinal measurements in aqueous glycerol. J. Chem. Phys. 44, 3712–3718.

De Smet, I., Lau, S., Voss, U., Vanneste, S., Benjamins, R., Rademacher, E.H., Schlereth, A., De Rybel, B., Vassileva, V., Grunewald, W., et al. (2010). Bimodular auxin response controls organogenesis in Arabidopsis. Proc. Natl. Acad. Sci. USA 107, 2705–2710.

Smetana, O., Mäkilä, R., Lyu, M., Amiryousefi, A., Sánchez Rodríguez, F., Wu, M.-F., Solé-Gil, A., Leal Gavarrón, M., Siligato, R., Miyashima, S., et al. (2019). High levels of auxin signalling define the stem-cell organizer of the vascular cambium. Nature 565, 485–489.

Smith, J.J., Muldoon, E.P., and Lamport, D.T.A. (1984). Isolation of extensin precursors by direct elution of intact tomato cell suspension cultures. Phytochemistry 23, 1233–1239.

Somerville, C. (2006). Cellulose synthesis in higher plants. Annu. Rev. Cell Dev. Biol. 22, 53–78.
Spartz, A.K., Ren, H., Park, M.Y., Grandt, K.N., Lee, S.H., Murphy, A.S., Sussman, M.R., Overvoorde, P.J., and Gray, W.M. (2014). SAUR Inhibition of PP2C-D Phosphatases Activates Plasma Membrane H+-ATPases to Promote Cell Expansion in Arabidopsis. Plant Cell 26, 2129–2142.

Stahl, Y., Wink, R.H., Ingram, G.C., and Simon, R. (2009). A signaling module controlling the stem cell niche in Arabidopsis root meristems. Curr. Biol. 19, 909–914.

Suer, S., Agusti, J., Sanchez, P., Schwarz, M., and Greb, T. (2011). WOX4 imparts auxin responsiveness to cambium cells in Arabidopsis. Plant Cell 23, 3247–3259.

Sugimoto, K., Williamson, R.E., and Wasteneys, G.O. (2000). New techniques enable comparative analysis of microtubule orientation, wall texture, and growth rate in intact roots of Arabidopsis. Plant Physiol. 124, 1493–1506.

Swarup, K., Benková, E., Swarup, R., Casimiro, I., Péret, B., Yang, Y., Parry, G., Nielsen, E., De Smet, I., Vanneste, S., et al. (2008). The auxin influx carrier LAX3 promotes lateral root emergence. Nat. Cell Biol. 10, 946–954.

Takahashi, K., Hayashi, K., and Kinoshita, T. (2012). Auxin activates the plasma membrane H+-ATPase by phosphorylation during hypocotyl elongation in Arabidopsis. Plant Physiol. 159, 632–641.

Takenaka, Y., Watanabe, Y., Schuetz, M., Unda, F., Hill, J.L., Phookaew, P., Yoneda, A., Mansfield, S.D., Samuels, L., Ohtani, M., et al. (2018a). Patterned Deposition of Xylan and Lignin is Independent from that of the Secondary Wall Cellulose of Arabidopsis Xylem Vessels. Plant Cell 30, 2663–2676.

Takenaka, Y., Kato, K., Ogawa-Ohnishi, M., Tsuruhama, K., Kajiura, H., Yagyu, K., Takeda, A., Takeda, Y., Kunieda, T., Hara-Nishimura, I., et al. (2018b). Pectin RG-I rhamnosyltransferases represent a novel plant-specific glycosyltransferase family. Nat. Plants 4, 669–676.
Tan, X., Calderon-Villalobos, L.I.A., Sharon, M., Zheng, C., Robinson, C.V., Estelle, M., and Zheng, N. (2007). Mechanism of auxin perception by the TIR1 ubiquitin ligase. Nature 446, 640–645.

Thomson, J.A. (1917). On growth and form. Nature 100, 21–22.

Tonn, N., and Greb, T. (2017). Radial plant growth. Curr. Biol. 27, R878–R882.

Uggla, C., Moritz, T., Sandberg, G., and Sundberg, B. (1996). Auxin as a positional signal in pattern formation in plants. Proc. Natl. Acad. Sci. USA 93, 9282–9286.

Uggla, C., Mellerowicz, E.J., and Sundberg, B. (1998). Indole-3-acetic acid controls cambial growth in scots pine by positional signaling. Plant Physiol. 117, 113–121.

Ulmasov, T., Murfett, J., Hagen, G., and Guilfoyle, T.J. (1997). Aux/IAA proteins repress expression of reporter genes containing natural and highly active synthetic auxin response elements. Plant Cell 9, 1963–1971.

Vain, T., Crowell, E.F., Timpano, H., Biot, E., Desprez, T., Mansoori, N., Trindade, L.M., Pagant, S., Robert, S., Höfte, H., et al. (2014). The cellulase KORRIGAN is part of the cellulose synthase complex. Plant Physiol. 165, 1521–1532.

Verhertbruggen, Y., Marcus, S.E., Haeger, A., Ordaz-Ortiz, J.J., and Knox, J.P. (2009). An extended set of monoclonal antibodies to pectic homogalacturonan. Carbohydr. Res. 344, 1858–1862.

Vincken, J.-P., Schols, H.A., Oomen, R.J.F.J., McCann, M.C., Ulvskov, P., Voragen, A.G.J., and Visser, R.G.F. (2003). If homogalacturonan were a side chain of rhamnogalacturonan I. Implications for cell wall architecture. Plant Physiol. 132, 1781–1789.

Vogler, H., Draeger, C., Weber, A., Felekis, D., Eichenberger, C., Routier-Kierzkowska, A.-L., Boisson-Dernier, A., Ringli, C., Nelson, B.J., Smith, R.S., et al. (2013). The pollen tube: a soft shell with a hard core. Plant J. 73, 617–627.

Wang, C.X., Wang, L., McQueen-Mason, S.J., Pritchard, J., and Thomas, C.R. (2008). pH and expansin action on single suspension-cultured tomato (Lycopersicon esculentum) cells. J Plant Res 121, 527–534.
Wang, S., Hagen, G., and Guilfoyle, T.J. (2013). ARF-Aux/IAA interactions through domain III/IV are not strictly required for auxin-responsive gene expression. Plant Signal. Behav. 8, e24526.

Wang, X., Yu, R., Wang, J., Lin, Z., Han, X., Deng, Z., Fan, L., He, H., Deng, X.W., and Chen, H. (2020). The asymmetric expression of SAUR genes mediated by ARF7/19 promotes the gravitropism and phototropism of plant hypocotyls. Cell Rep. 31, 107529.

Webb, J.N., Zhang, H., Roy, A.S., Randleman, J.B., and Scarcelli, G. (2020). Detecting mechanical anisotropy of the cornea using brillouin microscopy. Transl Vis Sci Technol 9, 26.

Weihs, D., Mason, T.G., and Teitell, M.A. (2006). Bio-microrheology: a frontier in microrheology. Biophys. J. 91, 4296–4305.
Weijers, D., Benkova, E., Jäger, K.E., Schlereth, A., Hamann, T., Kientz, M., Wilmoth, J.C., Reed, J.W., and Jürgens, G. (2005). Developmental specificity of auxin response by pairs of ARF and Aux/IAA transcriptional regulators. EMBO J. 24, 1874–1885.

Willats, W.G.T., McCartney, L., Mackie, W., and Knox, J.P. (2001). Pectin: cell biology and prospects for functional analysis. Springer Science and Business Media LLC.

Wolf, S., Mouille, G., and Pelloux, J. (2009). Homogalacturonan methyl-esterification and plant development. Mol. Plant 2, 851–860.

Wolf, S., Hématy, K., and Höfte, H. (2012a). Growth control and cell wall signaling in plants. Annu. Rev. Plant Biol. 63, 381–407.

Wolf, S., Mravec, J., Greiner, S., Mouille, G., and Höfte, H. (2012b). Plant cell wall homeostasis is mediated by brassinosteroid feedback signaling. Curr. Biol. 22, 1732–1737.

Wolf, S., van der Does, D., Ladwig, F., Sticht, C., Kolbeck, A., Schürholz, A.-K., Augustin, S., Keinath, N., Rausch, T., Greiner, S., et al. (2014). A receptor-like protein

mediates the response to pectin modification by activating brassinosteroid signaling. Proc. Natl. Acad. Sci. USA 111, 15261–15266.

Wysocka-Diller, J.W., Helariutta, Y., Fukaki, H., Malamy, J.E., and Benfey, P.N. (2000). Molecular analysis of SCARECROW function reveals a radial patterning mechanism common to root and shoot. Development 127, 595–603.

Xiao, C., Zhang, T., Zheng, Y., Cosgrove, D.J., and Anderson, C.T. (2016). Xyloglucan deficiency disrupts microtubule stability and cellulose biosynthesis in arabidopsis, altering cell growth and morphogenesis. Plant Physiol. 170, 234–249.

Zandleven, J., Sørensen, S.O., Harholt, J., Beldman, G., Schols, H.A., Scheller, H.V., and Voragen, A.J. (2007). Xylogalacturonan exists in cell walls from various tissues of Arabidopsis thaliana. Phytochemistry 68, 1219–1226.

Zhou, P., and Howley, P.M. (1998). Ubiquitination and degradation of the substrate recognition subunits of SCF ubiquitin-protein ligases. Mol. Cell 2, 571–580.

Žigon-Branc, S., Markovic, M., Van Hoorick, J., Van Vlierberghe, S., Dubruel, P., Zerobin, E., Baudis, S., and Ovsianikov, A. (2019). Impact of Hydrogel Stiffness on Differentiation of Human Adipose-Derived Stem Cell Microspheroids. Tissue Eng. Part A 25, 1369–1380.
(2018). Biomechanics in Oncology (Cham: Springer International Publishing).